Use of the seismic reflection method to optimize safety and extraction: A case study from a South African platinum mine

Prepared by

Seeiso A. Moshoeshoe

Supervisors: Prof. Raymond Durrheim, Prof. Musa Manzi

A dissertation submitted to the Faculty of Science, University of the Witwatersrand in fulfilment of the requirements for the degree of

Master of Science

Declaration

I declare that this dissertation is my own, unaided work. It is being submitted for the Master of Science at the University of the Witwatersrand, Johannesburg. It has not been submitted before for any degree or examination at any other University.

Seeiso Moshoeshoe

Digitally signed by Seeiso Moshoeshoe
Date: 2019.08.31 19:09:44 +02'00'

Seeiso Alexander Moshoeshoe

31st day of August 2019 in Johannesburg

Abstract

Mining operations in the Bushveld Complex platinum mines have been mostly restricted to shallow depths (<1000 m) but are migrating to intermediate depths (1000 – 2250 m). This migration is met with complexities in the local geology, prevailing rock mass conditions, thickness and dip of the orebody, all of which influence the mining procedures and standards. Mining is likely to encounter zones of rock weakness, high stress and induced seismicity. This study aims to investigate the structural complexity of the remaining part of the lease area of a platinum mine. This is an area earmarked for future operations, and thus the impact and effect these complexities have on current mining operations is studied to understand what future mine planning and ore valuation should entail. Investigation was done in two phases: the comparison of conventional to seismic attribute interpretation, and the formulation of an interpretation workflow for the seismic attributes.

Initial conventional interpretation was carried out by picking the UG2 marker horizon throughout the 3D reflection seismic data and correlating results with borehole data and synthetic seismographs. The workflow that was developed and used in this study first involved data gridding using a constrained biharmonic operator. Then various horizon seismic attributes (surface stability index, dip angle, dip-azimuth and edge detection) were used to enhance the visibility and continuity on structures (e.g. lineaments and reef terracing) not readily visible on the horizon picked using conventional techniques. Subsequently, volumetric seismic attributes (data conditioning using the dominant frequency, structural smoothing vs graphic equalizer attributes, then edge detection using variance vs chaos attributes) were applied. The outputs from variance and chaos attributes were then used as inputs to the ant-tracking algorithm. Conventional interpretation yielded expected first order results, notably horizons dipping between 9º - 12º in the NE direction, as described in the literature, but could not discern more structural detail. The dip angle, dip-azimuth and edge detection seismic attributes immediately picked up linear features trending NW – SE and a few SW – NE, possibly fault zones. It also confirmed that the dip angle found using conventional interpretation techniques, ranged between 5º to > 10º, with the steeper dips associated with regions too noisy to pick and are possible zones of depression. The ant-tracking volume from the variance attribute was chosen over the chaos attribute due to better resolution. The ant-tracked volume enhanced the visibility of gently dipping structures, initially seen in the data but not well resolved. It also enhanced steeply dipping structures that

were not visible to the conventionally-processed data. In the end, it was very clear that good results are dependent on the interpretation workflow used and thus great care should always be taken before and during the use of seismic attributes as undesired features, like noise, can also be enhanced.

Acknowledgement

I would like to express my gratitude and thanks to my supervisors Professor Raymond Durrheim and Professor Musa Manzi for providing me with unwavering support and guidance throughout my Masters programme.

I would like to thank my parents for their motivation, support and presence throughout my studies and to the rest of my family and friends who cheered me on throughout this journey.

I would like to acknowledge Impala Platinum mine for granting access to the 3D reflection seismic cube that was used in this study.

I would like to acknowledge Schlumberger for their continuous support with their Petrel Exploration and Production (E&P) Software Platform 2015 and DownUnder Geosolutions for the DUG Insight seismic interpretation software package.

The National Research Foundation (NRF) is also greatly appreciated for funding my studies. Finally, I would also like to thank the School of Geosciences, staff and facilities for the support that was always important during my studies.

Contents

List of figures

List of tables

1. Introduction

South Africa is host to the Bushveld Complex, the world's largest layered intrusion (Figure 1.1). It hosts most of the world's known resources of platinum group elements (platinum, palladium, and rhodium), chromium and vanadium (Scoates and Friedman, 2008). Its platinum production constitutes a significant majority of the Earth's total (>75%), primarily from the two strati-form sequences, namely the Merensky Layer and the Upper Group 2 (UG2) chromitite layer (locally known as reefs) (Cawthorn, 2010).

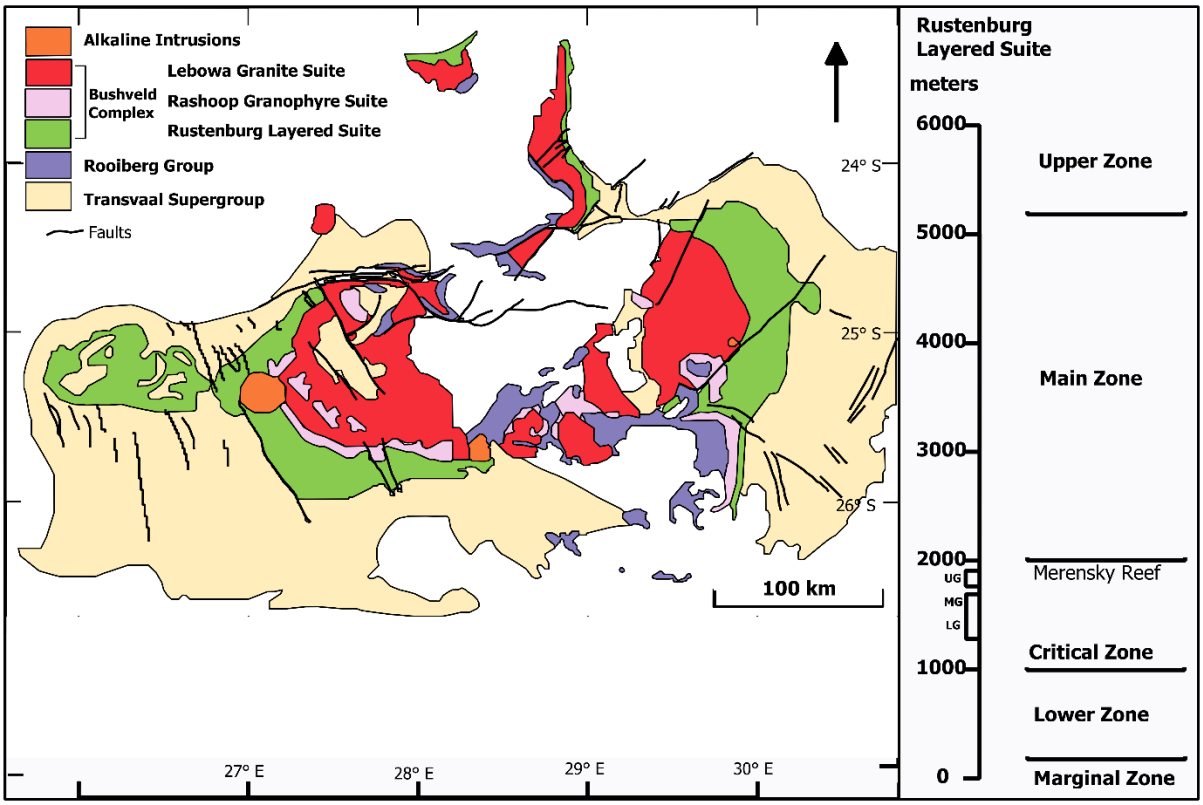

Figure 1.1: Generalized geological map outlining the Bushveld Complex (adapted from Scoates and Friedman, 2008).

Mining operations in the Bushveld Complex face challenges associated with progressive increases in mining depth and currently, unpredictable geological complexities (e.g. faults, dykes and pegmatoid intrusions) (Ledwaba, 2012). In particular, zones of reef depression (termed potholes) and varying dips and strikes along the reefs need to be better defined to enable safe and efficient mining (Zindi, 2008).

Mining depth is also the central factor in determining the optimum extraction plan of an ore reserve. The following terms are used to classify the depth of mining in South Africa: shallow (< 1000 m), medium (1000 m – 2250 m), deep (2250 m – 3500 m) and ultra-deep (>3500 m) (Jager and Ryder, 1999). Mining for platinum group metals in the Bushveld Complex has been mostly restricted to the shallow depths but is currently approaching medium depths. The characteristics (local geology, prevailing rock mass conditions, thickness and dip of the orebody) critically influence the mining procedures and standards (Jager and Ryder, 1999).

Platinum mines in the Bushveld Complex are in areas of high geothermal gradient compared to, for example, the gold mines of the Witwatersrand Basin. High rock temperatures of these platinum mines are encountered at relatively shallower depths (Karsten and Mackay, 2012). One of the biggest hazards in the Witwatersrand Basin is seismicity and rockbursts (Riemer and Durrheim, 2012). Though much experience has been gained from the deep gold mines of the Witwatersrand Basin, it is not directly applicable to the Bushveld Complex mines as the geotechnical properties and stress regimes differ considerably (Durrheim et al., 2005).

The reflection seismic method has been widely used for platinum, gold and base metal explorations in Southern Africa and has proven useful for mine design and planning (Stevenson and Durrheim, 1997). In the early 1980s, the extension of existing mines and planning of new mines relied mostly on geological models that were based on a combination of aeromagnetic gravity and borehole data (Durrheim, 1986). Although magnetic and gravity techniques effectively delineate major fault zones and magnetic dykes, they have limited ability to image pegmatoid intrusions, fault geometries and potholed reefs at a resolution essential for optimal mine planning (Trickett et al., 2004). Borehole data were considered the most detailed and reliable tool to extract geological information from mine structural features, but this method is limited by the restriction of the information to the vicinity around the borehole; even when linked with surface methods such as magnetic and gravity surveys (Chambovet, 2006).

Three-dimensional (3D) reflection seismic data were acquired between 1998 and 2002 in the western Bushveld Complex (Campbell, 2011). These data formed an integral part of mine planning and development due to their high-quality nature and ability to enhance 3D models of the geological structure of the Merensky and UG2 chromitite reefs. These models made it possible to deduce the sizes, geometries and distribution of mineable blocks (Duweke et al.,

2002). The capabilities of the method were immediately clear as zones of un-mineable ground caused by structural disturbances in the form of fault zones, pegmatoid intrusions and potholes were highlighted (Campbell, 2011). Furthermore, changes along the dip and strike of the platinum ore bodies were well defined, which permitted optimizations in the mine design, layout and safety considerations.

With the introduction of seismic trace attributes in early 1970s, came a new era of seismic data interpretation. Seismic attributes are all of the computed, measured or implied quantities obtained from the reflection seismic data (Barnes, 2007). These attributes can be classified as essentially physical and geometrical. Physical attributes are attributes directly related to the wave propagation, lithology and other physical properties, while the geometrical attributes enhance characteristics like discontinuity, dip and dip-azimuth (Subrahmanyam and Rao, 2008).

Seismic attributes may highlight subtle geological features hidden in the data leading to a more accurate interpretation of the reflection seismic data (Randen and Sønneland, 2005). Preliminary testing of seismic attributes analysis on the 3D seismic volume acquired in the Bushveld Complex showed the potential to illuminate several geological reef disruptions that were otherwise indiscernible in the original seismic time volume (Trickett, et al., 2004).

1.1. Aims and objectives of the study

The aim of this study was to interpret 3D reflection seismic data collected at Impala Platinum Mine (henceforth referred to as Impala), to better understand the local geology and assess the economic viability of the UG2 marker horizon in an area earmarked for future mining operations.

The main objectives of the study are as follows:

- Seismic interpretation of the two strati-form sequences, the Merensky and UG2 reefs, to develop a structural model of the lease area that could be used for mine planning.

- Identify and apply seismic trace attributes (physical and geometric attributes) to enhance:
    - mapping of the horizons,

- definition of zones of reef depression (‘slumps’ and ‘potholes’)
- definition of fault zones, and
- the identification of reef terracing and/or reverse dip

1.2. Study area and mining background

Impala is situated near the town of Rustenburg in the North-West Province of South Africa (Figure 1.2). It is part of Impala Platinum Holdings Limited; a company whose business includes mining, refining and marketing of platinum group metals (PGMs). In the early 1960s, Impala was established and had acquired a prospecting permit (Implats, 2015). Impala started mining and production of the Merensky Reef in 1969. Mining of the UG2 chromitite Reef only initiated in the early 1980s as the technology to smelt higher – ratio chrome ore was developed. By the early 1990s Impala was producing about 1 million ounces of platinum annually (Implats, 2015).

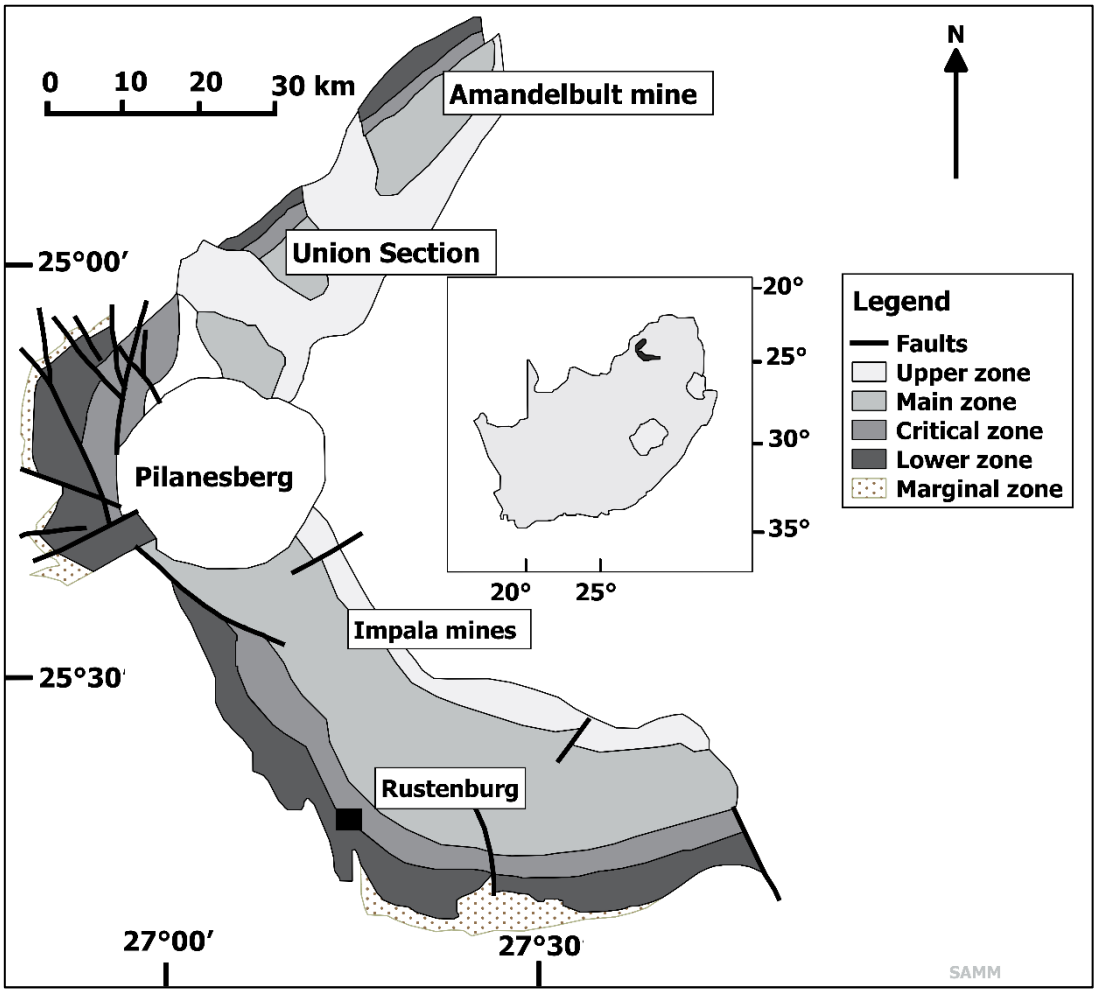

Figure 1.2: Map showing the location of the Impala mines in the western Bushveld Complex (adapted from Godel et al., 2006).

Impala's operations comprise a 14-shaft mining complex, smelting and concentrating plants (Implats, 2015). Both mineralized horizons dip gently at 10° to 12° away from the sub-outcrop in a north-easterly direction. The vertical separation between the Merensky and UG2 reefs varies from ~ 45 m in the north and ~ 125 m in the south of the mining area. The mining depths in underground operations for both the Merensky and UG2 reefs range from 30 m to 1250 m below surface. Mining panels are cut approximately 36 m long on the Merensky Reef where the hangingwall is relatively stable, while on the UG2 Reef, panels are approximately 30 m long (Leeb-Du Toit, 1986; Lougher, 1994).

The conventional double-sided breast mining method is predominantly used to mine the Merensky and UG2 reefs concurrently (Figure 1.3). The haulages are developed in opposite directions from the cross-cuts, which are all connected to a central shaft position. The two reef horizons run along strike in the footwall and are defined as half levels. Footwall drives are developed at approximately 18 m to 30 m below the reef horizon with on-reef raise/winze connections being between 180 m and 250 m apart. Panel face lengths vary from 15 m to 30 m for both Merensky and UG2 reefs, with panels being typically separated by 6 m x 3 m grid pillars with 2 m ventilation holings. Stoping widths are approximately 1.3 m and 1.1 m for conventional Merensky and UG2 reefs, respectively, depending on the width of the economical reef horizon (Implats, 2015).

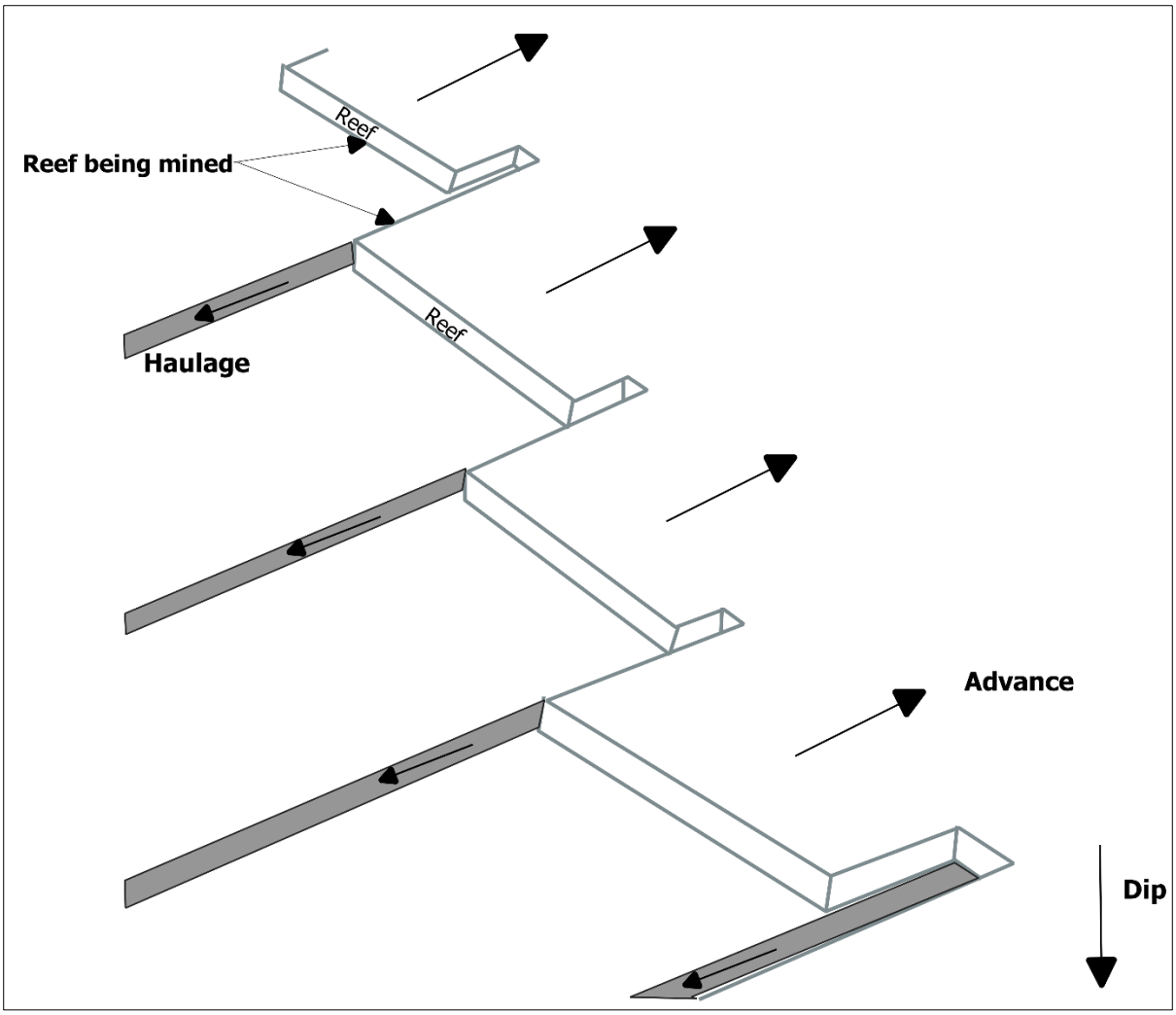

Figure 1.3: Illustration of conventional double-sided breast mining with haulages, advance direction and the reef being mined. This method is predominantly used to mine the Merensky and UG2 reefs (adapted from Implats, 2015).

Mechanized (trackless) bord and pillar mining occurs in selected Merensky Reef areas on two of the shafts, 12 and 14 Shafts (Figure 1.4). The average stoping width of mechanized panels is approximately 1.9 m (Implats, 2015).

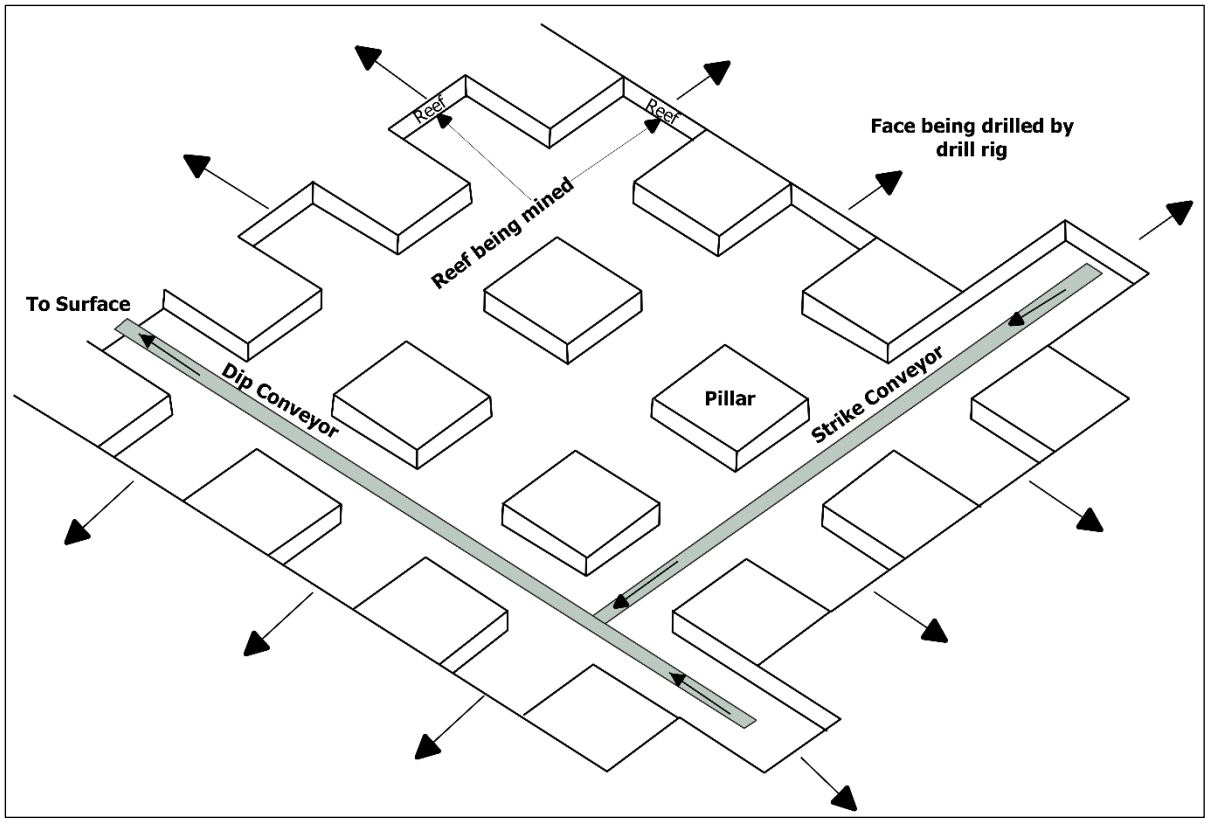

Figure 1.4: Illustration of mechanized bord and pillar mining method with strike conveyors from the stope face where the reef is being mined and the dip conveyors to the surface. This method is predominantly used to mine the Merensky Reef at Impala Platinum (adapted from Implats, 2015).

1.3. Overview of dissertation

This dissertation is divided into the following eight chapters:

Chapter 1 highlights the purpose and main objectives of the study, and provides a brief overview of the study area and mining background,

Chapter 2 provides a review of the geological and structural setting of the Bushveld Complex,

Chapter 3 introduces the principles of the seismic reflection method and its application in mineral exploration,

Chapter 4 presents the detailed methodology carried out in this study on the 3D reflection seismic data,

Chapter 5 presents the results of the seismic interpretation carried out in the study,

Chapter 6 is the discussion about the obtained results,

Chapter 7 draws conclusions from the results.

2. Geological and structural setting

Before the interpretation of the reflection seismic data, it is important to review the geological and structural setting. The geological setting relates to the time evolution of the stratigraphy and lithologies of the area, whereas the structural setting describes the area's tectonic history, which constrains the stress field dynamics that resulted in observed geometries and strain.

2.1. Geological sequence

2.1.1. Kaapvaal Craton

The Kaapvaal Craton comprises a complex mosaic of Archaean terranes that amalgamated episodically between about ~3.7 and ~2.8 Ga (Figure 2.1) (Nguuri et al., 2001). The Kaapvaal Craton measures approximately 1.2 x 10^6 km^2 and comprises predominantly granitoids interspersed with greenstone belts, covered by a variety of Neoarchaean to Mesoproterozoic sedimentary and volcano-sedimentary basins (Good and De Wit, 1997).

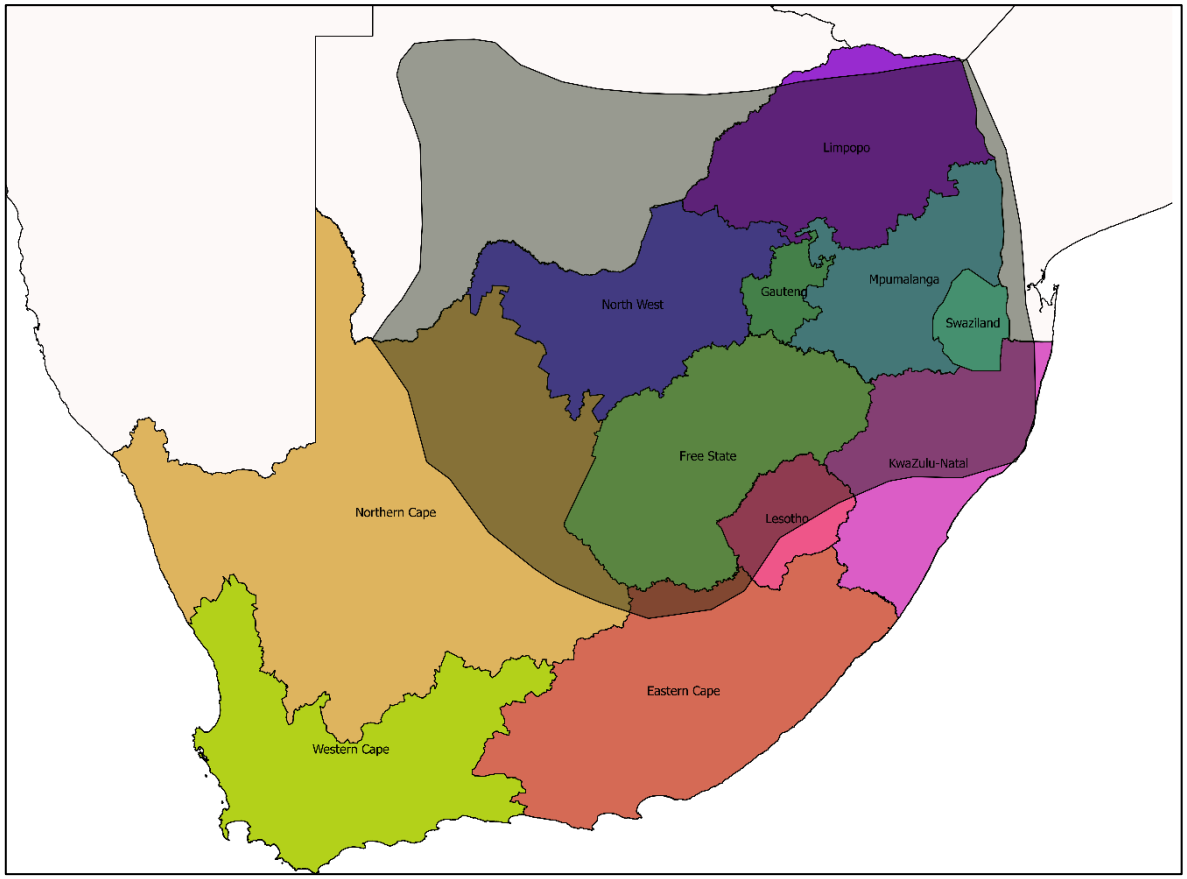

Figure 2.1: Outline of the Kaapvaal Craton (shade area) (adopted from Coetzee and Kisters, 2018).

The Archaean history of the craton includes the collision and stabilization of the Kaapvaal Craton and the Zimbabwe Craton to the north to form the Kaapvaal-Limpopo-Zimbabwe Block. The Palaeoproterozoic evolution of the now stable block was dominated by extensional regimes, in particular, intra-cratonic pull-apart sedimentary basins such as the Witwatersrand Basin (Eriksson et al., 1996).

2.1.2. Witwatersrand Basin

Following the stabilization of the Kaapvaal Craton, the Late Archaean to Early Proterozoic is characterized by the development of large volcano-sedimentary intra-cratonic basins. The NE-trending Archaean Witwatersrand Basin, a source of 40% of the world's gold, is one of the most significant of these basins (Kinnaird, 2005). Pulses of sedimentation within the sequence and its precursors were episodic (a period of over 360 Ma), occurring between 3074 ± 6 Ma (Dominion Group) (Robb and Meyer, 1995), > 2.98 – 2.91 Ga (West Rand Group) and > 2.90 – 2.78 Ga (Central Rand Group) (Nwaila et al., 2017). The Witwatersrand Basin is divided into the lower Witwatersrand Supergroup (3.074 Ga – 2.714 Ga), middle Ventersdorp Supergroup (2.72 – 2.63 Ga) and the upper Transvaal Supergroup (2.588 ± 0.006 Ga) (Robb and Meyer, 1995).

2.2. Bushveld Complex

The Bushveld Complex is the largest layered igneous intrusion, emplaced at ~ 2.06 Ga into the stable Kaapvaal Craton (Walraven et al., 1990). It intruded the intra-cratonic sedimentary sequences of the Transvaal Supergroup (Cawthorn and Webb, 2001). The Bushveld Complex formed by the crystallization of successive injections of magma. These were sufficiently closely spaced in time that each preceding magma had not cooled and differentiated significantly before the addition of the next one (Cawthorn and Walraven, 1998).

Unresolved problems in the Bushveld Complex include the processes and tectonic setting that controlled the emplacement of such a vast volume of magma. Features unique to the Bushveld Complex are its size, about 350 km by 350 km (Du Plessis and Walraven, 1990), the Rooiberg Group and the Rustenburg Layered Suite. The Rooiberg Group is one of the world's largest pyroclastic province, up to 3 km thick, and covering 50 000 km^2 while the Rustenburg Layered Suite is one of the world's oldest and largest mafic layered complex.

(Kinnaird, 2005). The emplacement of the Bushveld Complex is thought to have been guided by relict terrane boundaries or crustal-scale structures (Hunt, 2006).

The Bushveld Complex comprises four major limbs; the Eastern, the Western (which includes the Far Western), the Northern or Potgietersrus (including Villa Nora), and the Southeastern or Bethal limb (Figure 2.2). The general geology is divided into the Rooiberg Group, the Rashoop Granophyre Suite, the Lebowa Granite Suite and the Rustenburg Layered Suite (Eales and Cawthorn, 1996).

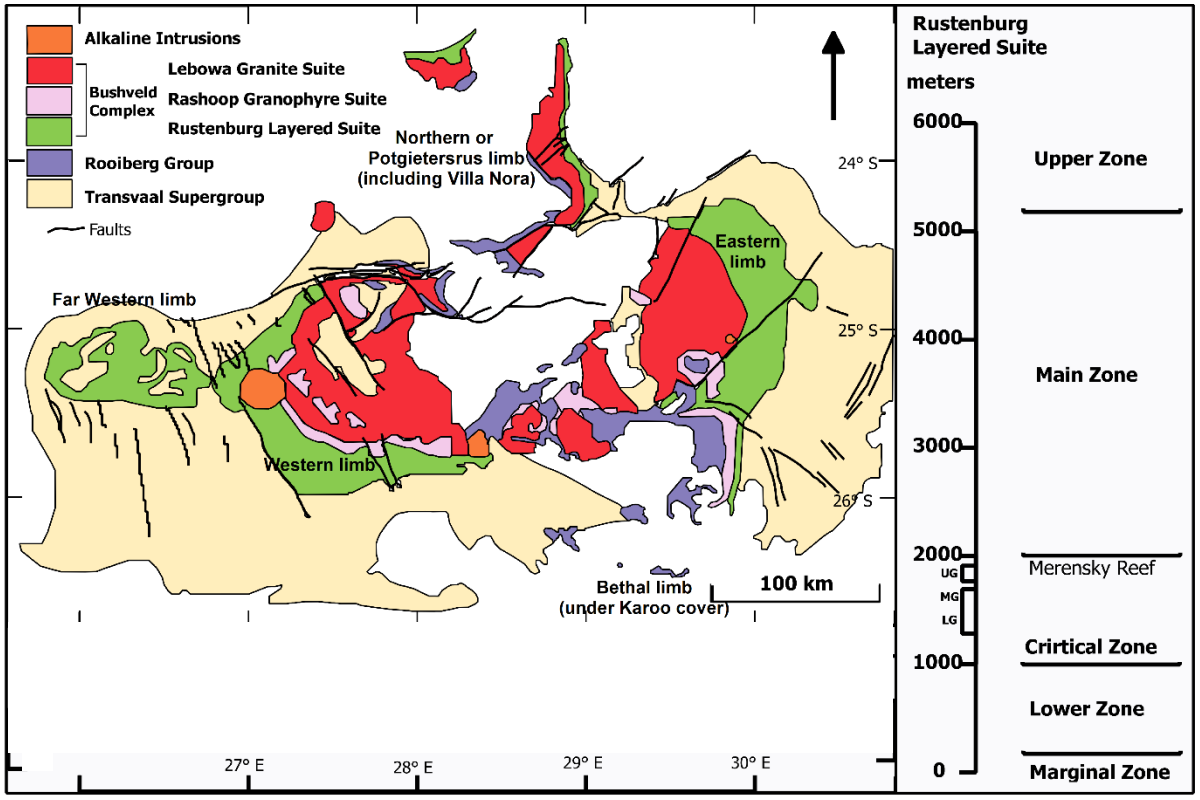

Figure 2.2: Generalized and labelled geological map outlining the Bushveld Complex (adapted from Scoates and Friedman, 2008).

2.2.1. Rooiberg Group

The Rooiberg Group volcanics, dated at 2057.3 ± 3.8 Ma using U-Pb SHRIMP zircon analysis (Harmer and Armstrong, 2000), are preserved over an areal extent of > 50,000 km^2 and are as thick as 3.5 km in the Loskop area (Schweitzer et al., 1995). Twist and French (1983) estimated the Rooiberg Group to have an original volume ~300,000 km^3 with a local thickness of more than 5 km. The Rooiberg Group has an extensive sequence of epicrustal acid volcanics comprising dacite pyroclastics, rare rhyolite flows and rare andesites. Lavas,

air-fall tuffs, ash-flow tuffs and hydrothermal tuffs are all present with interbedded shales, sandstones and volcanic mudflows (Hunt, 2006).

2.2.2. Lebowa Granite Suite

The Lebowa Granite Suite, dated at 2054.2 ± 2.8 Ma U-Pb SHRIMP (Harmer and Armstrong, 2000), consists of a 1.5 to 3.5 km thick series of sheeted intrusions (Kleemann and Twist, 1989), with an areal range of 30,000 km^2, and possibly a volume of ~ 100,000 km^3. The majority of the granitic units incorporated within the Lebowa Suite are comparatively minor to the Nebo Granite sheets, which are the major component of the acid phase of the Bushveld Complex and form a sill-like intrusive body over most of the complex (Walraven and Hattingh, 1993).

2.2.3. Rashoop Granophyre Suite

The Rashoop Granophyre Suite, dated at 2061.8 ± 5.51 Ma using U-Pb SHRIMP zircon analysis (Harmer and Armstrong, 2000), represents small volumes of partially re-melted Rooiberg volcanics and shallow intrusions of magma (Hatton and Schweitzer, 1995; Walraven, 1987). Two types of granophyres have been observed: magmatic and metamorphic granophyre units (Walraven, 1987).

2.2.4. Rustenburg Layered Suite

The Rustenburg Layered Suite comprises mafic and ultramafic rocks, ~ 9 km in thickness (Figure 2.3). It is dated at 2054.4 ± 2.8 Ma using U-Pb SHRIMP (Harmer and Armstrong, 2000). It consists of a wide array of rock types such as olivine, diorite, anorthosite, gabbro, norite, pyroxenite, harzburgite and bronzitite (Eriksson et al., 1995). The Rustenburg Layered Suite is generally sub-divided into five zones. From youngest to oldest, they are the Upper Zone, Main Zone, Critical Zone, Lower Zone and at the base is the Marginal Zone (Eales and Cawthorn, 1996; Kinnaird, 2005).

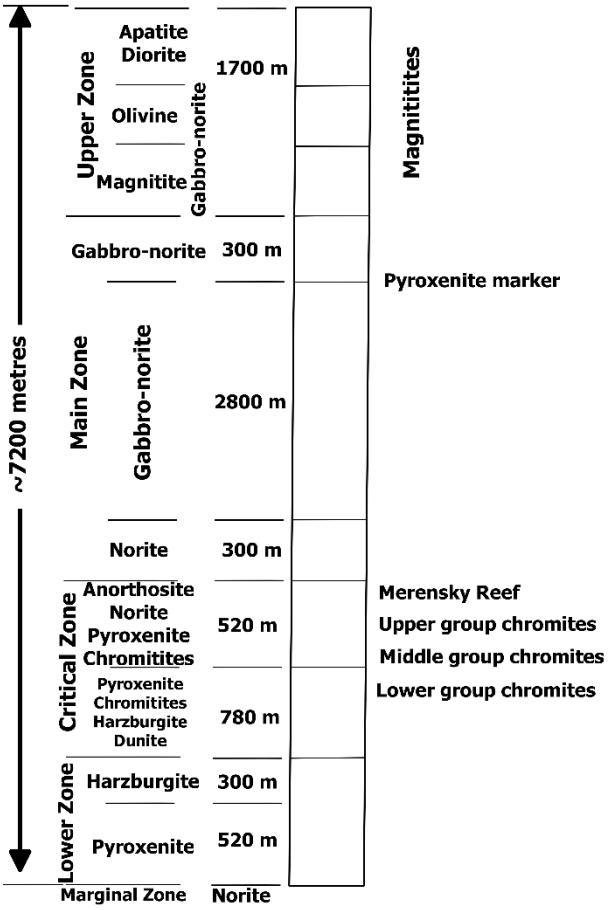

Figure 2.3: Simplified stratigraphic column of the Rustenburg Layered Suite of the western Bushveld Complex (after Clark et al., 2009).

2.3. Regional geology of the Merensky and UG2 reefs: western Bushveld Complex

There are two mineralized horizons being mined:

- The Merensky Reef includes various layers, namely the Merensky pegmatoid, Merensky chromitite layer and Merensky pyroxenite (Lougher and Mellowship, 1991). The Merensky Reef is generally composed of an upper feldspathic pyroxenite, overlying a thin basal chromitite stringer, followed by an anorthosite to norite footwall. Locally, this is termed a "pyroxenite reef" (Figure 2.4). Occasionally, a pegmatoidal pyroxenite and a second chromitite stringer may be developed between the feldspathic pyroxenite and the footwall units. This is termed a "pegmatoid reef" (Figure 2.5) (Wilson and Anhaeusser, 1998).

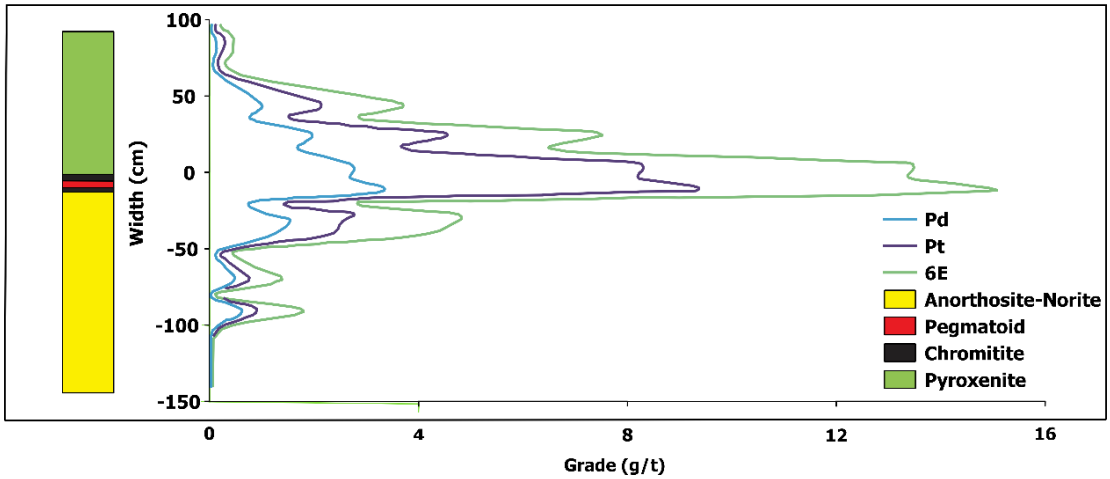

Figure 2.4: Grade distribution (in grams per ton) vs reef width in the Merensky pyroxenite reef (after Implats, 2015).

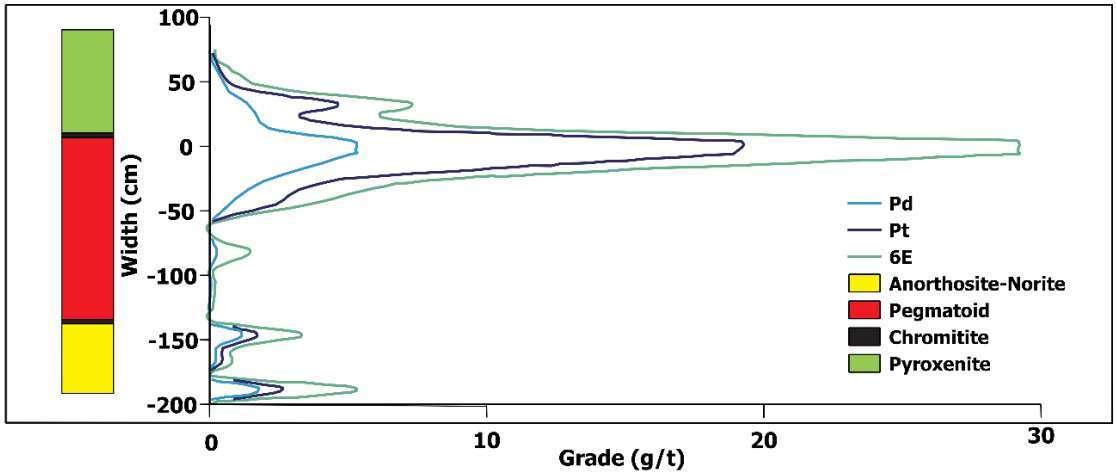

Figure 2.5: Grade distribution (in grams per ton) vs reef width in the Merensky pegmatoid reef (after Implats, 2015).

- The UG2 chromitite layer consists of chromitite and pegmatoid units. The UG2 Reef is represented by a coarse plagioclase-orthopyroxene pegmatoid layer, the base of which may grade into a coarse pyroxenite (Leeb-Du Toit, 1986). The thickness of the UG2 Reef varies from 20 cm to 200 cm, but averages approximately 50 cm. The absence of coarse pyroxenite below the UG2 chromitite layer would indicate that the layer is potholed (Lougher and Mellowship, 1991). The UG2 Reef is defined as a main chromitite layer, with most of the PGM and base metal mineralization confined to this unit, followed by a poorly mineralized pegmatoidal pyroxenite footwall (Figure 2.6). The hangingwall to the main chromitite layer is a feldspathic pyroxenite containing up to four thin weakly – mineralized chromitite layers.

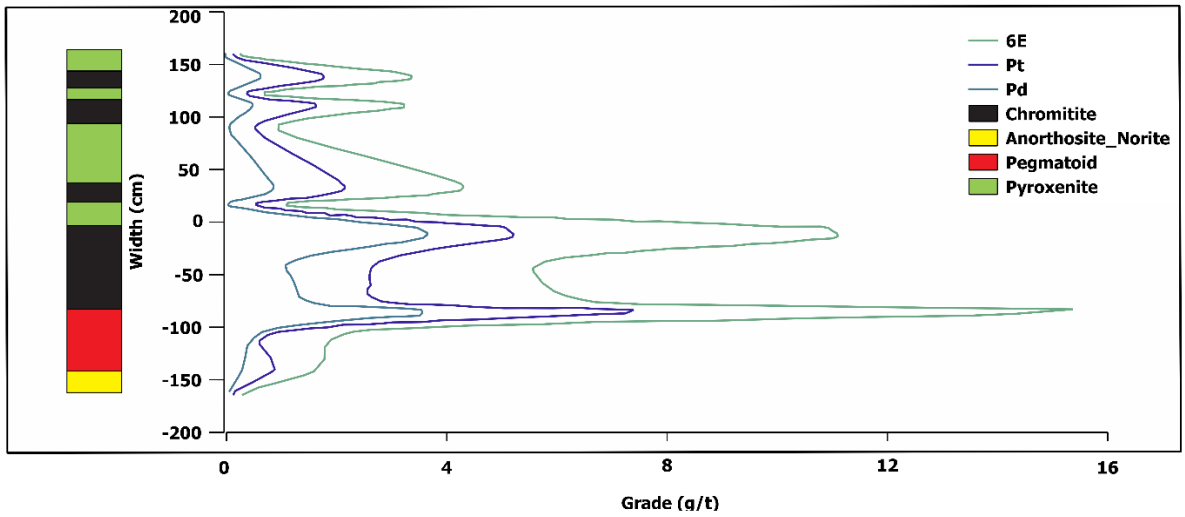

Figure 2.6: Grade distribution (in grams per ton) vs reef width in the UG2 chromitite reef (after Implats, 2015).

2.3.1. Geological structures

The reefs' composition may be disrupted by slumps (potholes), faults, dykes and iron-rich ultramafic pegmatites (IRUPs). These features are accounted for in the mineral reserve and resource statements as geological losses. When converted to reserves through the ore evaluation process, they contribute to the dilution or absence of the mineralized horizons (Implats, 2015).

2.3.1.1. Dykes

Dykes are sheet-like intrusions that are generally steeply dipping. Typical orientation of dykes in the area is NW – SE orientation and a thickness range of 15 – 25 m (Qamata and Steenkamp, n.d). They are either forced into cracks or create their own cracks due to hydrodynamic pressure. Dykes indicate areas of potentially poor ground conditions (Lougher and Mellowship, 1991). The three types of dykes encountered in the Impala lease area, include pegmatite dykes, dolerite dykes and lamprophyre dykes (Leeb-Du Toit, 1986). These dykes, in conjunction with other geological structures, can result in poor hanging wall conditions.

2.3.1.2. Potholes

Potholes are transgressive circular to elliptical depressions with gentle (seam rolling) to steep inclined walls (limb pinching) (Figure 2.7) (Ballhaus, 1988). These structures are thought to be formed by strong eddy currents and the scouring action of early-formed pyroxene crystals

eroding the floor rocks (Leeb-Du Toit, 1986). Therefore, they occur on all horizons where a heavy pyroxenite or chromitite layer overlies an anorthosite. Footwall layers may be entirely absent and hangingwall layers may be thickened. There is a marked increase in the density of joints and minor faults at the edges of potholes, with their occurrence being in a nonpredictable pattern (Scheiber-Enslin and Manzi, 2018). Pothole diameters range from, but not limited to, 10 – 60 m and depending on the size of potholes, falls of ground can vary from a few square meters to a complete panel collapse (Ledwaba, 2012; Scheiber-Enslin and Manzi, 2018). Potholes are normally not mined due to associated strata control problems, their geological complexity, and the additional cost of mining off-reef. The ground around potholes serves as regional stability pillars.

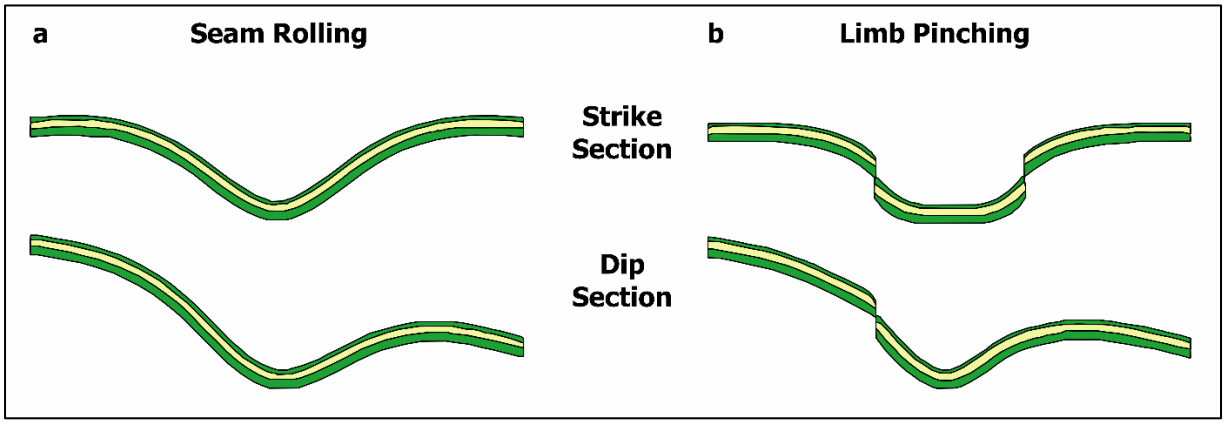

Figure 2.7: a) Slump/rolling behavior and b) chromitite layer steepening and pinches (after Qamata and Steenkamp, n.d).

2.3.1.3. Faults and joints

Faults are often filled with soft material such as clay and form weak zones. North and northwest trending faults are dominant, and dips encountered tend to average from 70º to 80º. Poor ground conditions are most frequently associated with faults which contributed significantly towards instabilities experienced early on in the life of the mine (Ledwaba, 2012). Many of the north-north-west striking dykes in the western Bushveld fall along faults and are of Pilanesberg age, 1450 – 1200 Ma (Scheiber-Enslin and Manzi, 2018).

The following types of faults are noted at Impala lease area (Leeb-Du Toit, 1986):

- Normal faulting occurs when the dip of the fault and the throw along the fault are in the same direction and results in loss of ground.

- Reverse faulting occurs when the dip of the fault and the throw along the fault are in the opposite direction and results in a gain of ground.

- Lateral faulting occurs when horizontal movements occur along a fault plane. Vertical displacements can often be observed due to reef dip and rolls in the reef being displaced. Fault zones have variable dips and throws along the fault plane.

Joints are breaks in the rock which do not displace the strata. They may be infilled, and their surfaces are often weathered (Leeb-Du Toit, 1986). Joints break up the hangingwall and footwall strata surrounding the reef plane. The joint density is prevalent near faults, dykes and potholes.

2.3.1.4. IRUPs

The iron-rich ultramafic pegmatites (IRUPs) comprise a suite of coarse-grained rocks that form discordant bodies within the Bushveld Complex layered sequence (Figure 2.8). The pegmatites are composed largely of clinopyroxene and iron-rich olivine together with ilmenite and Ti-magnetite (Scoon and Mitchell, 1994). Spatially correlated with potholes, their size ranges from a few tens to hundreds of meters (Scheiber-Enslin and Manzi, 2018).

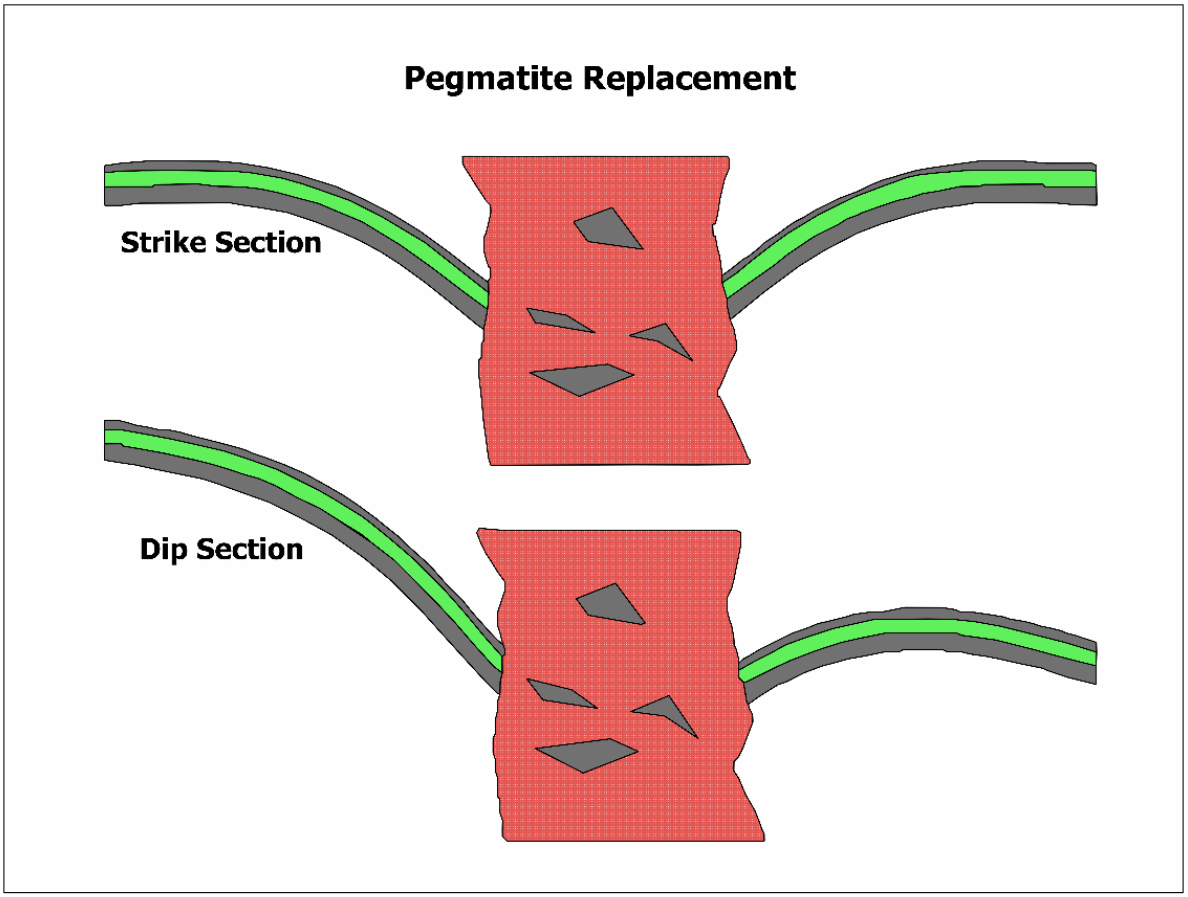

Figure 2.8: Pothole type associated pegmatoid body (after Qamata and Steenkamp, n.d).

3. The seismic reflection method

3.1. Background

Reflection seismology method is a powerful geophysical tool used to explore for minerals and hydrocarbons. It uses the principles of seismology to produce high resolution images of the subsurface from the reflected seismic waves (Figure 3.1). At its core, the reflection seismic technique involves generation of seismic waves and measuring the wave travel times from the seismic source, down to the reflector and back to the array of receivers (Telford et al., 1990).

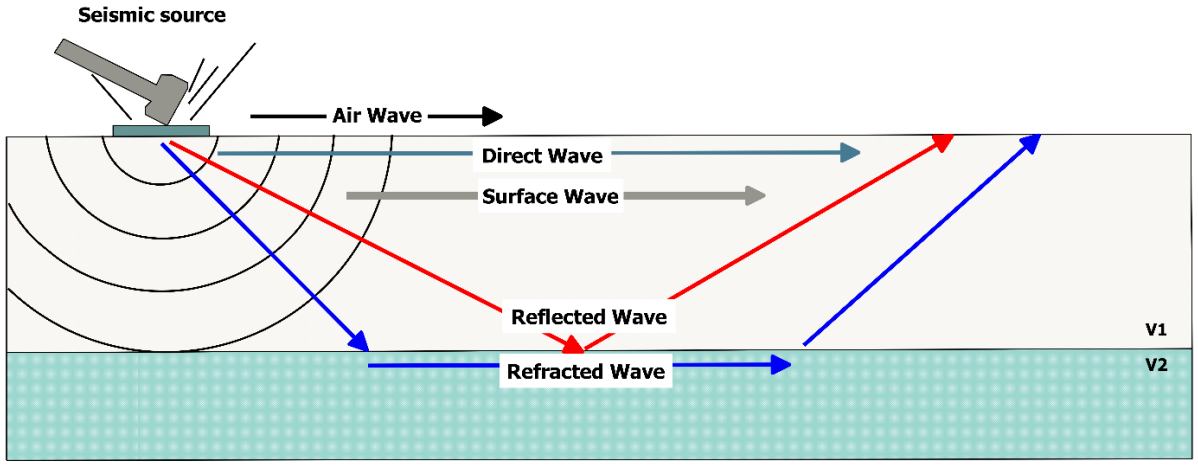

Figure 3.1: Major forms of seismic waves built from the characteristics of wave propagation, as governed by Snell's law (after Parkseismic.com, n.d)**.**

At an interface, wave propagation and interaction are governed by Snell's law (Figure 3.2). The velocities for Primary or P – waves (V_p) and Secondary or S – waves (V_s) are given by:

$$V_P = \sqrt{\frac{k+\frac{4}{3}\mu}{\rho}} \qquad (1)$$

$$V_S = \sqrt{\frac{\mu}{\rho}} \qquad (2)$$

where k is the bulk modulus, ρ is the bulk density and μ is the shear modulus.

The P–wave velocity is generally greater than the S-wave velocity (~ 70 % of P-wave velocity). Since the propagation of S – waves involves a shear strain, they cannot pass through fluids where $\mu = 0$ (Dentith and Mudge, 2014).

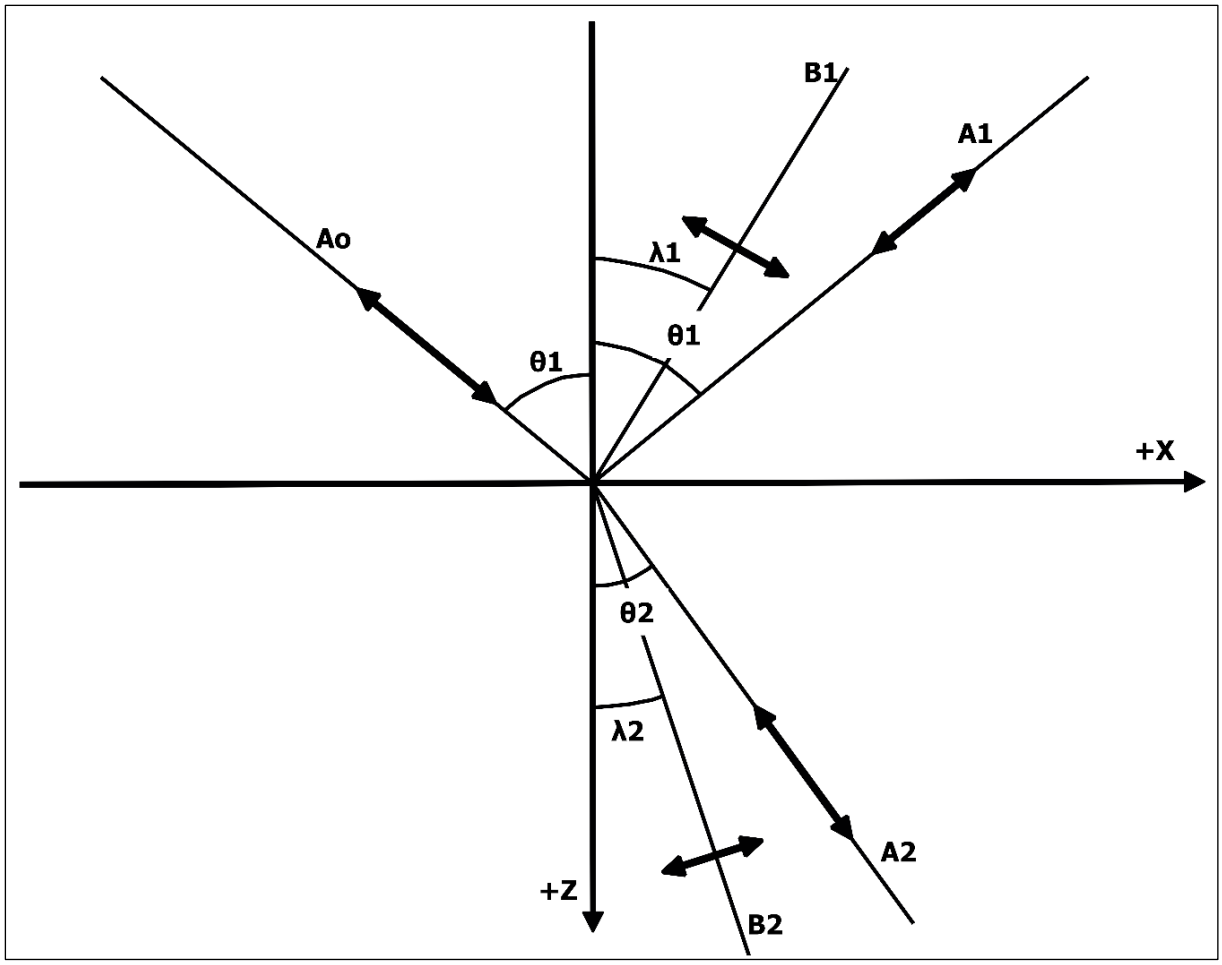

Figure 3.2: Wave generated at an interface by an incident P – wave (Telford et al., 1990).

where A_0 is the incident amplitude, A_1, A_2 are the reflected and refracted amplitudes and θ_1, θ_2 are angles of the reflected and refracted P-waves. B_1, B_2 are the reflected and refracted amplitudes and λ_1, λ_2, angles of the reflected and refracted S-waves, respectively. α_i, β_i represent the P-wave and S-wave velocities.

The reflection and transmission coefficients give the ratio between the incident amplitude, the transmitted amplitude and the reflected amplitude. Boundary conditions allow calculations of the partition of wave energy into reflected and refracted waves, which are needed to define the transmission and reflection coefficients for elastic waves (Telford et al., 1990). These

coefficients depend on the contrasts in: velocity, the angle of the incident wave and the rock's bulk density derived from the Zoeppritz equations.

From Snell's law:

$$\frac{\sin\theta_1}{\alpha_1} = \frac{\sin\theta_2}{\alpha_2} = \frac{\sin\lambda_1}{\beta_1} = \frac{\sin\lambda_2}{\beta_2} = p \qquad (3)$$

where p (ray parameter) is constant for reflected and transmitted waves and corresponds to the component of the slowness that is parallel to the interface.

The corresponding equations in terms of amplitude derived by Zoeppritz (1919) are given by:

$$A_1\,cos\theta_1 - B_1\,sin\lambda_1 + A_2\,cos\theta_2 - B_2\,sin\lambda_2 = A_0\,cos\theta_1 \qquad (4)$$

$$A_1\,sin\theta_1 + B_1\,cos\lambda_1 - A_2\,sin\theta_2 + B_2\,cos\lambda_2 = -A_0\,sin\theta_1 \qquad (5)$$

$$A_1Z_1\,cos2\lambda_1 - B_1W_1\,sin2\lambda_1 - A_2Z_2\,cos2\lambda_2 - B_2W_2\,sin2\lambda_2 = -A_0Z_1\,cos2\lambda_1 \qquad (6)$$

$$A_1\gamma_1W_1\,sin2\theta_1 + B_1W_1\,cos2\lambda_1 + A_2\gamma_2W_2\,sin2\theta_2 - B_2W_2\,cos2\lambda_2 = -A_0\gamma_1W_1\,sin2\theta_1 \qquad (7)$$

where $\gamma_1 = \beta_i/\alpha_i$, $Z_1 = \rho_i\alpha_i$, $W_i = \rho_i\beta_i$, $i = 1, 2$.

For a plane at normal incidence where $B_1 = B_2 = 0\ and\ \theta_1 = \theta_2 = 0$, equations (4) to (7) can be described as:

$$A_1 + A_2 = A_0 \qquad (8)$$

$$A_1Z_1 - A_2Z_2 = -A_0Z_1 \qquad (9)$$

and their solutions are the reflection and transmission coefficients, which are given by

$$R: \frac{A_R}{A_0} = \frac{v_2\rho_2 - v_1\rho_1}{v_2\rho_2 + v_1\rho_1} = \frac{Z_2 - Z_1}{Z_2 + Z_1} \quad (10)$$

$$T: \frac{A_T}{A_0} = \frac{2v_1\rho_1}{v_2\rho_2 + v_1\rho_1} = \frac{2Z_1}{Z_2 + Z_1} \quad (11)$$

Where A_R and A_T are the reflected and transmitted amplitudes respectively, the product $Z = \rho v$ is the acoustic impedance, and Z_1 and Z_2 are the acoustic impedances of the first and second medium, respectively. The Zoeppritz equations state that the reflected amplitude compared with the incident amplitude varies directly with the change in acoustic impedance (Sheriff and Geldart, 1995).

The reflected and transmitted incident energy are defined as follows:

$$E_R = \left(\frac{Z_2 - Z_1}{Z_2 + Z_1}\right)^2 \quad (12)$$

$$E_T = \frac{4Z_1Z_2}{(Z_2 + Z_1)^2} \quad (13)$$

$$E_R + E_T = 1 \quad (14)$$

When $Z_1 > Z_2$, the sign of R and value of T will change, but E_R and E_T remain unchanged, hence the partition of energy does not depend on which medium contains the incident wave.

Seismic data resolution

Vertical resolution involves the capability to resolve two closely-spaced interfaces as separate reflectors. The thickness of a layer must be greater than one-quarter of the dominant wavelength for the top and bottom of the layer to be discerned. This is the conventional criterion for the acceptable threshold of the vertical resolution (λ/4, Rayleigh criterion). The dominant wavelength of seismic waves is given by:

$$\lambda = \frac{v}{f} \quad (15)$$

where, v is the velocity and f is the dominant frequency. Lateral resolution refers to a minimum distance between two reflecting points on the horizontal plane that can be recognized as distinct (Yilmaz, 2001). The Fresnel zone governs the lateral resolution, Figure 3.3, which is a subsurface area that reflects energy to the surface within a time of half the dominant period (T/2). Separate reflectors within the Fresnel zone are not individually resolvable. A quarter (1/4) of the signal's wavelength is the conventional criterion for horizontal resolution. A recorded reflection at the surface does not come from a subsurface point, but from a disk – shaped area, which has a dimension equal to the Fresnel zone (Sheriff and Geldart, 1995).

The radius of the Fresnel zone (r) is given by:

$$r = \sqrt{\frac{z_0 \lambda}{2}} = \frac{v}{2}\sqrt{\frac{t_0}{f}} \qquad (16)$$

where $\boldsymbol{z_0}$ is the depth of the reflecting interface and $\boldsymbol{t_0 = z_0/v}$ is the two-way travel-time and f is the dominant frequency. This equation shows that higher frequencies give better lateral resolution, which deteriorates with depth. The size and shape of the Fresnel zone is dependent on the position of the source and receiver, the velocity distribution, wavelength, the depth, dip, and curvature of the reflector (Brouwer and Helbig, 1998).

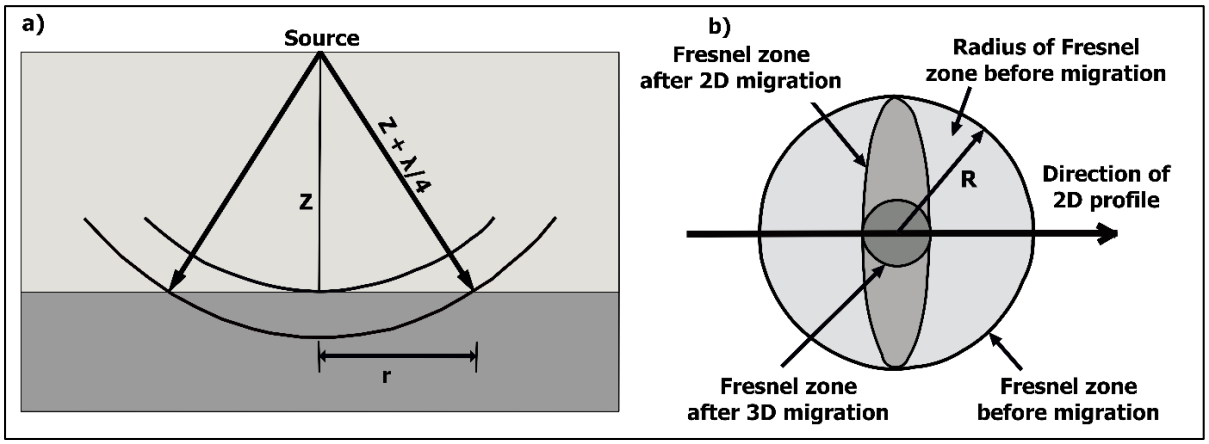

Figure 3.3: a) 2D view illustration of the first Fresnel zone. b) Map view illustration of the Fresnel zone before & after 2D and 3D migration (after Chaouch and Mari, 2006).

As described by Manzi (2013), the seismic reflection method has three main components:

- **Acquisition**: The reflection seismic technique uses energy sources (e.g. sledgehammer, air gun, dynamite, vibroseis trucks, etc.) to inject seismic waves into the Earth's subsurface. The waves may be reflected by lithological and structural boundaries such as unconformities, conformities and faults. The reflected waves result from the abrupt changes in the rocks' elastic properties, which are then recorded by the receivers (geophones) on the surface.

- **Processing**: The main objective of seismic data processing is to suppress noise, enhance the reflected signal, move (or migrate) seismic reflections to their true positions in time and space, and thus produce the best possible image of the subsurface.

- **Interpretation**: reflection seismic data interpretation requires an understanding of the subsurface formations and their effect on wave propagation. This data interpretation is enhanced by applying seismic attribute analysis.

3.2. Survey design and acquisition

The main objective of a seismic survey is to create a homogeneous coverage of subsurface reflection points across the area of interest. The challenges include obtaining high-resolution data with maximum resolution at depths, at a cost that is substantially more appealing than the drilling alternative (Gillot et al., 2005). The typical performance – constraining factors are the design parameters (e.g. of source and receiver locations), field surface conditions (dams, infrastructure, etc.), the target geometry and costs.

Four 2D reflection seismic profiles, spaced approximately 700 meters apart were acquired on the mining lease between 1992 and 1996. During 1998 to 2000, a 3D seismic survey that covered the whole area of interest was conducted. The 3D seismic survey was merged with four 2D seismic profiles to improve coverage (Ledwaba, 2012). In 2008 Compagnie Générale de Géophysique and Veritas Digicon Inc. (CGGVeritas) conducted a surface 3D seismic survey for Impala using a vibroseis source. The company report detailing the acquisition and processing parameters was not available to be used for this study. Table 1 and Table 2 only report acquisition and processing parameters respectively that were extracted from the

seismic cube prior to seismic interpretation. A Trimble 5700 dual frequency GPS receiver and the real-time kinematics (RTK) method were used to survey the seismic stations and lines. The RTK method has three components, a GPS base station, GPS rovers and radio link between the base station and the rovers. The radio link transmits the GPS observations from the base station to the rover, then the rover combines the base station with its own observation to process and produce coordinates in real time (Ledwaba, 2012).

Table 1: The 2008 3D reflection seismic survey acquisition parameters

Recorded by	**CGGVeritas**	**Crew**
Instrumentation	System	Sercel SN 388
	Geophones	10 Hz
	Data format	SEGD
	Record length	6 s
	Sample interval	2 ms
	System polarity	SEG standard
Parameters	Bin dimensions	25 x 25 m
	Survey pattern	Orthogonal
	Shot line separation	240 m
	Shot line direction	9.51°
	Shot line angle to receiver line	90°
	Shot point separation	30 m
	Total number of shot points	25544
	Receiver line separation	180 m
	Receiver line direction	99.51°
	Receiver point separation	30 m
	Total number of receiver points	33113
	Array	Linear, 95 receiver points
	Array length	Variable (36–85 m)
Source	Vibroseis	Two vibrators
	Sweep	24 s, 10-160 Hz

3.3. Data processing

In the processing of seismic reflection data, the three fundamental steps are, stacking, deconvolution and migration (Dentith and Mudge, 2014). Stacking merges the recorded traces at finite source–receiver offsets into a smaller number of equivalent zero-offset recordings thus improving the signal-to-noise ratios. Deconvolution manipulates the characteristics of the signal wavelet to correct for wave attenuation during propagation through the subsurface. Migration moves features in the seismic section to their correct relative physical positions, to allow the seismic sections to better represent the subsurface geology.

Some of the sources of noise that can be removed during processing are:

- **Airwaves**: airwaves travelling at the speed of sound in air (roughly 330 m/s), directly from source to receiver.

- **Surface waves** (commonly referred to as ground roll): Rayleigh wave propagating near the surface, from source to receiver. Characteristics include low velocity and high amplitude.

- **Refracted waves** (head wave): used in seismic refraction tomography. This wave travels along a buried interface and can produce oscillations parallel to the interface that are detectable (Sheriff and Geldart, 1995).

- **Cultural noise**: environmental noise such as weather effects, planes, electrical pylons, etc., that are all detectable by the geophones.

Table 2: Processing steps done by CGG Veritas using Pre-stack time migration with post-stack processing applied on the data.

Processing Route	**Parameters**
Data reformat	From SEGD to SEGY
Trace editing	Air-blast attenuation applied
Trace editing	Air-blast attenuation applied
Geometry application	Source, receiver, and offsets assigned to each trace
First-break picking and statics	Primary static computation (DP=1400 m, Vr=5500 m/s, Vo = 1000 m/s).
1st RMS velocity analysis	Fixed datum plane at 500 m x 500 m grid
Minimum phase conversion	From zero phase to minimum phase wavelet
Noise attenuation	3D FKxKy filtering on cross-spread gathers
Amplitude recovery: spherical divergence correction	1/(TV^2), where V=6500 m/s
Amplitude versus offset gain correction	Average curve of amplitude versus offset
Surface consistent gain correction	G(T)= 200.log10 (A/5000); Time window: 250-1000 ms.
Frequency/Amplitude dependent noise attenuation	Attenuation on the whole data: threshold = 4 (from 0 to 3s) and threshold = 2 (from 3 to 4 s)
Zero-phase surface consistent spiking deconvolution	Low frequency side: Cut-off 8 Hz; Operator design window: 200 – 2700 ms
1st pass residual static corrections (medium wavelength)	24 × 24 bins sub-volume, time window: 250-2000 ms
2nd pass RMS velocity analysis	250 m (inline) x 250m (cross-line) grid; datum =1400 m a.m.s.l
2nd pass residual static corrections (short wavelength)	12 × 12 bins sub-volume; time window: 250-2000 ms
3D Dip moveout (DMO) velocity analysis	Iterative link to velocity analysis
First-pass PSTM velocity analysis	DMO velocities removed and PSTM velocities picked
PSTM	Full 3D Kirchhoff using velocity model from PSTM velocities
Pre-stack time migration (PSTM) flow	
Second-pass PSTM velocity analysis	Second pass PSTM velocities picked
NMO correction	35% stretch mute
Stacking	
Bandpass frequency filter	Time variant Ormsby zero phase filter, 0-1400 ms: 15/20-80/90 Hz
Amplitude equalization	Operator length: 0 to 500 ms; 500 ms up to 5000 ms

3.4. Seismic data interpretation

Interpretation is concerned with the quantitative and qualitative reconstruction of the subsurface from the intermediate results of data processing (Yordkayhun, 2008). Initially, conventional picking of strong reflections and other visible structures such as faults, folds, and potholes are done throughout the seismic dataset, usually with the aid of some lithological data, e.g. borehole log data.

- Manual picking involves the manual interpretation of horizons across the data, along the inlines, crosslines, time slices and traverses (Admasu, 2008).

- Interpolation is a horizon-picking technique that assumes that the horizon is linear (or planar) and very smooth between control points (Dorn, 1998).

- Automatic picking (or autotracking) technique involves placing seed points on inlines and/or crosslines in the seismic volume, which are then used as parameters for the autotracking algorithm (Dyrendahl, 2018).

3.5. Seismic trace attributes

Seismic attributes are quantities that are measured or computed from seismic data. These attributes are used to highlight geological effects thus leading to a quicker data analysis. There are many attributes and they can be classified in a number of ways, but for our purposes we will classify them into two basic categories (Taner et al., 1994):

- **Physical attributes**: seismic attributes that directly affect the physical characteristics of the subsurface and thus relate to wave propagation and lithology. These include frequency, phase and amplitude.

- **Geometric attributes**: seismic attributes that enhance the visibility of the geometrical nature of the seismic reflectors. These are dip, dip-azimuth, curvature, variance, chaos and edge detection.

In Schlumberger's Petrel Exploration and Production (E&P) Software Platform 2015 (henceforth referred to as Petrel), classification of attributes is dependent on the input data

and subsequently the libraries of grouped attributes that enhance similar features. Unlike the previously mentioned classification of attributes based on input data characteristics (physical and geometric), Petrel has two libraries of attributes available, namely: surface or horizon attributes and volumetric attributes. Some of the seismic attributes used in this study are described below.

3.5.1. Surface attributes

3.5.1.1. Confidence classification: surface stability index

In Petrel, the attribute creates a confidence map for the horizon by calculating the surface stability index. This is calculated by comparing nearby picks in relation to their depth. It highlights areas which fluctuate in elevation. The input value assigned is the radius of the moving window which is used to define points that are included in the calculation. Larger values are used to compare points more generally as smaller values are more sensitive to local changes in the elevations of the interpreted horizon or surface.

In the resultant output value property, some areas would represent high confidence zones (as indicated by certain colours) while other areas represent low to intermediate confidence zones (assigned to a specific colour).

3.5.1.2. Dip and dip-azimuth attributes

Geologically, strike is defined as the compass – bearing of a horizontal line on a dipping layer, and dip is the angle of the inclination of the bed measured perpendicular to the strike direction. Mathematically, these are defined as:

$$Dip = \sqrt{\left(\frac{dt}{dx}\right)^2 + \left(\frac{dt}{dy}\right)^2} \quad (17)$$

$$Dip - azimuth = arctan\left(\frac{\left({}^{dt}/_{dx}\right)}{\left({}^{dt}/_{dy}\right)}\right) \quad (18)$$

where ${}^{dt}/_{dx}$ and ${}^{dt}/_{dy}$ are the dip in the x and y direction respectively (Manzi, 2013).

These attributes are used to estimate the dominant attribute of the strata, represented by dip and azimuth. In Petrel, the local structural dip and dip-azimuth can be computed following three different computation methods with different complexities (Iske and Randen, 2005):

- **Gradient method**: this method calculates the gradient vector using a different operator for each of the three dimensions of space (inline, crossline and time). The calculated gradient vector is normal to the considered seismic event. The dip (0° to 90°) is measured from the z – axis to the gradient vector while the azimuth (0° - 360°) is the angle of the vertical projection of the gradient vector measured clockwise from the inline axis (Azevedo and Pereira, 2009).

- **Event method**: this method computes the downslope dip and azimuth of the estimated event. The gradient is assumed to be perpendicular to the event. This method numerically calculates the gradient using the same approximation of the gradient method (above) but by convention, the event normal should always points upwards. The azimuth ranges are 0° - 360° while the dip ranges from 0° - 90°.

- **Principal component analysis**: this method aims to reduce the number of variables of a data set, while preserving as much information as possible. It initially estimates the data's gradient vector, then the local gradient covariance matrix is computed and finally the eigenvector and eigen values from the covariance matrix are used to identify the data's principal components. Dip and azimuth angles will behave like the event method (above); i.e. azimuth (0° - 360°) and dip (0° - 90°) (Randen et al., 2000).

3.5.1.3. Edge detection attribute

The edge detection attribute essentially combines the dip and azimuth variations, normalized to the local noise of the picked horizon grid (Manzi, 2013). The edge detection attribute assists the user in the identification of subtle discrete edges, thereby increasing confidence in the modelled fault network, and helps the user identify potential relay zones and fault intersections.

3.5.2. Volumetric attributes

3.5.2.1. Structural smoothing

The structural smoothing attribute applies a 3D Gaussian filter to the input signal. This is controlled by the local structure to increase the seismic reflectors' continuity (Othman et al., 2016). Using principal component analysis, a structure-orientated filter reduces the noise content without losing information related to edges (e.g. faults, dykes, etc.) within the data. The Gaussian smoothing operator, used in Petrel 2015, has the following expression:

$$h_G(k) = \frac{1}{\sqrt{2\pi\sigma}} \exp\left(-\frac{1}{2}\frac{k^2}{\sigma^2}\right) \qquad (19)$$

where k is the distance from the origin in horizontal distance, while σ defines the width of the smoothing filter, which is user-defined and is adjustable to the data in the vertical (time or depth) and horizontal (inline, crossline) directions.

3.5.2.2. Dominant frequency

The dominant frequency attribute is a complex trace attribute that is calculated as the hypotenuse between the instantaneous frequency and instantaneous bandwidth (Taner et al., 1994). This method is useful in detecting signs of frequency absorption effects caused by fracturing, revealing subtle frequency trends associated with changing stratigraphy or lithology (Chen and Sidney, 1997). This represents the root mean square frequency of the amplitude spectrum, defined as:

$$\omega_{RMS} = \sqrt{\omega_B^2 + \omega_c^2} \qquad (21)$$

where ω_B is the instantaneous bandwidth, described as the absolute value of the derivative of the envelope with time divided by the envelope, over a user-defined window. ω_c is the instantaneous frequency, defined as the rate of change in time of the instantaneous phase over a user-defined window.

3.5.2.3. Graphic equalizer

The graphic equalizer attribute is a user-defined band-pass frequency filter that can be applied to the input volume attenuate or enhance specific frequencies, or frequency intervals,

to improve the continuity of the reflections and the signal-to-noise ratio (Zhang et al., 2017). Prior to the graphic equalizer attribute, the dominate frequency attribute is first derived to observe the frequency distribution in the data.

In Petrel, this filtering is executed in the frequency domain with the following equation:

$$F(\omega) = \mathrm{W}(\omega) * |A_\omega| e^{-i\emptyset(\omega)} \qquad (20)$$

where W(ω) is the user-defined linear interpolation frequency-sampled weighting function and the frequency signal is represented by its coefficients expressed as magnitude A_ω and phase angle($\emptyset$), while ω is the radian frequency (Azevedo and Pereira, 2009). The weighting function is created interactively in Petrel.

3.5.2.4. Variance

The variance attribute is an edge detection and imaging method that estimates local variance from the input signal. Edges imply disjointedness in the horizontal continuity of the amplitude. Variance is applied as a stratigraphic attribute as it can highlight depositional features such as reefs and channels (Azevedo and Pereira, 2009).

Petrel uses a patented algorithm introduced by van Bemmel et al. (2000) which computes the local variance of the input signal through a multi-trace window with a user-defined size:

$$\sigma_t^2 = \frac{\sum_{j=t-\frac{L}{2}}^{j=t+\frac{L}{2}} W_{j-t} \quad \sum_{i=1}^{I} (x_{ij} - \overline{x_j})^2}{\sum_{j=t-\frac{L}{2}}^{j=t+\frac{L}{2}} W_{j-t} \quad \sum_{i=1}^{I} x_{ij}{}^2} \qquad (22)$$

where x_{ij} is the sample value at horizontal position i and vertical time sample j. $W_{j-t}$is the vertical smoothing term across a window length L.

3.5.2.5. Chaos

The chaos attribute considers the chaotic signature contained within the seismic data. It computes the discordance in the dip and dip-azimuth orientations estimated using the

principal component method (Barbato, 2012). Chaotic texture in the seismic signal can be used to illuminate faults and discontinuities due to local geologic features that are affected by intrusions, reef texture, channel infill, etc. If each C-matrix contains three eigen vectors with their respective eigen values (λ), then the largest eigen value (λ_{max}) is representative of the dip and dip azimuth of the event (this event is determined by calculating the local dip and azimuth, during the dip guidance step) (Randen and Sønneland, 2005).

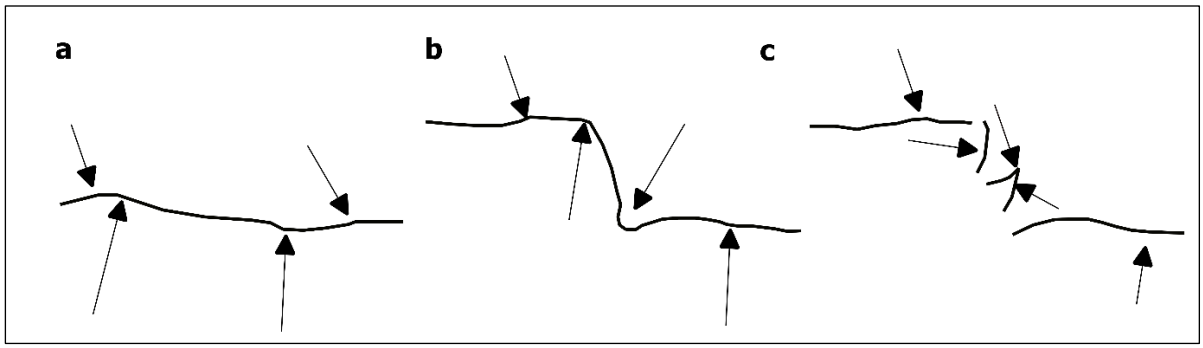

Figure 3.4: a) Continuous reflector will show $\lambda_{max} >> \lambda_{mid} \approx \lambda_{min}$, b) Continuous reflector (with a bend) will show $\lambda_{max} \approx \lambda_{mid} >> \lambda_{min}$, c) Discontinuous reflector will show $\lambda_{max} \approx \lambda_{mid} >> \lambda_{min}$ (after Randen et al., 2001).

As Randen et al. (2001) explains, the difference between (λ_{max}) and the other two eigen values (λ_{mid} and λ_{min}) shows the level of "chaoticness" in the event.

3.5.2.6. Ant-tracking

The ant-tracking algorithm, based on the ant colony optimization first introduced by Colorni et al. (1991), is inspired by the behaviour of real ant colony systems in nature (Figure 3.5). The attribute uses the principles of swarm intelligence which explains how the ants finds the shortest path between the nest and a food source, without any visual cues, by communication using chemical pheromones (Ngeri et al., 2015).

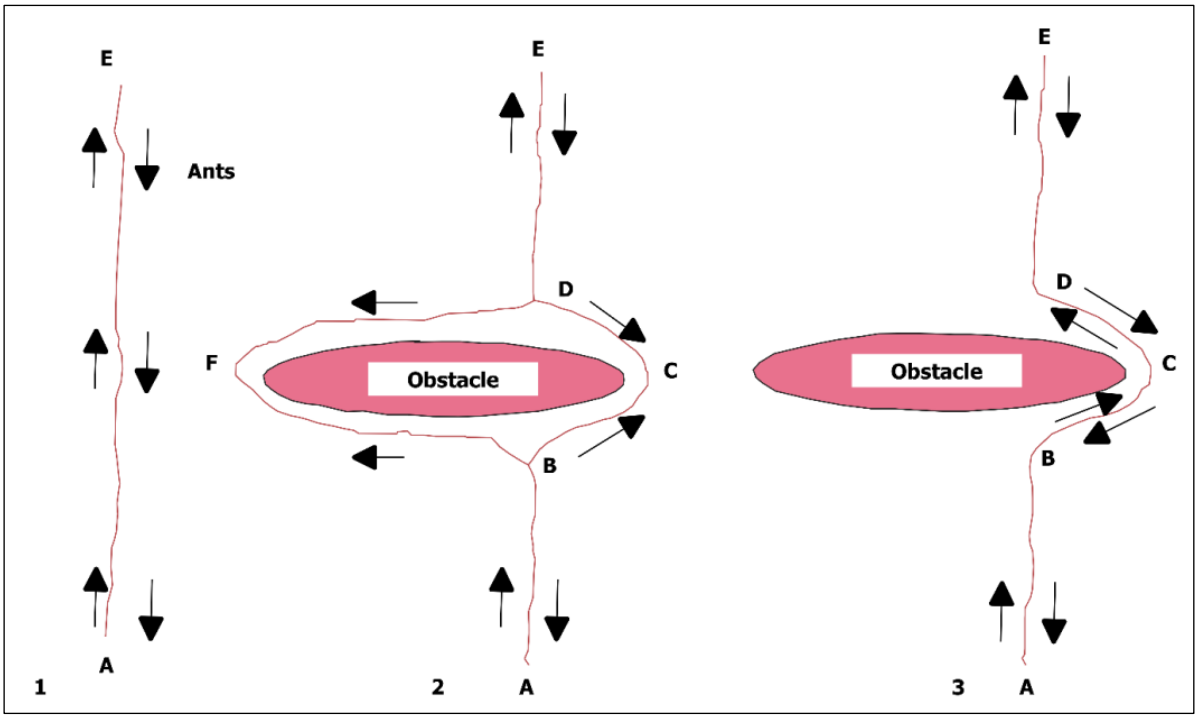

Figure 3.5: 1) Ant walking from nest (A) to food source (E). 2) an obstacle suddenly appears, and the ants must go around it. 3) The ants eventually choose the shorter path by a stronger pheromone trace on path ABCD than ABFD (adapted from Colorni et al., 1991).

The ant-tracking attribute is a patent-protected edge-enhancement algorithm, by Schlumberger, that uses a standard workflow to enhance edges (fractures, faults, and other linear features). This facilitates automatic and manual interpretation of these features. Intelligent software agents (ants) extract features in the seismic attribute matching the expected fault behaviour. Many of the ants will extract the correct fault information in the attribute, as it should fulfill this expected fault behaviour. The remaining reflectors and noise should be extracted by at most a few ants (in which case, should be deleted).

The general workflow for the ant-tracking attribute in Figure 3.6 involves:

- Data conditioning: to reduce spatial noise while preserving features of interest, usually by applying filtering.

- Edge detection: estimated using variance and chaos attributes.

- Edge enhancement (ant-tracking): edge surfaces extracted and written back to the volume, using the ant-tracking algorithm, resulting in an enhanced attribute volume.

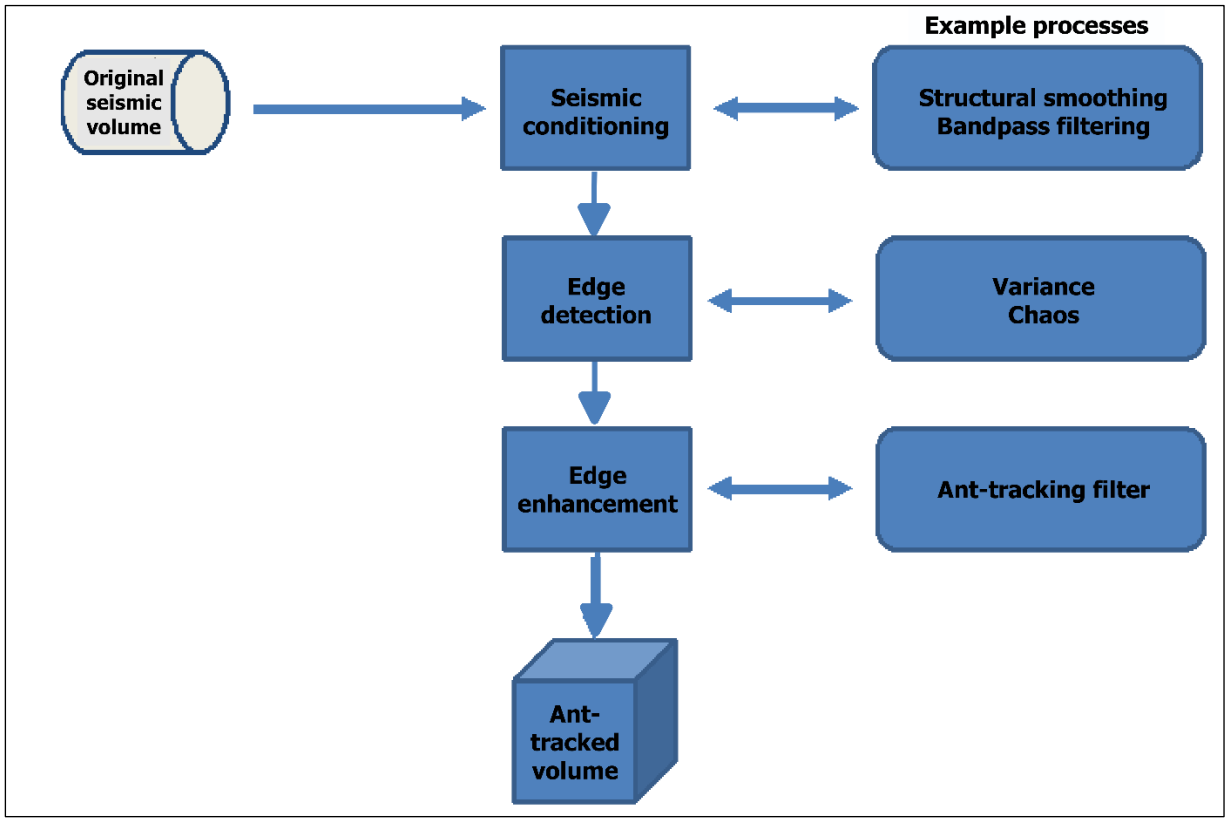

Figure 3.6: Schlumberger's standard ant-track workflow (after Kee et. al., 2017).

Two different predefined settings provided with the method are: passive or aggressive.

Passive Ants

The passive ant mode refers to a set of parameters where the swarm behaviour is conservative; the artificial ants require a strong signal to advance further in the volume. This mode is used when extracting only major regional fault zones in the data.

Aggressive Ants

The aggressive ant mode renders the ant agents added autonomy to explore and detect more subtle connections. This mode was used to extract major and subtle fault zones in the data. The list of single parameters is adjusted accordingly. It is possible to customize the behaviour

of the ant agents in custom mode, by specifying certain settings (described below) that govern the behaviour of the ants:

- Initial ant boundary (number of voxels)

  This parameter defines the initial distribution of agents, by specifying territorial radius around each ant in the number of voxels. Execution time is greatly dependent on this parameter as it defines the density of agents that are propagated through the volume.

- Ant track deviation

  This parameter controls the deviation threshold from a local maximum during tracking. The agents can only deviate 15 degrees from the initial orientation and adopt a planar shape.

- Ant step size

  This parameter defines, within each searching step, the number of voxels an ant agent advances for each increment. Increasing this value will allow an agent to search further at the expense of the resolution of the result.

- Illegal steps allowed

  Illegal steps allowed defines how far (as measured in steps) that an agent's track can continue without finding an acceptable edge value (a continuous local maximum) (Table 3).

- Legal steps required

  Legal steps required controls how "connected" a detected edge must be to help distinguish an edge from un-oriented noise. This parameter is used in combination with the “illegal steps allowed” parameter.

- Stop criteria

  This parameter refers to the percentage of “illegal steps” allowed throughout a single agent's life (for the entire search space).

Table 3: A list of values for the custom ant-tracking parameters.

Ant-tracking (Output)	**Ant-tracking (Output)**
Ant mode**: Passive**	Ant mode: **Aggressive**
Initial ant boundary**: 7**	Initial ant boundary: **5**
Ant-tracking deviation**: 2**	Ant-tracking deviation: **2**
Ant step size**: 3**	Ant step size: **3**
Illegal steps allowed**: 1**	Illegal steps allowed: 2
Legal steps required**: 3**	Legal steps required: **2**
Stop criteria (%)**: 5**	Stop criteria (%): **10**

4. Dataset and methodology

The processing workflow began with importing the processed 3D reflection seismic data into Petrel and DownUnder Geosolutions' DUG Insight seismic data interpretation software packages (Figure 4.1). The reflectors of interest were then picked throughout the volume to examine first order features. Lastly seismic attribute analysis was carried out to investigate subtle features that fall below the resolution limits.

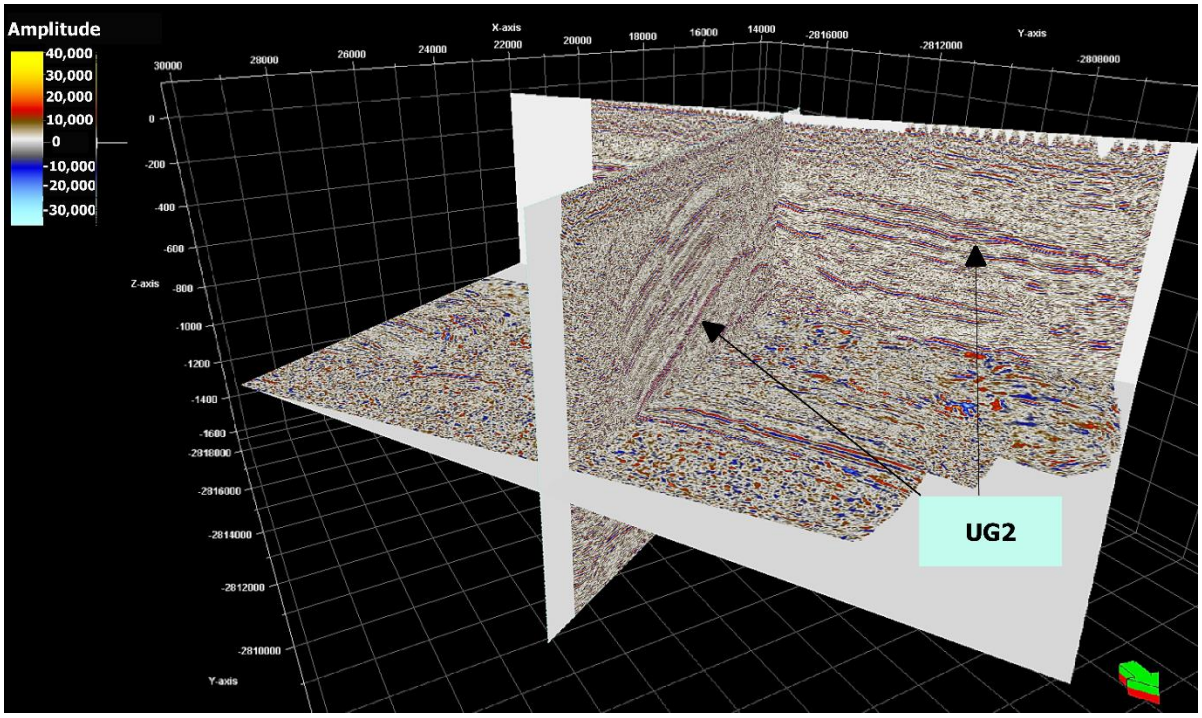

Figure 4.1: 3D view of the reflection seismic data (amplitude display) in the Petrel interpretation package.

Using the average velocity of the rocks of ~6500 m/s, frequency range of 30 Hz and 90 Hz, Rayleigh criterion, and equations (12) and (13), Table 4 shows the vertical and lateral resolution ranges of the data.

Table 4: Vertical and lateral seismic resolution range of the data using the average velocity (~6500 m/s), dominant frequency range (30 Hz – 90 Hz).

Vertical seismic resolution		
Frequency range	**Amplitude ($\lambda = \frac{v}{f}$)**	**Rayleigh criterion ($\lambda/4$)**
30 Hz	217 m	54 m
45 Hz	144 m	36 m
60 Hz	108 m	27 m
75 Hz	87 m	21 m
90 Hz	72 m	18 m
Lateral seismic resolution		
TWT	**Fresnel zone radius using 30 Hz**	**Fresnel zone radius at 90 Hz**
0.1 s	188 m	108 m
0.5 s	420 m	242 m
1.0 s	593 m	343 m
1.5 s	727 m	420 m

4.1. Forward modelling

The most common use of forward modelling is to verify structural and stratigraphic interpretations (Mellman and Kunzinger, 1992). Synthetic seismic traces are created using velocity data from sonic logs and density logs from borehole data. These approximate and calibrate the seismic trace that propagated in the proximity of the boreholes (Rekoske and Hicks, 1992).

The synthetic trace can be expressed by the convolutional model

$$\boldsymbol{T(t) = R_0(t) * w(t) + n(t)} \qquad (21)$$

where $\boldsymbol{T(t)}$ is the seismic trace, $\boldsymbol{R_0(t)}$ is the reflection coefficient series, $*$ is convolution, $\boldsymbol{w(t)}$ is the wavelet and $\boldsymbol{n(t)}$ is noise.

The P – wave sonic velocities for the mafic rocks fall in a range of ~ 6500 m/s to greater than 7000 m/s, thus reflecting the slight porosity of these units. The densities of the Rustenburg Layered Suite lithologies fall within the extremes of pyroxenite and dunite (3.28 ± 0.04 g/cm^3) to anorthosite (2.80 ± 0.10 g/cm^3) and pure oxides (Figure 4.2) (Campbell, 2011). Therefore, reflection seismic mapping of mafic unit lithologies greatly depends on density zoning than on velocity variations.

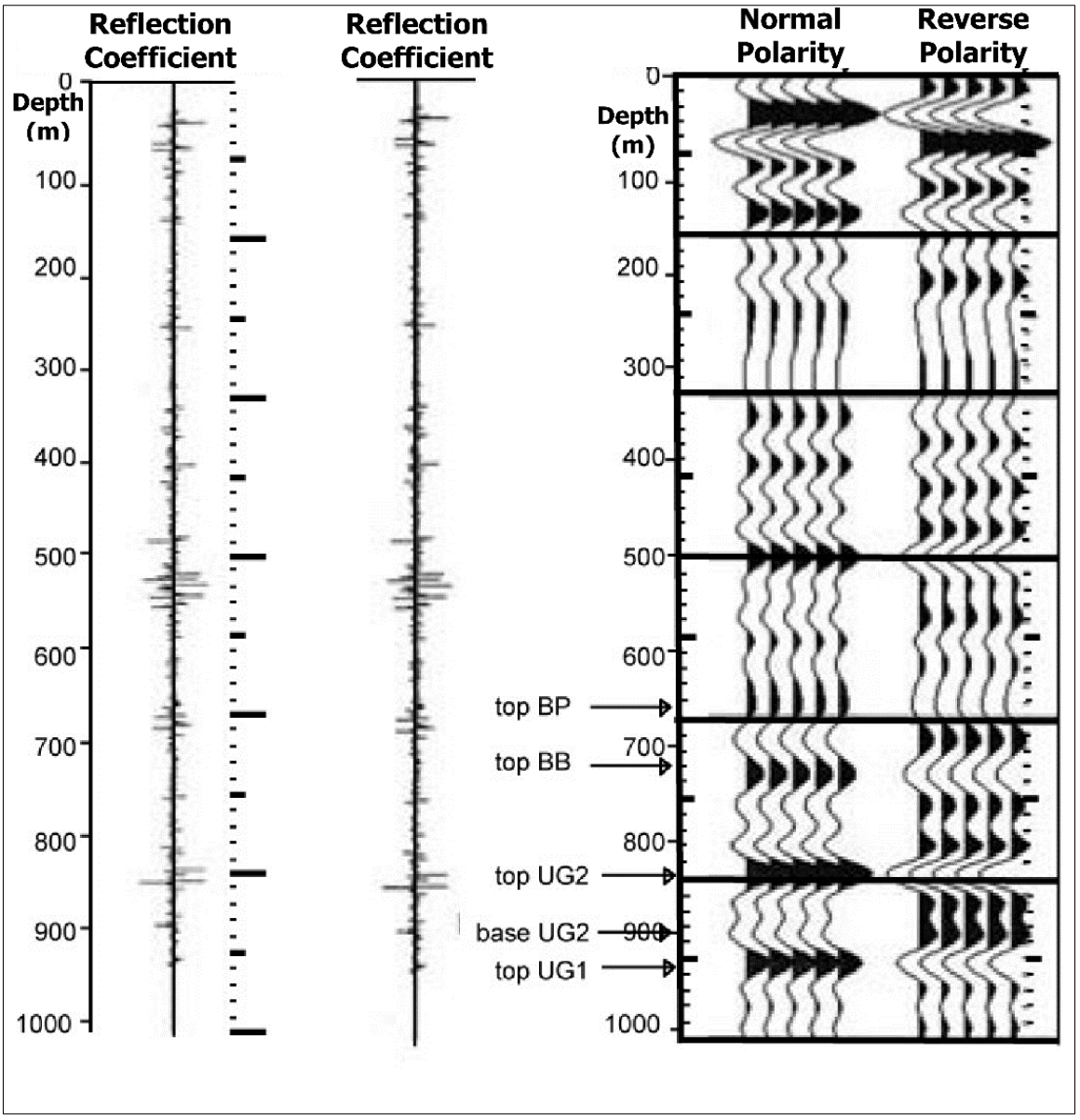

Figure 4.2: Synthetic seismogram showing the UG2 pyroxenite as a major seismic reflection event. Seismic velocities (~ 6500 – greater than 7000 m/s) and density (~ 2.8 – 3.28 g/cm^3) yielded reflection coefficient in the range 2 – 7% (modified from Campbell, 2011).

4.2. Borehole correlation

One hundred and ninety-nine boreholes were used to constrain the positions of different structures of interest seen throughout the data (Figure 4.3). Boreholes intersected various geological structures, some of which are:

- Iron-rich Ultramafic Pegmatoids (IRUPs)
- Merensky Reef
- UG2 Reef

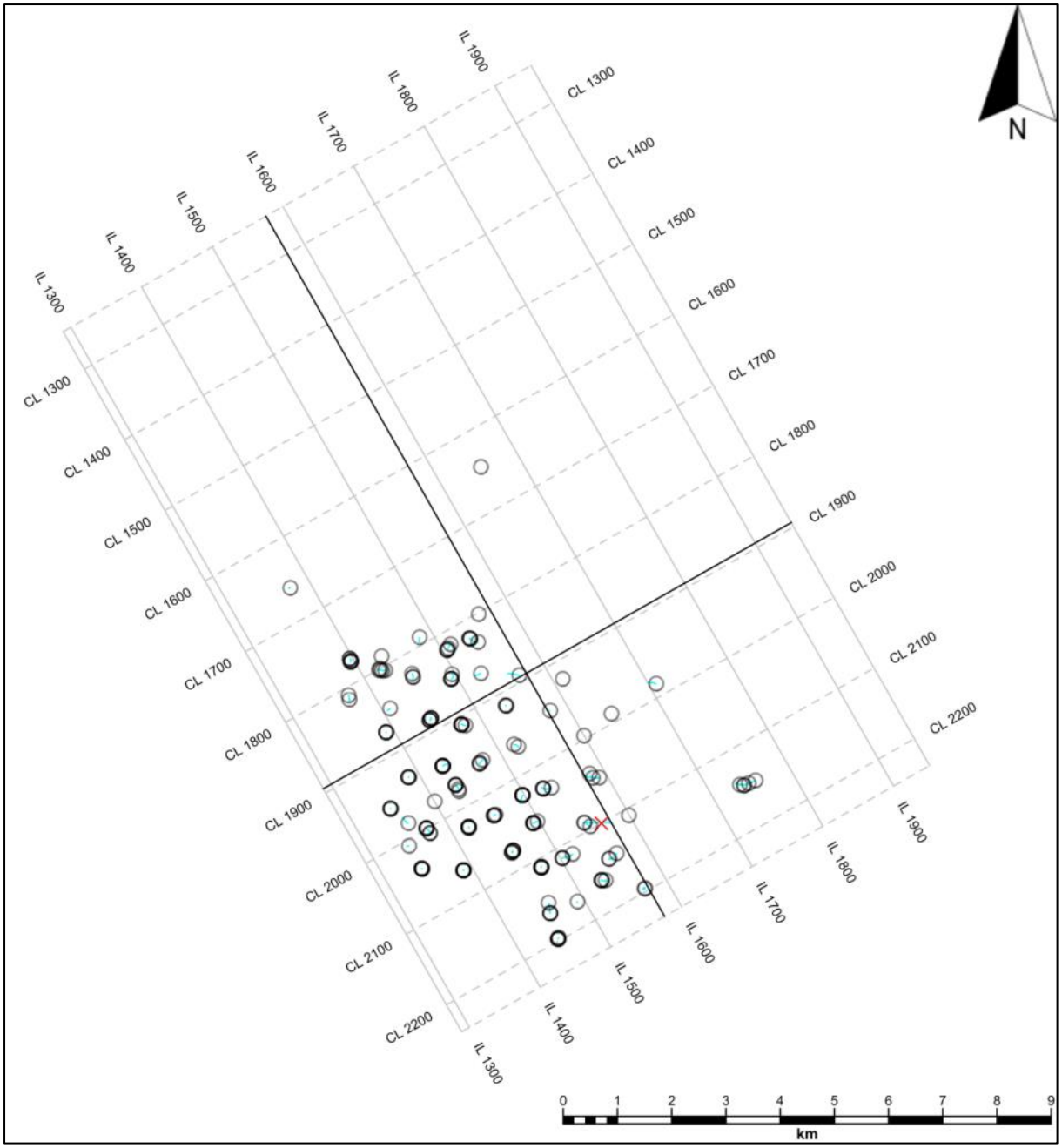

Figure 4.3: Survey area showing the location of the boreholes that were used for this study.

Horizon interpretation, as further discussed in the next section, was constrained using borehole correlation with the structures of interest. Unfortunately, the boreholes were only geologically logged and no downhole geophysical data was available for this study. The data would have further constrained the seismic data by providing a better understanding of the expected geophysical responses, such as reflection strength.

4.3. Horizon interpretation

The UG2 marker horizon was interpreted using both manual and 3D automatic picking interpretation techniques. Firstly, automatic picking of the horizon was carried out to perform first-pass examination of the data. This was done by placing seed points on confirmed areas of the marker horizon, using borehole logs, and then letting the automatic picking algorithm map out the horizon throughout the data. In areas of low signal-to-noise ratios and areas of structural complexities, such as on the edges of the survey area that have a poor fold coverage and areas with potholes, the auto-picking algorithm yielded low quality results.

Secondly, manual picking was carried out initially on a 10 m x 10 m inline by crossline spacing and then on every inline and crossline. The position of the UG2 marker horizon was constrained using available borehole logs (Figure 4.4), and the reflector was then traced throughout the volume even in areas without borehole data (Figure 4.5).

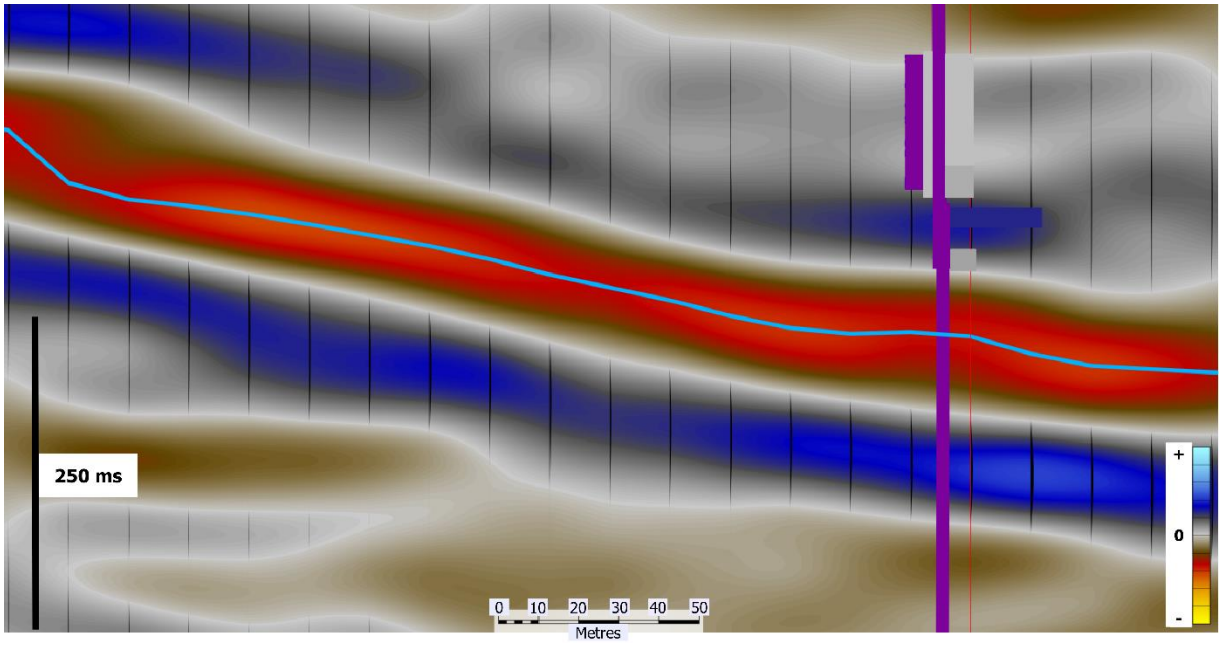

Figure 4.4: UG2 marker horizon picked with the aid of borehole log data.

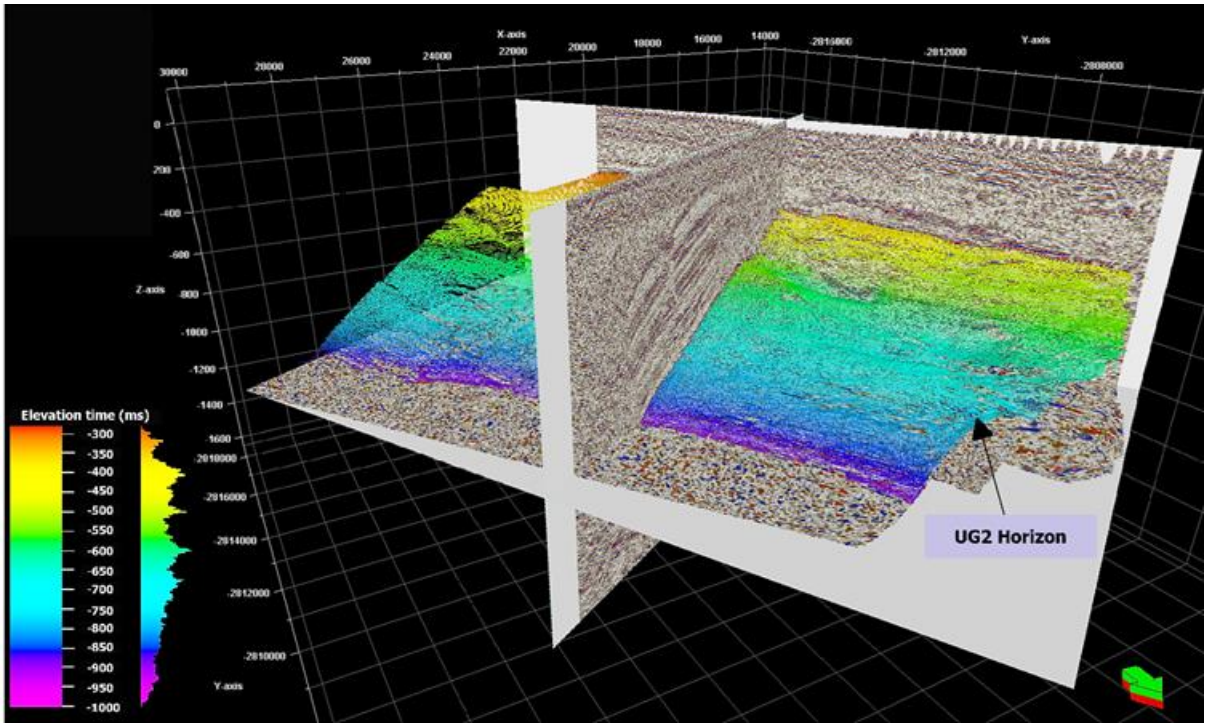

Figure 4.5: UG2 marker horizon picked throughout the entire 3D volume.

4.4. Seismic trace attribute analysis

Following the picking of the horizon of interest, it was noted that there was some more detail within the data that could be enhanced and extracted beyond what could be seen through conventional picking. Initial fault analysis was also carried out on the amplitude data, but due to the noisy nature of the data, detailed fault analysis was left to be done later after applying seismic attributes.

4.4.1. Data conditioning

Before horizon attributes could be applied to the picked horizon, it was first gridded and smoothed using Petrel's convergent interpolation algorithm (Figure 4.6). Convergent interpolation is a fast, reiterative surface gridding and smoothing algorithm. It builds models in stages by iterating or converging from an initial to a final solution, while also improving resolution of the data. It retains general trends in areas with little data while detail is honoured in areas where detail already exists.

Data conditioning creates a single gridded surface when building a structural model. It is the core modeller for horizons and faults. It is a general-purpose algorithm suited to various densities and a variety of data types. Some of which are: 2D seismic, 3D seismic, contour

data and well markers. The algorithm can handle sparse point data (horizon marker interpretations), line-type data (e.g. fault interpretations), dense point data (horizon interpretation grids) or combinations of these and other data types.

Convergent interpolation is broken into three separate, sequential steps, (the resultant surface derivatives of each iteration are interpolated and fed into the next iteration):

- Refine - Change grid resolution.
- Snap - Grid (or re-grid) the data.
- Smooth - Minimize grid curvature using a constrained, biharmonic operator.

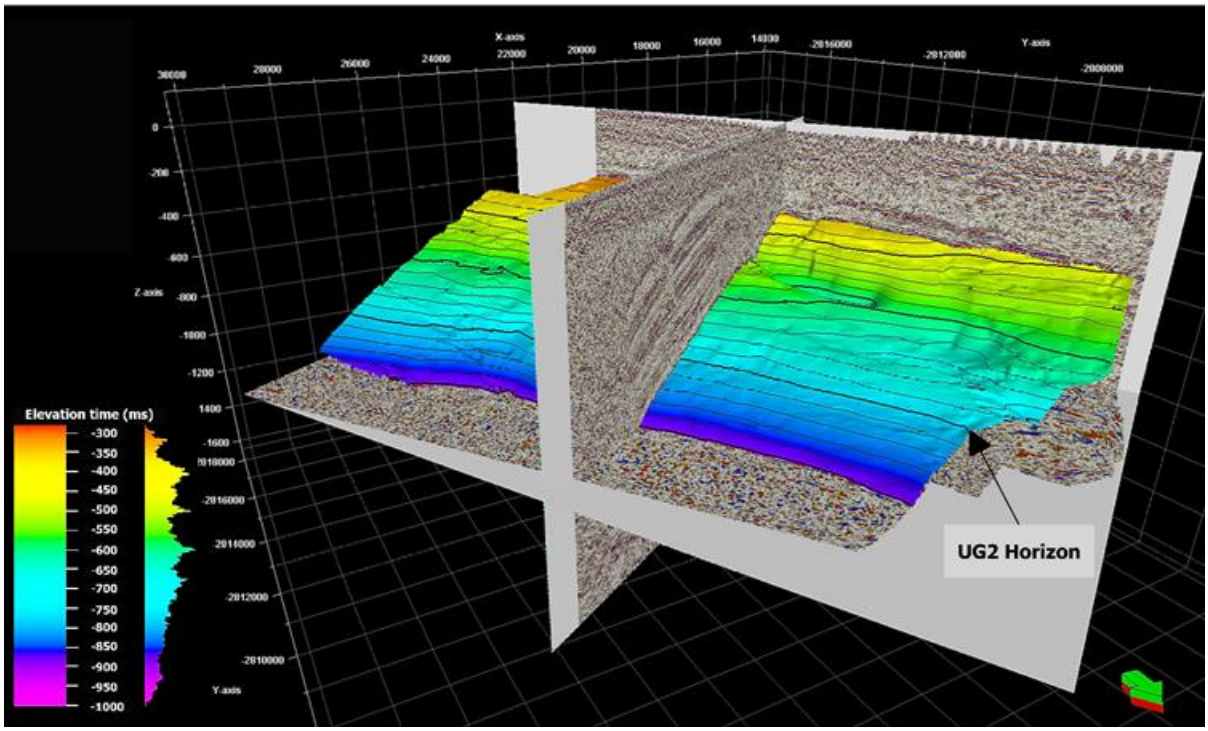

Figure 4.6: The UG2 marker horizon, in 3D view after gridding and smoothing.

4.4.2. Horizon seismic attributes and operations

Making correct fault interpretation is a crucial step for understanding fault development in a region, as this has impact on safety and optimum mine planning. As previously mentioned, the application of attributes is to improve confidence in structural delineation and the reliability of the data interpretation. After gridding and smoothing the horizon, as shown in Figure 4.7, the following horizon attributes were applied: **surface stability index, dip angle,**

dip-azimuth and edge detection. The results of the attribute analysis are discussed in Chapter 5.

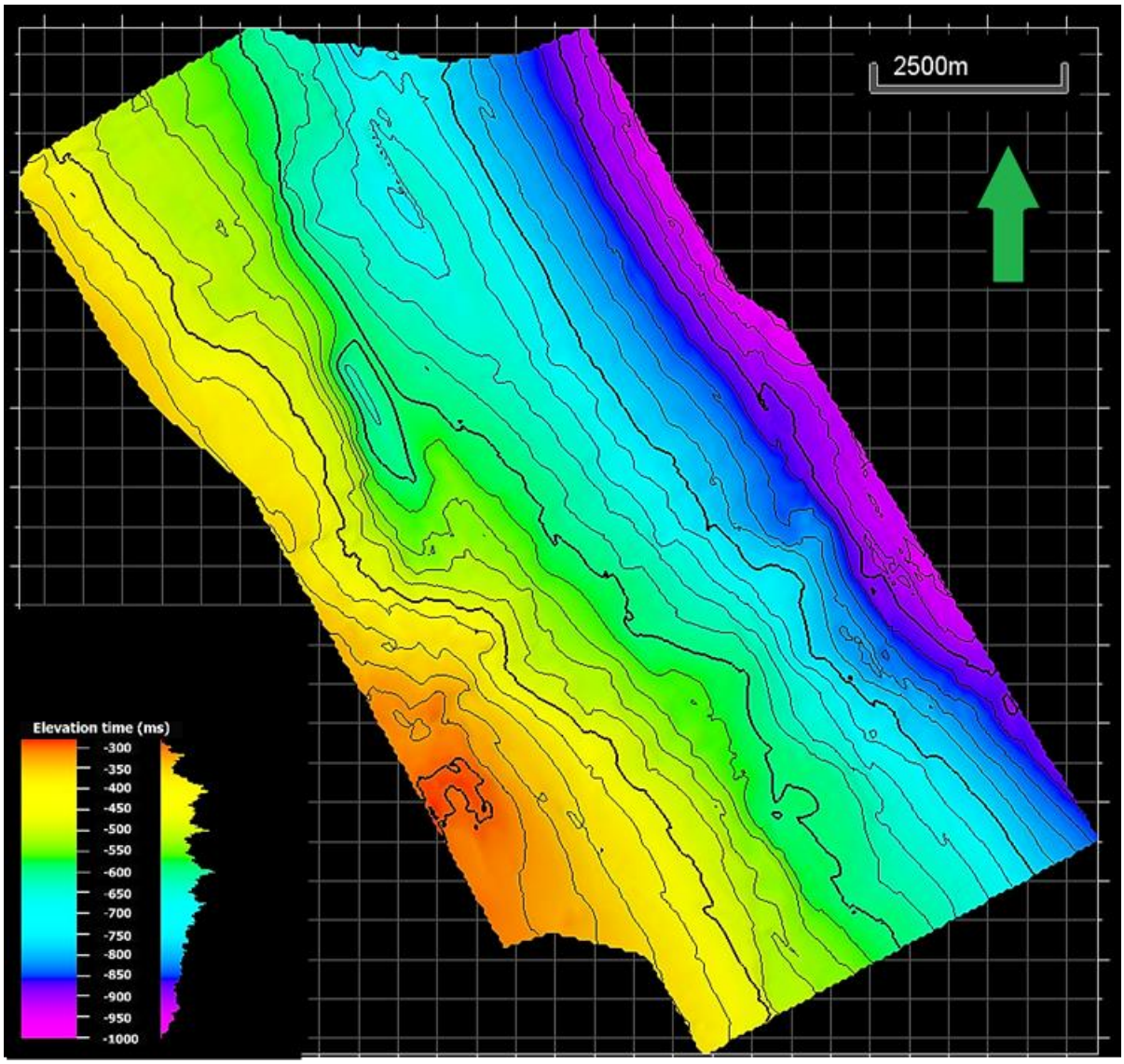

Figure 4.7: The UG2 marker horizon, in map view, with the colourbar showing the vertical time extent on the surface, from 300 ms to 1000 ms, with 50 ms contour interval.

4.4.3. Volumetric seismic attributes

The ant-tracking algorithm, widely used in fault interpretation, is highly dependent on the choice of processing methods and attributes combination within the workflow. As mentioned previously, the workflow stages are: **seismic conditioning, edge detection and edge enhancement**. I experimented with different parameters to determine the optimum workflow for my data and region.

4.4.3.1. Seismic conditioning

Dominant frequency

As mentioned earlier, the dominant frequency attribute characterizes the time-varying spectral properties of the seismic data. By applying this attribute, an interpreter can understand the frequency bandwidth of the data and can then feed that as a parameter to the graphic equalizer attribute. Figure 4.8 shows the same crossline views of the data. The data are characterized by frequencies between 0 Hz and 180 Hz.

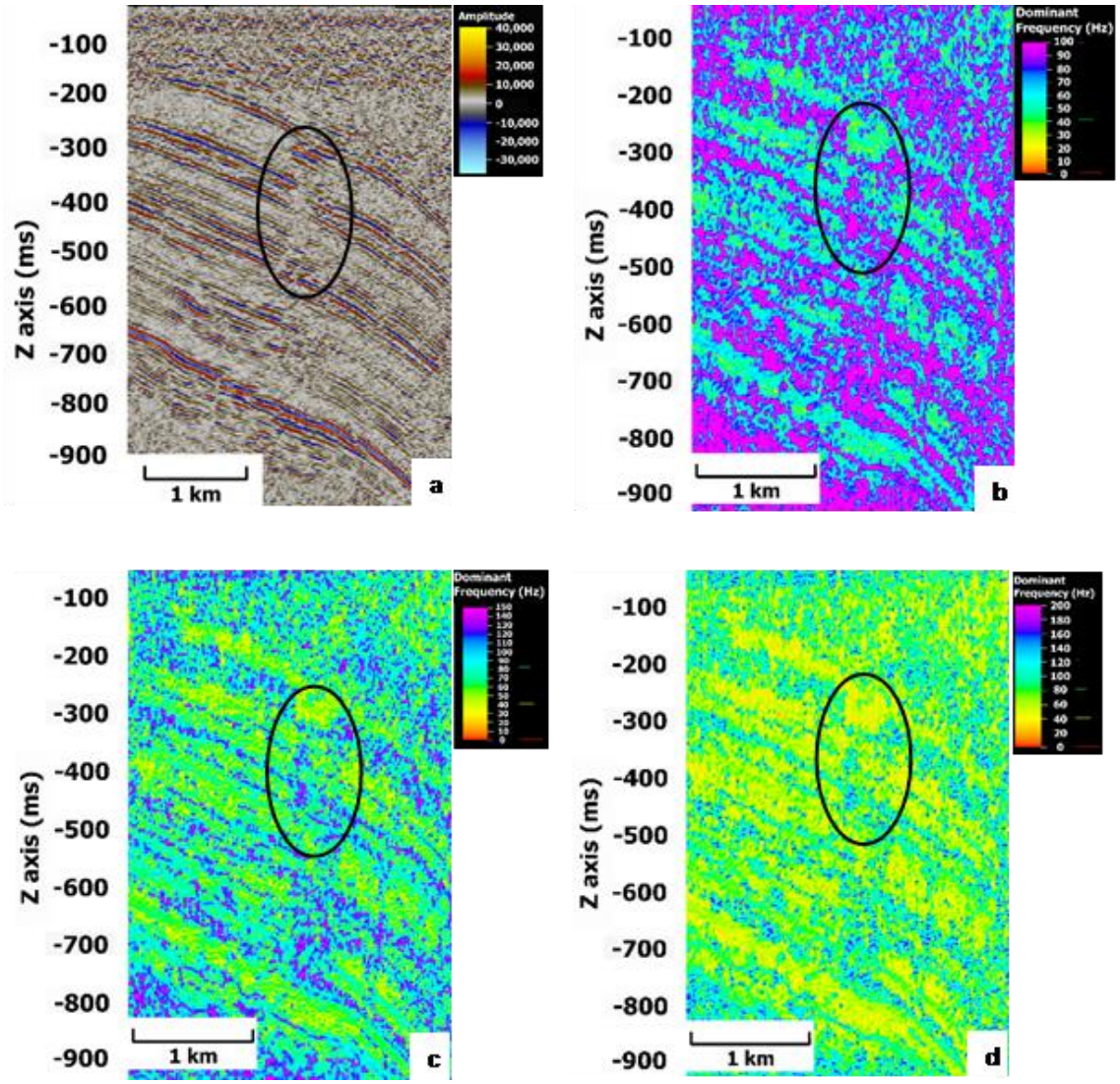

Figure 4.8: (a) Normal amplitude display, then with dominant frequency applied and capped at (b) 100 Hz, (c) 150 Hz and (d) 200 Hz. Black circles highlighting an area in the data showing disruptions in the dipping horizons, clearly imaged in (a) and better resolved in (b), (c) and (d), while also giving the frequency distribution.

Structural smoothing vs Graphic equalizer

The structural smoothing attribute was computed in various settings and was compared to the graphic equalizer attribute. Structural smoothing was run in “plain”, “dip-guided” and “dip-guided with edge enhancement” settings using filter sizes of: 1.0, 1.5 and 2.5 (Figure 4.9) below. The filter size controls the number of traces (horizontally) and samples (vertically) used for estimating structural smoothing. The value represents the standard deviation for the Gaussian filter.

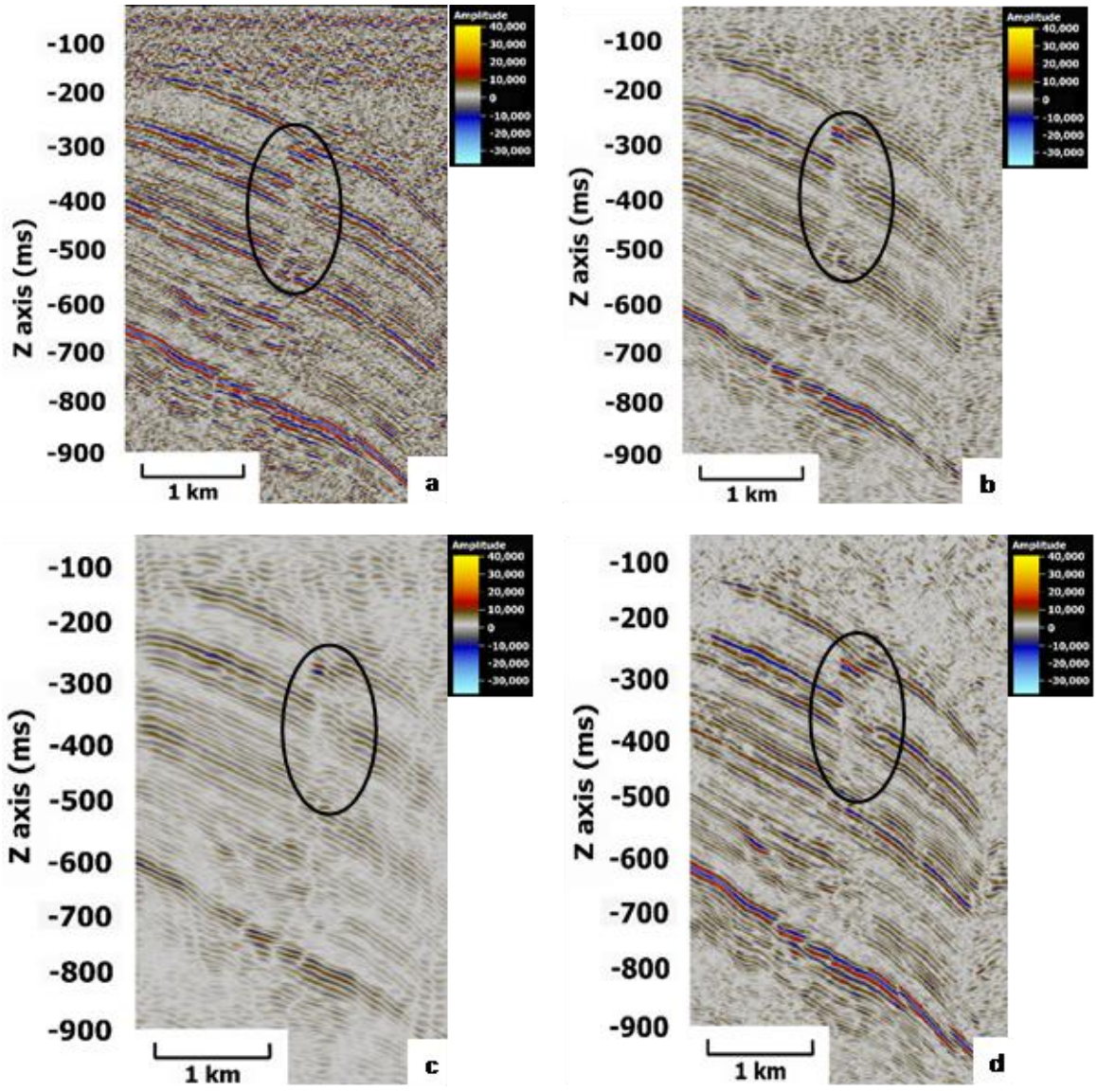

Figure 4.9: (a) Normal amplitude display, then with structural smoothing filter size of (b) 1.5 plain, (c) 2.5 plain and (d) 1.5 dip guided with edge enhancement. Black circles are highlighting an area of reef disruption being resolved with smoothing. (d) retains features better than the original amplitude display.

The graphic equalizer attribute was run with the frequency range of 0 Hz – 180 Hz, obtained from the dominant frequency attribute, and a range between 30 Hz and 90 Hz seemed to contain most of the data (Figure 4.10). Eventually structural smoothing – dip guided with edge enhancement with a window size of 1.5 was compared with graphic equalizer attribute with the boosted bandwidth range of 30 Hz – 90 Hz.

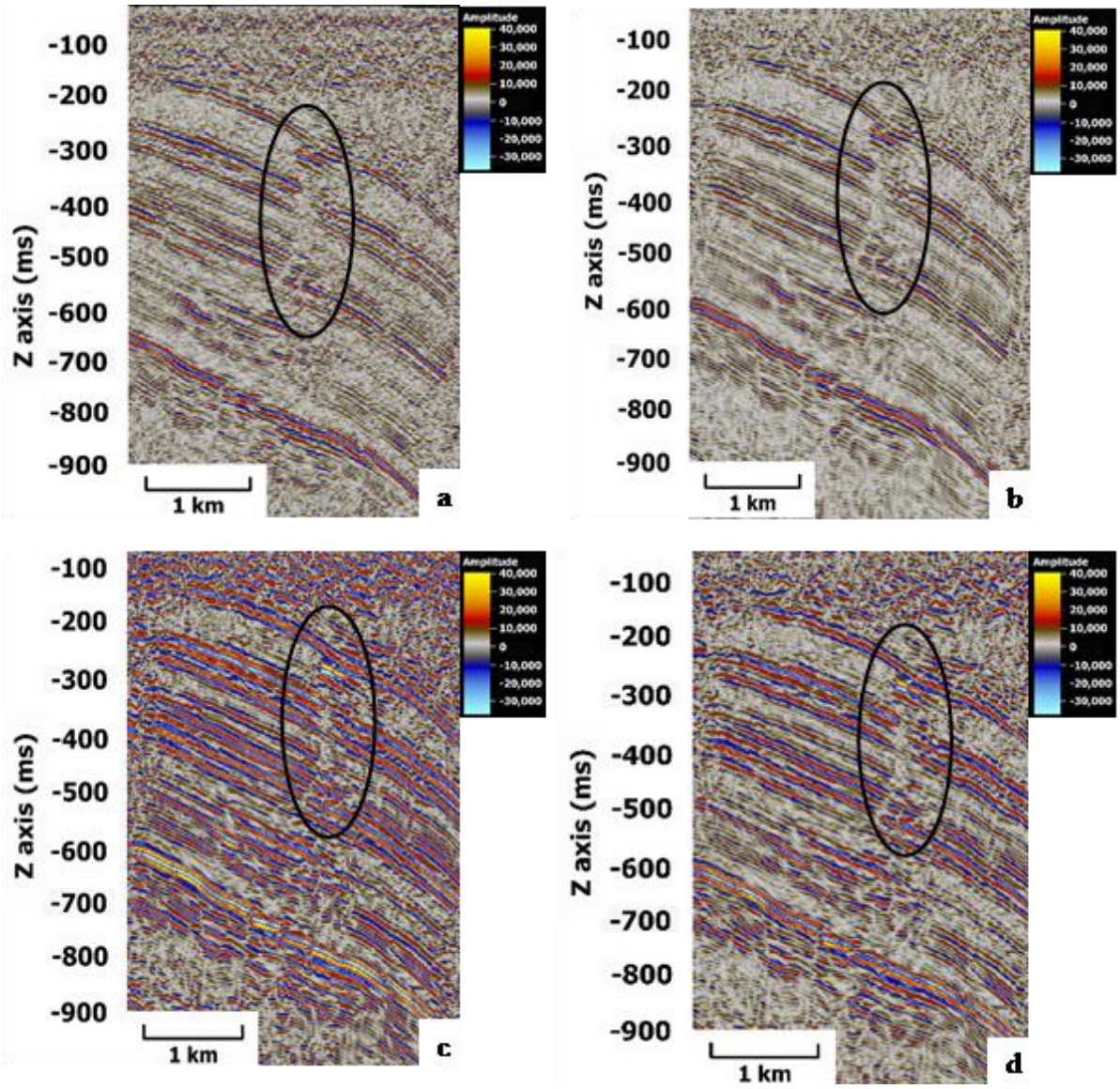

Figure 4.10: (a) Normal amplitude display, then: graphic equalizer with frequency filter set to 30 – 90 Hz with: (b) no enhancement, (c) 2-fold enhancement and (d) 1.5-fold enhancement. Enhancement (d) best preserves vertical and enhances lateral continuity, while significantly reducing noise in the data.

4.4.3.2. Edge detection

Variance vs Chaos

Many iterations were run, in different modes, for the variance attribute and compared with the chaos attribute. These attributes were applied to both the Structural Smoothened preconditioned and Graphic Equalizer filtered volumes (Figures 4.11 and 4.12). The iterations involved altering the inline, crossline ranges of 3 and 5, respectively; while the vertical smoothing parameter was toggled between 8 and 15, with the dip correction toggled on and off.

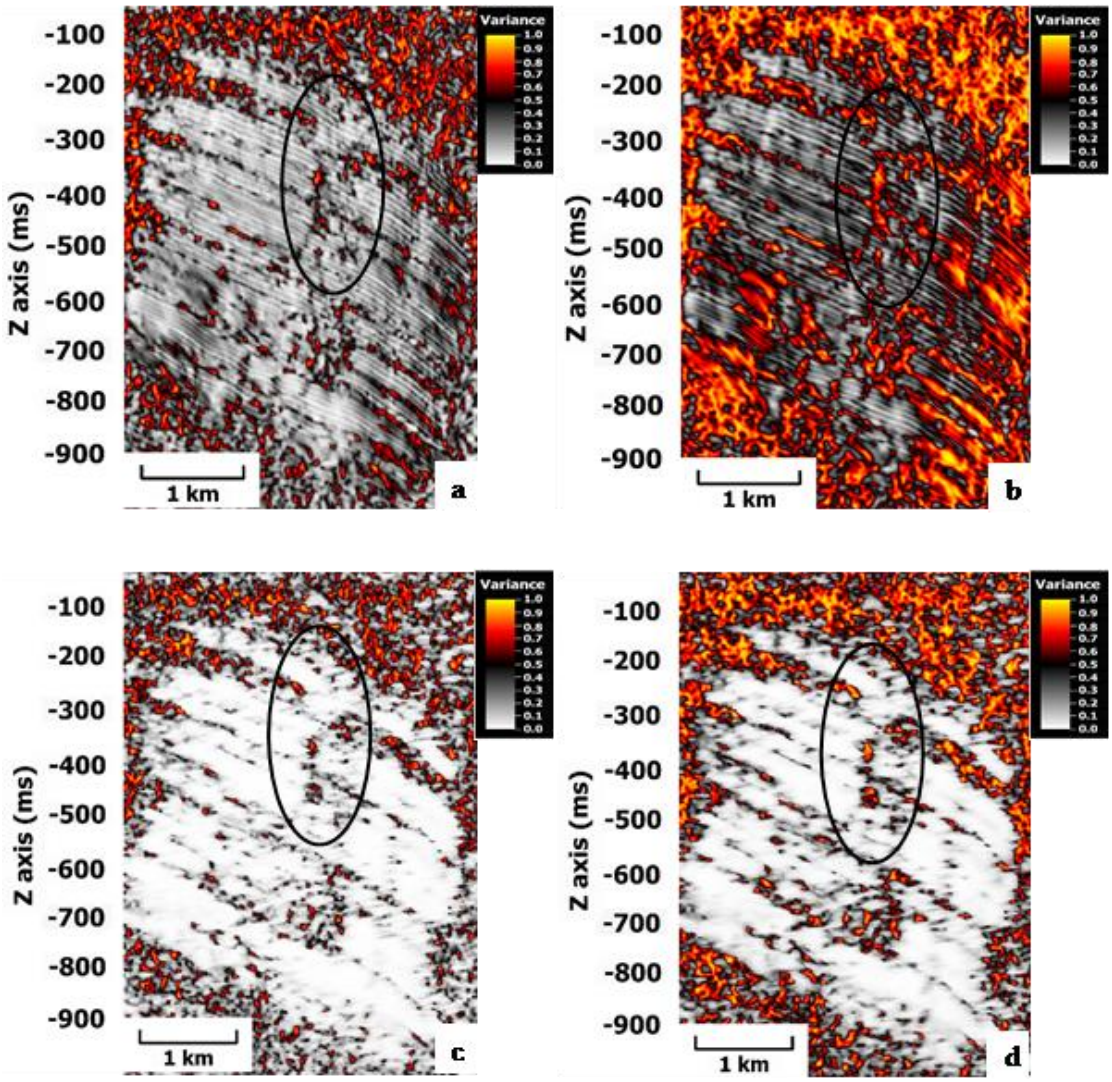

Figure 4.11: Variance (a) 3 x 3 and (b) 5 x 5 without dip correction and (c) 3 x 3 and (d) 5 x 5 with dip correction applied, from structural smoothing dip guided with edge enhancement. Better structural detail in (a) and (b), while (c) and (d) are relatively less noisy in comparison (black circles).

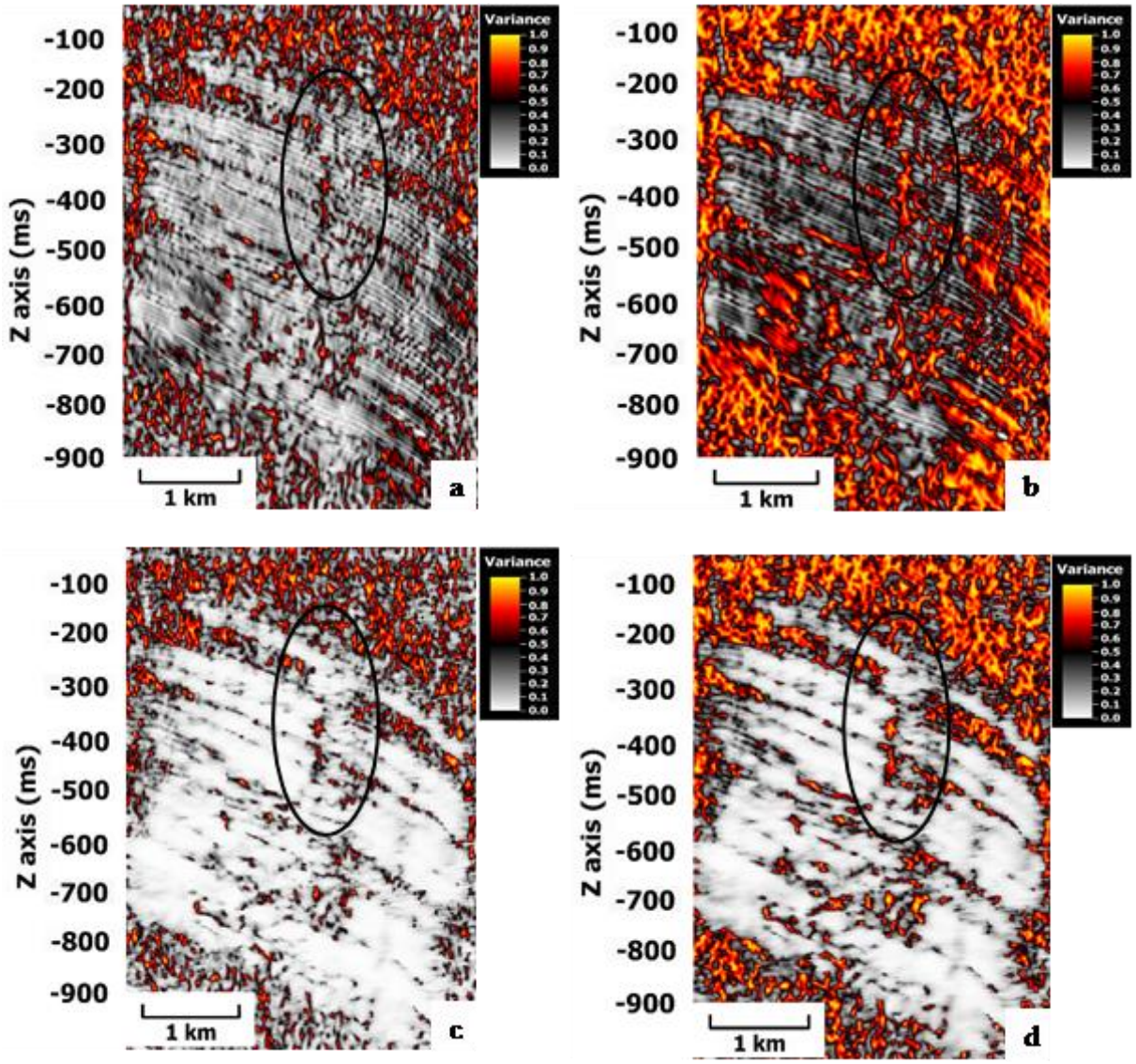

Figure 4.12: Variance (a) 3 x 3 and (b) 5 x 5 without dip correction and (c) 3 x 3 and (d) 5 x 5 with dip correction applied from graphic equalizer 30 Hz – 90 Hz. Better structural detail in (a) and (b), while (c) and (d) are relatively less noisy in comparison.

The chaos attribute was run with filter sizes of 0.5, 1, 1.5 and 2.0 for the x-, y- and z-directions, respectively and 0.7 was chosen because it yielded results with better structural detail. Figures 4.13 and 4.14 show outputs from structural smoothened data and graphic equalizer filtered data from the chaos attribute.

What can be seen in both the variance and chaos attribute outputs is the smearing effect in the data with the increase in filter window size. Care was taken in choosing the proper window size to honour features seen in the data.

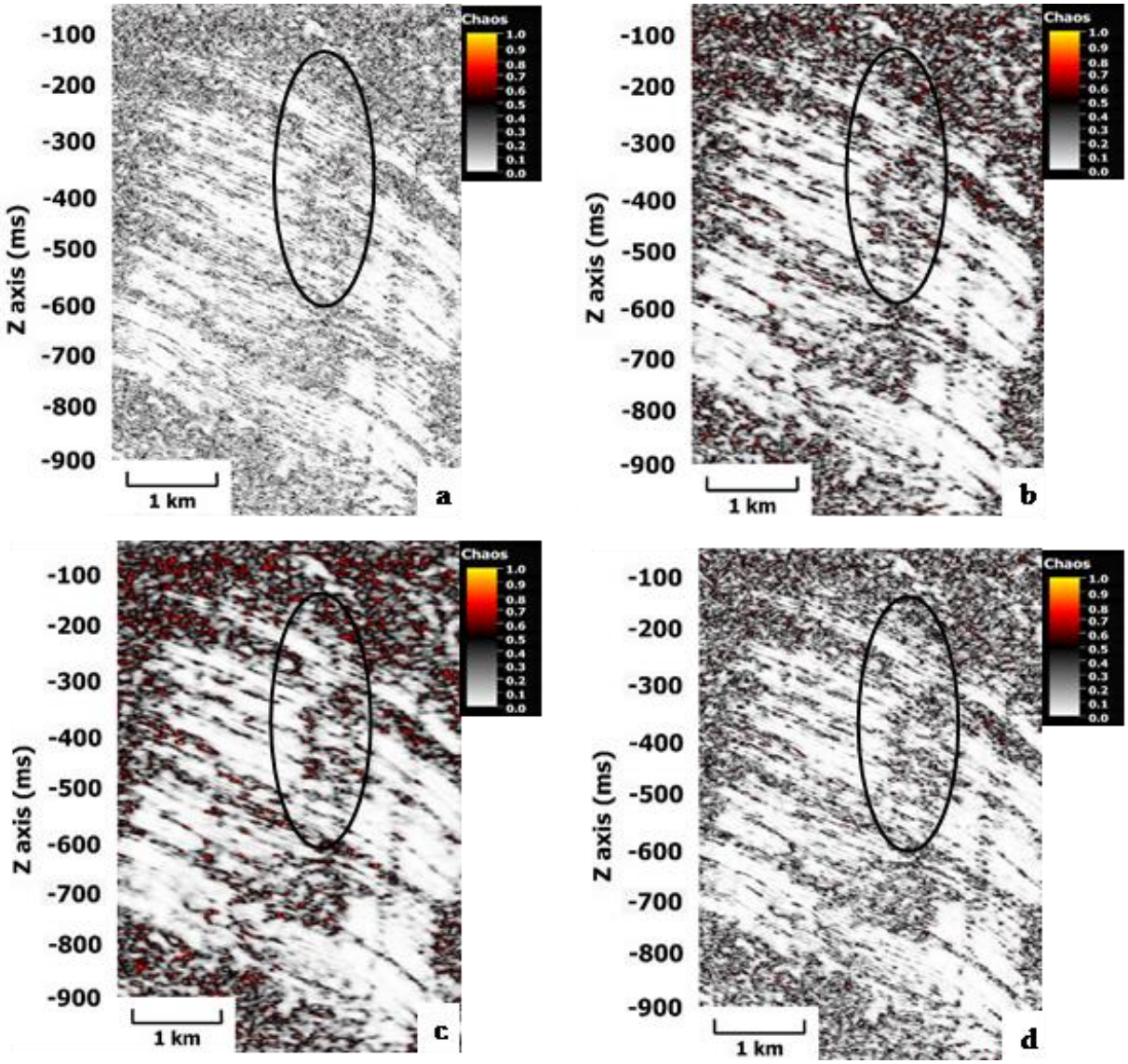

Figure 4.13: Chaos attribute (a) 0.5, (b) 1.0, (c) 1.5 and (d) 0.7 from structural smoothing 1.5 dip guided with edge enhancement respectively. While (b) and (c) seem smeared, (d) enhances features in the data (black circles).

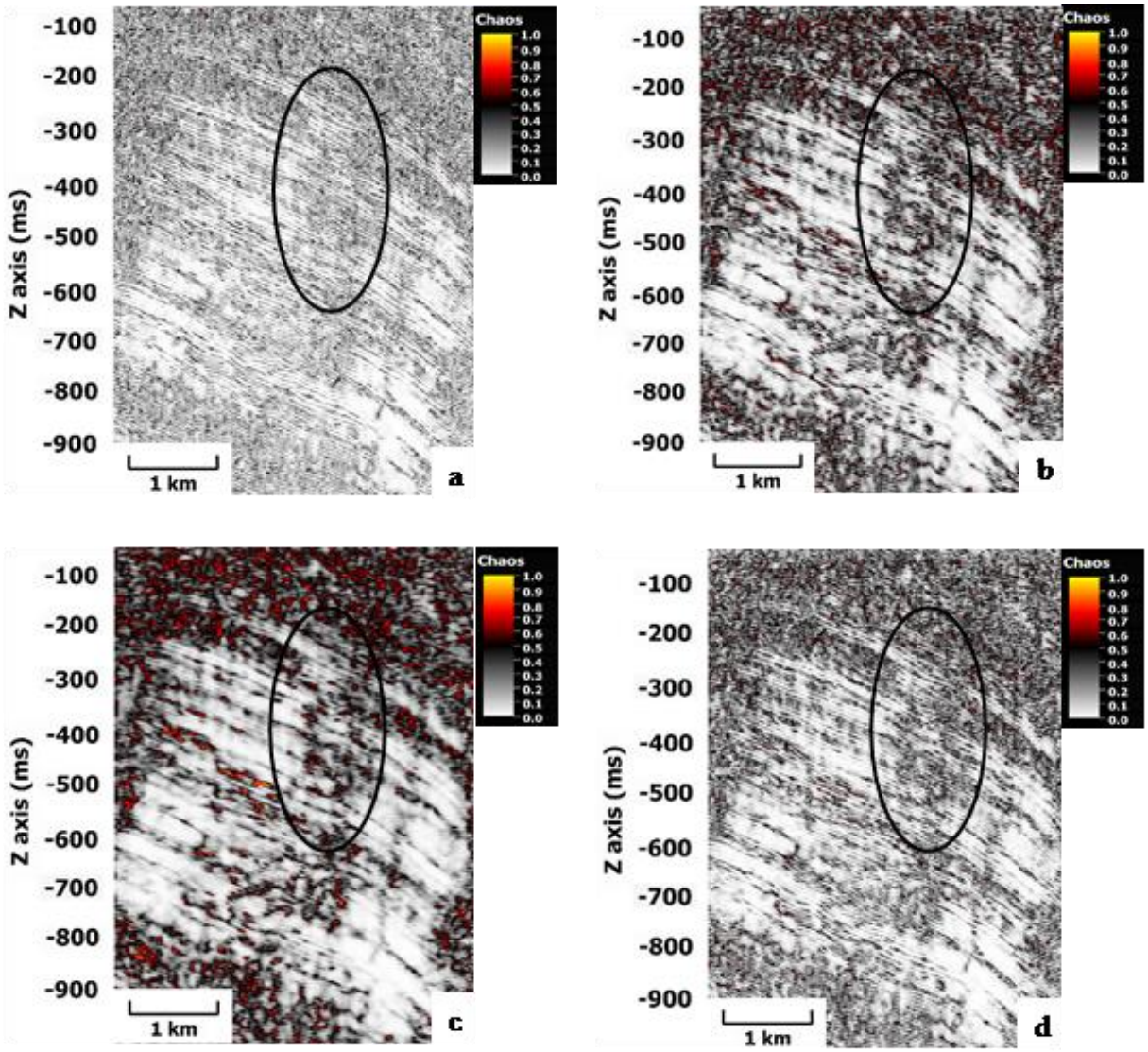

Figure 4.14: Chaos attribute (a) 0.5, (b) 1.0, (c) 1.5 and (d) 0.7 from graphic equalizer 30 Hz – 90 Hz. Filter sizes (b) and (c) yield smeared results while (a) and more in (d), we see more structural detail highlighted.

4.4.3.3. Edge enhancement

Ant-tracking

The ant-tracking attribute was run on the different edge detection resultant volumes (variance and chaos attribute volumes). When not coupled with other fault enhancing attributes such as variance and chaos, the ant-tracking attribute is inadequate. The ant-tracking attribute was initially run in passive mode, then aggressive mode and finally a custom mode, described in the Figure 4.15.

For each of the aforementioned modes, the following input volumes were used, and results compared:

- Smoothened – Variance
- Smoothened – Variance with dip correction ON
- Smoothened – Chaos
- Graphic Equalizer – Variance
- Graphic Equalizer – Variance with dip correction ON
- Graphic Equalizer – Chaos

It was noted that different input volumes used for the ant-tracking attribute yielded different results. An analysis of these is done in Chapter 5.

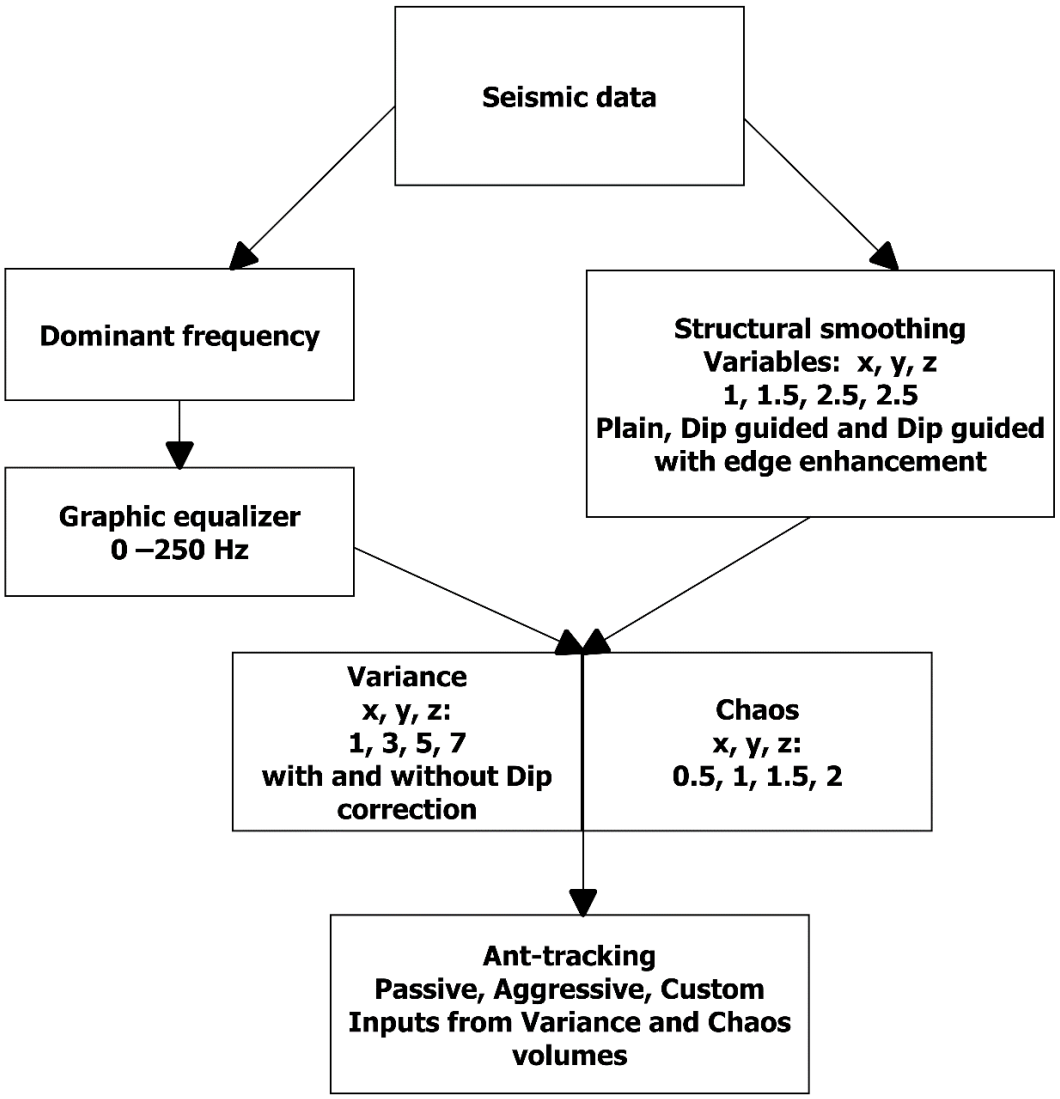

Figure 4.15: The ant-tracking workflow used for this study.

5. Results

This chapter presents results obtained from using different processing workflows, and contrasts interpretations that can be made in conventional seismic interpretations and those possible with the aid of seismic attributes.

5.1. Conventional interpretation

The crossline view of the 3D reflection seismic data (Figure 5.1) and time structure map (Figure 5.2) gridded UG2 horizon were produced from conventional interpretations. It is worth noting that not much structural information, e.g. faults, depressions, etc., can be derived from the map besides minor changes in the contours in time. Therefore, detailed structural interpretation cannot be drawn from the conventional time structure map due to poor structural resolution.

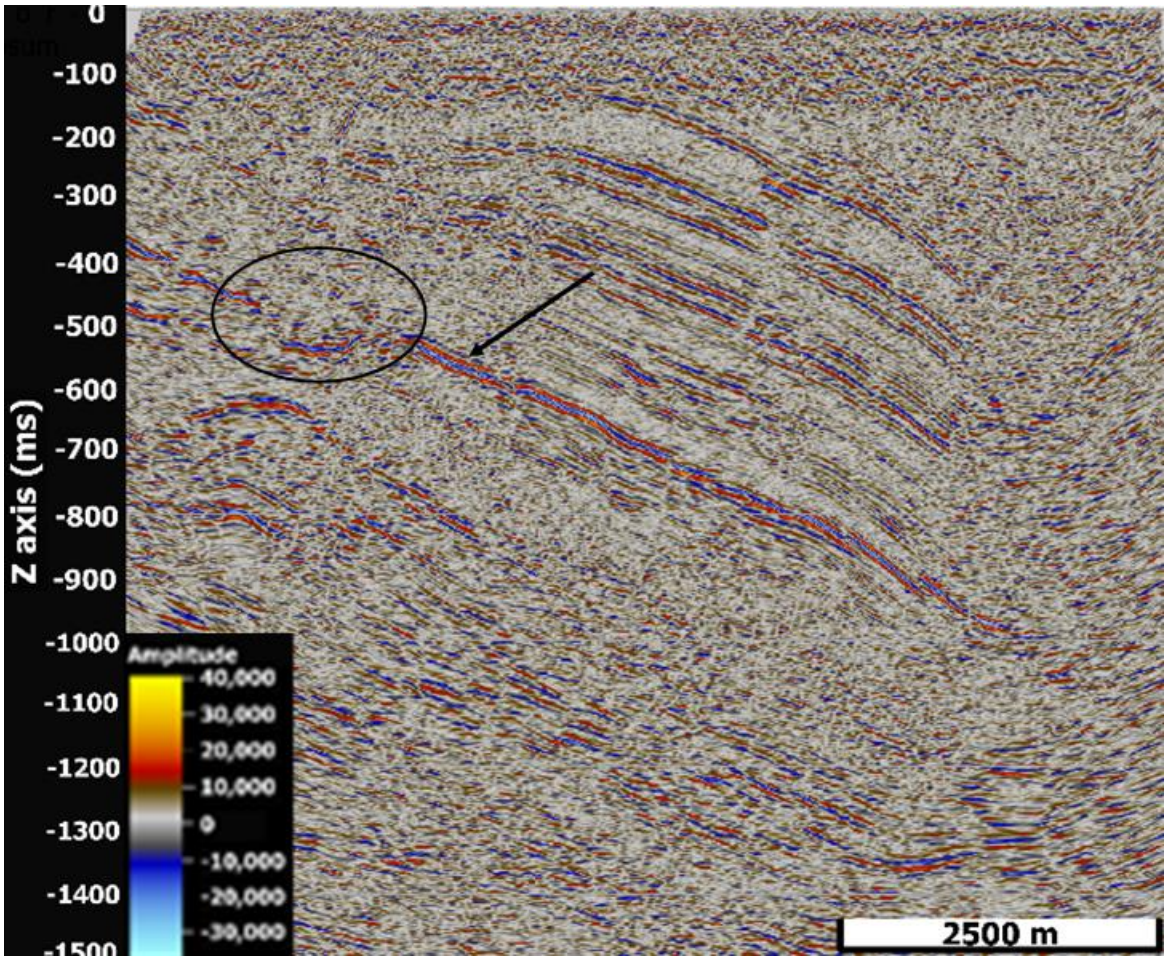

Figure 5.1: Crossline view of the 3D reflection seismic data, with the UG2 chromitite reef (pointed by black arrow) and possible pothole structure (circled).

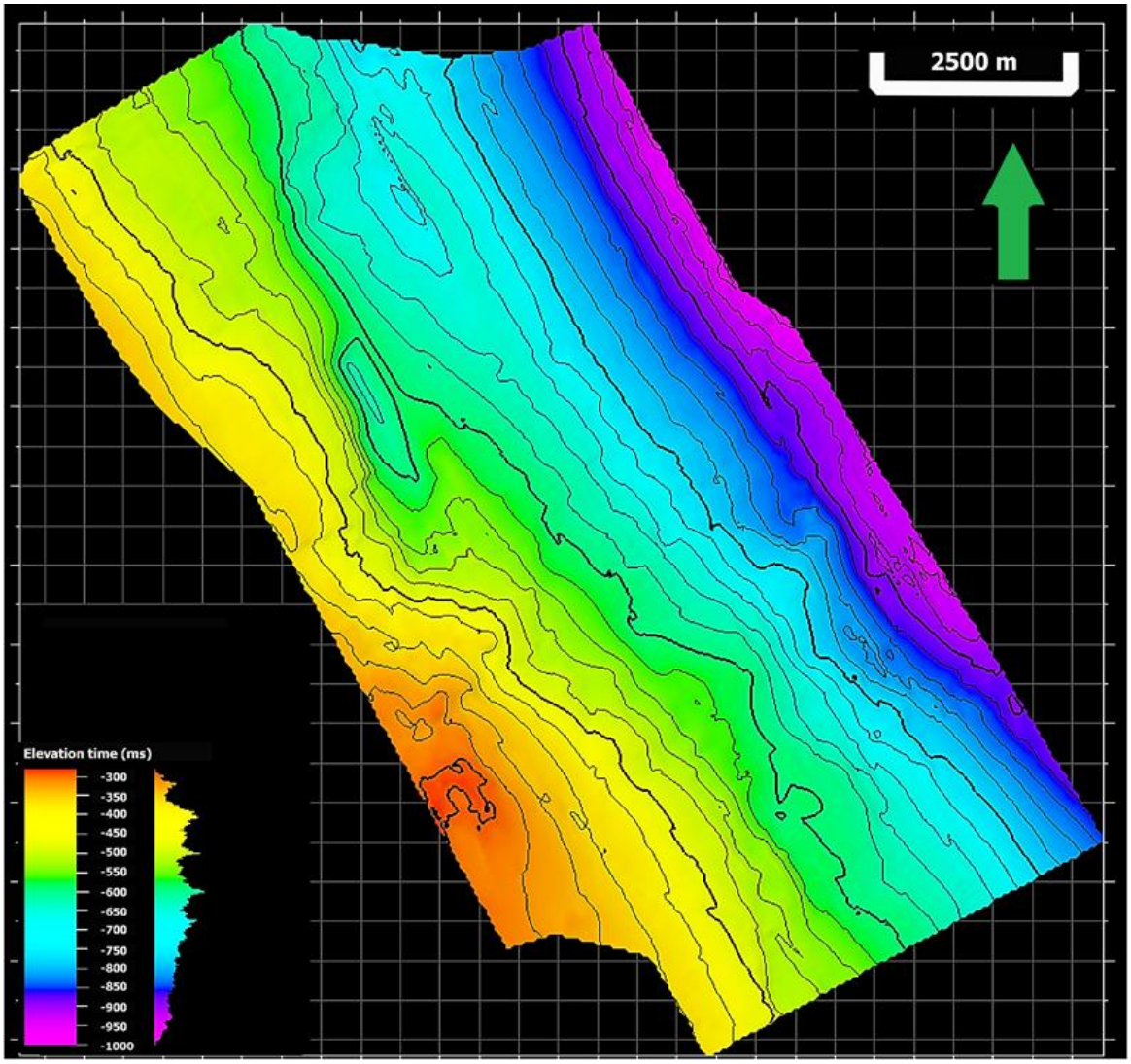

Figure 5.2: Time structural map, with contour interval set at 50 ms, showing the gridded UG2 horizon. It spans from 300 ms to 1000 ms (with a mean velocity of ~ 6500 m/s in the area, this translates to ~ 975 m to 3250 m), dipping between 9º - 12º in the NE direction.

5.2. Seismic attributes

From the conventional interpretation, several seismic attributes (dip angle and dip-azimuth, edge detection, surface stability and ant-tracking) were applied to reveal further subtle details that may have not been clear on conventional interpretation techniques. Prior to this, the picked horizon was conditioned to reduce noise and enhance signal-to-noise ratio as this will yield better seismic attribute results.

5.2.1. Horizon-based attributes

The dip angle applied on the UG2 horizon illuminates subtle dip characteristics of the surface that fall below the conventional seismic resolution limit (Figure 5.3). The features highlighted in the surface generally have a dip of 0º - 30º, but with the adjustment of the colourbar and cut off at 15º, we can highlight many subtle features of the surface dipping between 5º and 10º.

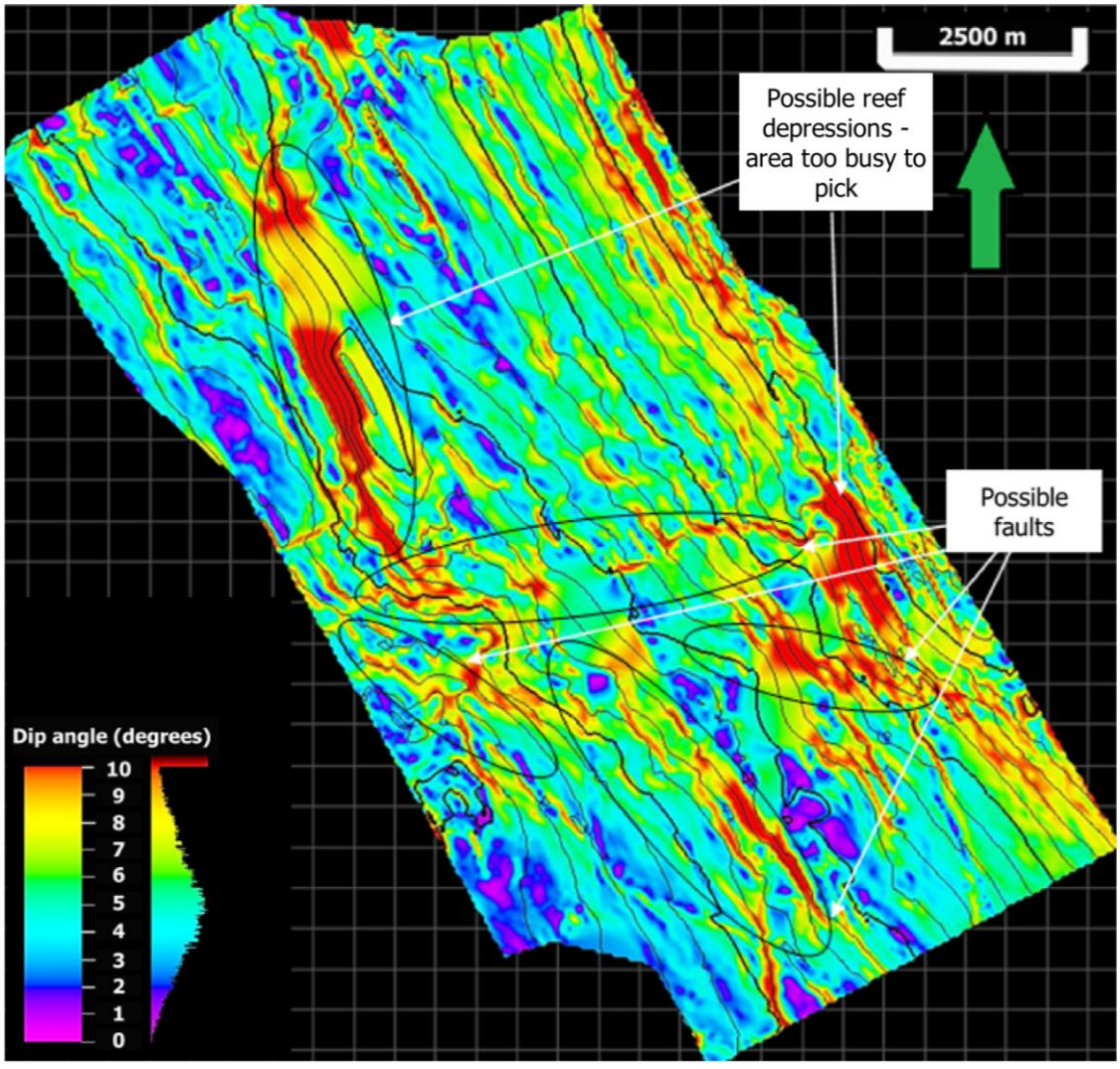

Figure 5.3: Dip angle map, with the colourbar restricted to 10º to better illuminate the subtle structures. Areas in red have dip angles greater than 10º and some are associated with linear structures.

Some structures with dip angles slightly outside this range are likely to be local geological structures, possibly faults or reef depressions; other cases are likely to be areas where the data are just too noisy to pick and interpret. The dip-azimuth attribute applied on the UG2 picked

horizon gives information about the general strike of the surface (Figure 5.4). The horizon has a general strike between 45º and 90º, with a few areas outside this range that are possibly local geological features, e.g. reef terracing. The dip azimuth highlights slightly more details of the surface, adding more linear structures where continuity is clearly visible due to their sharp contrasting azimuth to that of the overall horizon. The dip azimuth map shows some major scale lineaments throughout the surface that trend in the NW – SE direction, with highlight to some lineaments in the direction of dip.

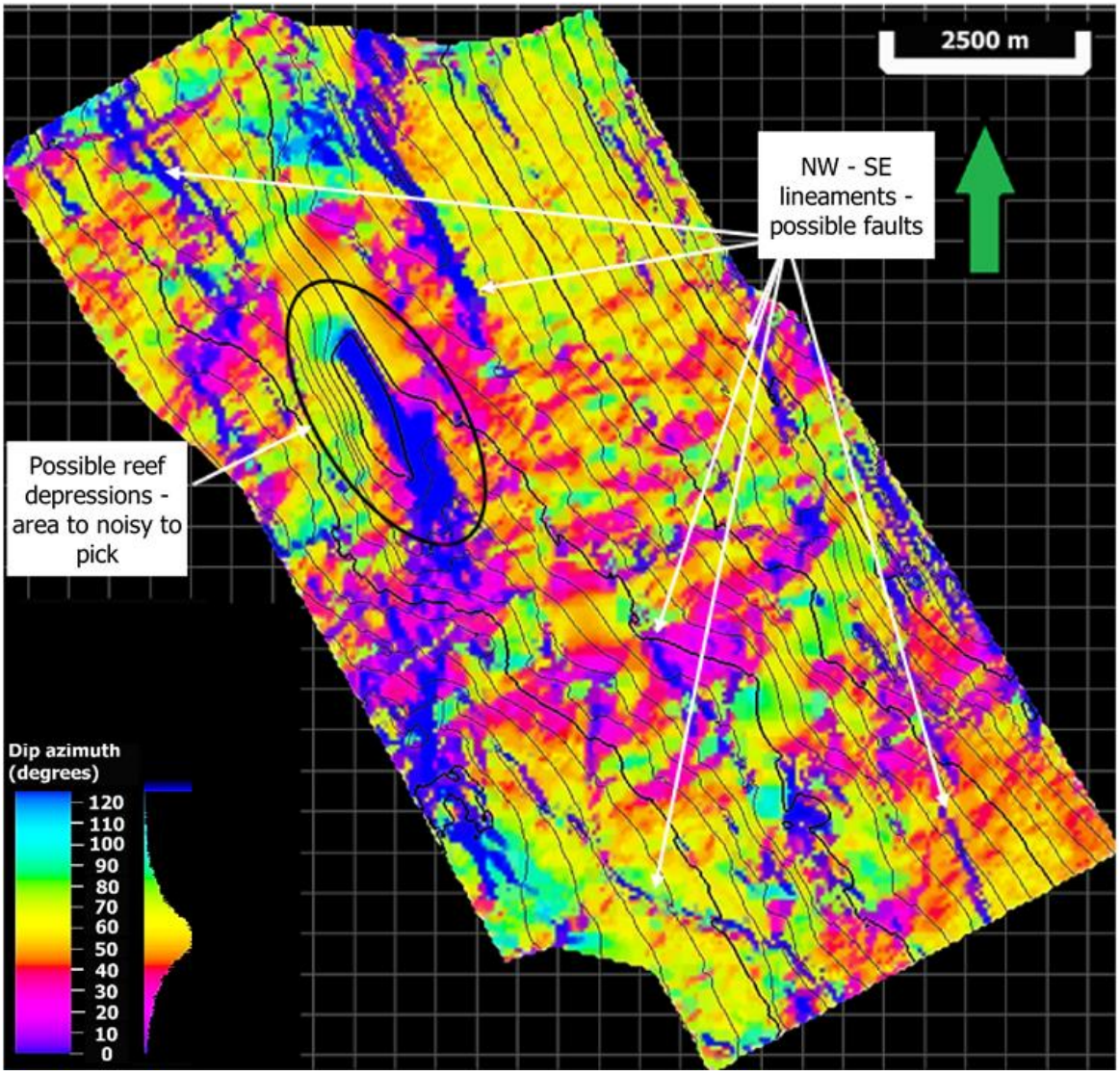

Figure 5.4 The dip-azimuth map, with the colourbar restricted to 125º, illuminating the general orientation of structures observed on the horizon.

The edge detection map, (Figure 5.5), illuminates and enhances the subtle features also seen from the dip angle and dip-azimuth maps. The map shows edge-like linear structures present

in some areas of the data like those delineated by the dip angle and dip-azimuth attribute maps. The edge detection attribute, however, adds more resolution on areas than the dip angle and azimuth attributes (Figures 5.3 and 5.4 respectively).

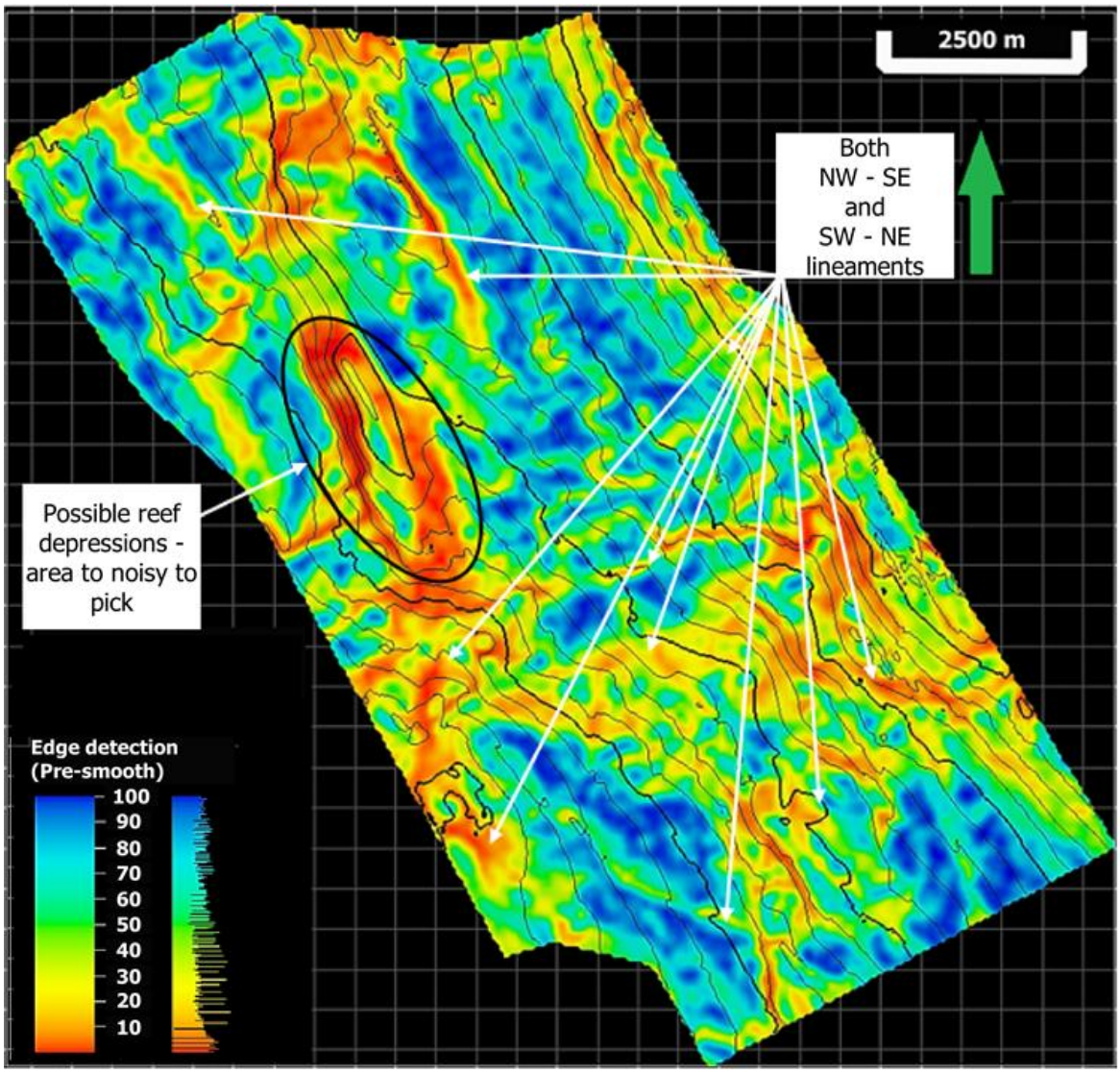

Figure 5.5: Edge detection map illuminating an array of lineaments that were below the seismic limit and were seismically 'invisible' to conventional seismic interpretations.

The surface stability map, shown in Figure 5.6, illuminates the pick confidence of the UG2 horizon, which is important information as it ties directly with the confidence of the results from other seismic attributes applied on the same surface (Figures 5.3, 5.4 and 5.5). Where confidence beyond 50% is exhibited in the attribute map, this relates to relatively good picks in that area and thus other different attribute information in these areas can be considered trustworthy.

Furthermore, areas with low signal to-noise ratio and possible linear features will be assigned a confidence index of below 50% due to the poor resolution resulting from vertical displacement of the reflector. As seen in Figure 5.6, areas assigned a low confidence index were also identified as possible geological features by the dip angle, dip-azimuth and edge detection attributes (Figures 5.3, 5.4 and 5.5).

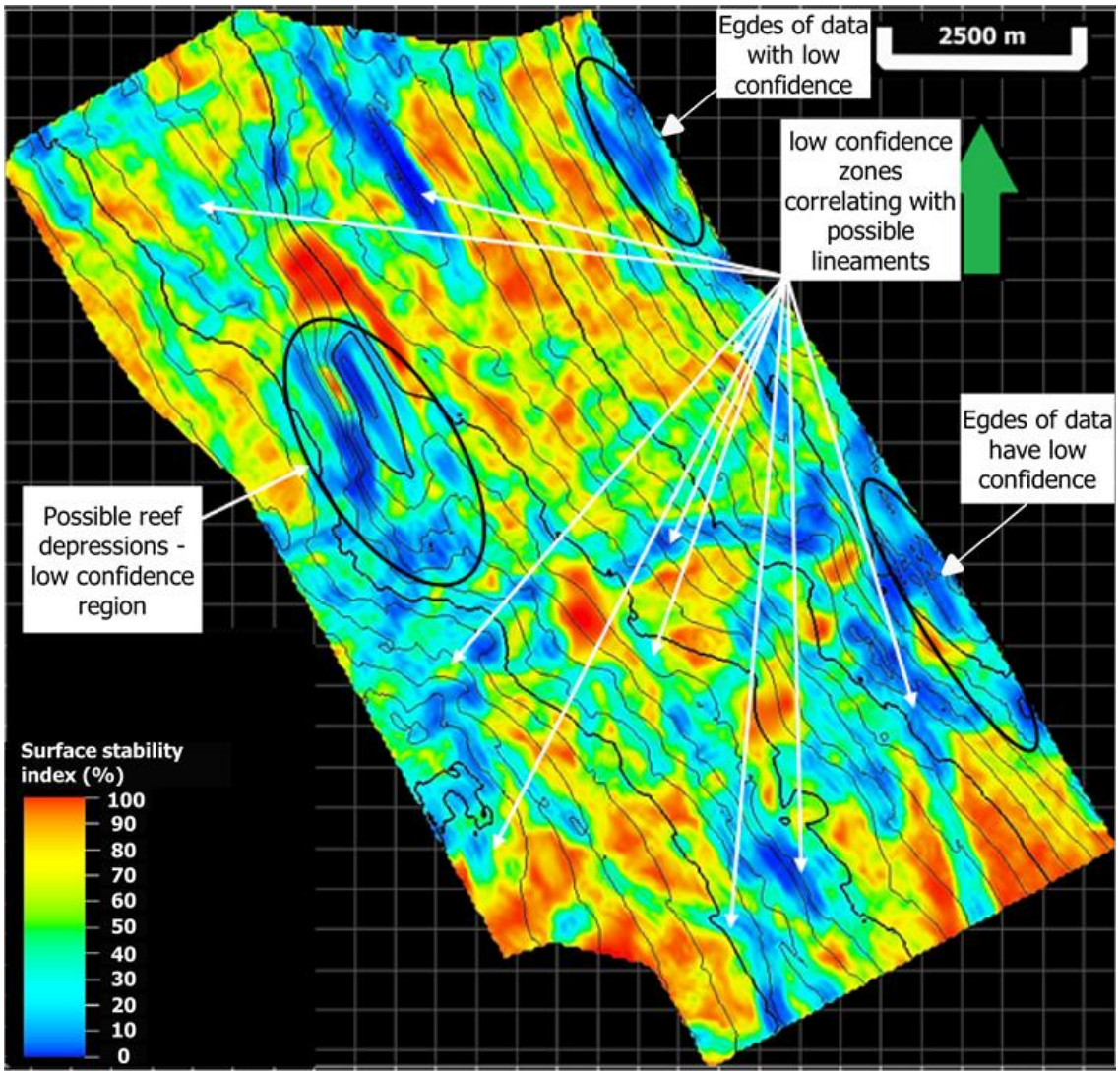

Figure 5.6: Surface stability map with the confidence index of the picked surface. Areas in orange and red have a higher confidence index than those in blue.

5.2.2. Volumetric seismic attributes

Prior to application of the volumetric attributes, the data were conditioned to enhance the signal-to-noise ratio and to reduce noise for better attribute results. Two different processing workflows were used for this study; one using structural smoothing to remove the noise, while the other approach was to use the graphic equalizer attribute, with the aid of the

dominant frequency attribute, to filter out the noise and enhance the desired frequency bands, as mentioned in Chapter 4.

The ant-tracking attribute maps were produced from the different edge detection outcomes of the two processing workflows. Figures 5.7 and 5.8 compare the results obtained from running the ant-tracking algorithm in passive mode from the structural smoothed and graphic equalizer filtered data respectively, specifically from the variance edge detection attribute.

The outcome from the structural smoothed data (Figure 5.7) has highlighted more structural detail than previously seen on the conventional seismic interpretation (Figure 5.1). Some of the gently dipping structures visible can be attributed to the layering also seen on the amplitude data. Some vertical and steeply-dipping structures that were not apparent on the amplitude data but are now visible, and can be attributed to joints, fractures or faults.

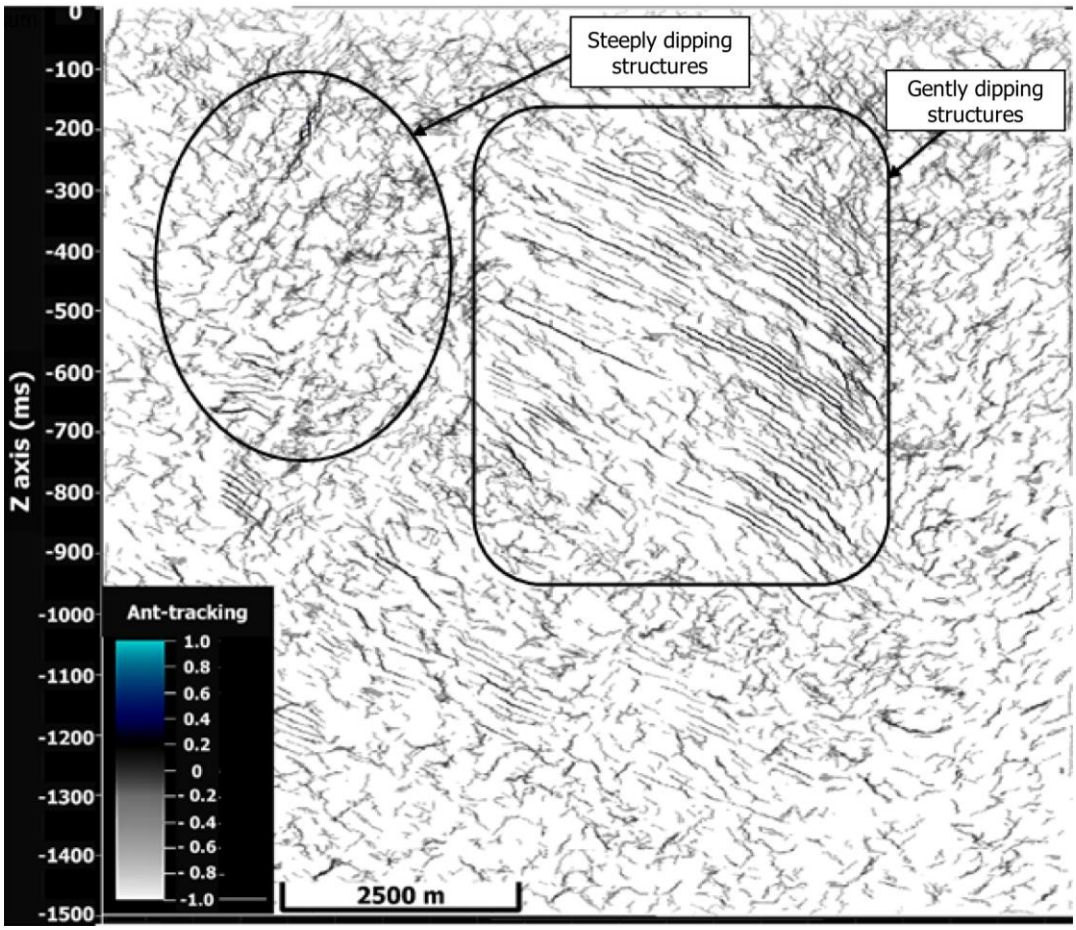

Figure 5.7: Crossline view of the ant-tracking results, run in passive mode, from the structurally – smoothed data with variance attribute applied. The visibility and continuity of

structures are considerably enhanced compared to the conventional amplitude display. Steep and gently dipping structures can be clearly seen, and their extents better resolved.

The outcome from the graphic equalizer filtered data (Figure 5.8) highlighted more structural detail than the ant-tracking outcome from the structural smoothed data. More near-vertical structures are highlighted than in the smoothed data outcome. However, some features observed in the graphic equalizer outputs are likely artifacts as there is no hint of these features in the raw images. Consequently, caution should be exercised throughout the processing workflow.

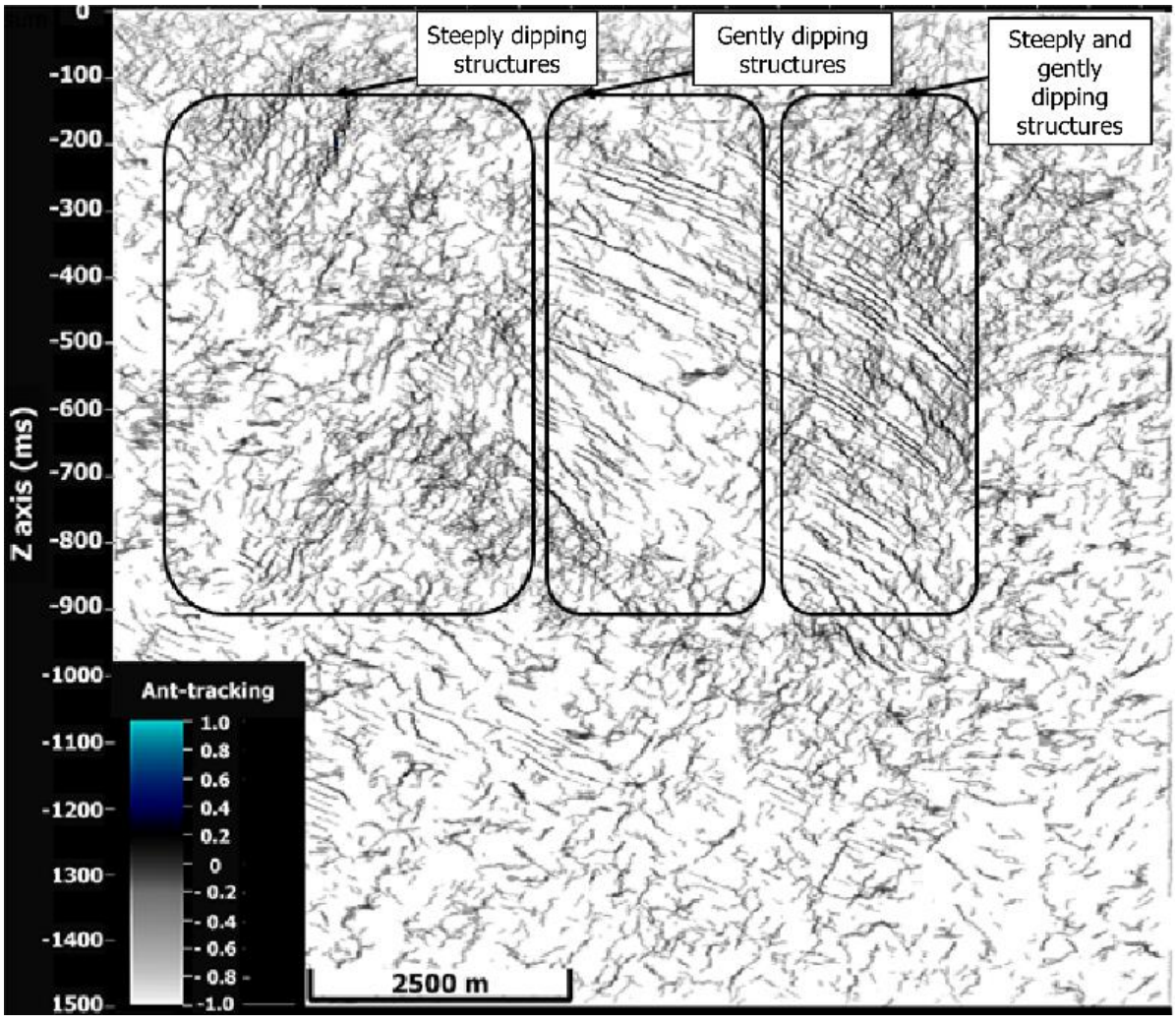

Figure 5.8: Crossline view of the ant-tracking results, in passive mode, from the graphic equalizer data with variance attribute applied. The visibility and continuity of structures are considerably enhanced compared to the conventional amplitude display. Areas of steep, gently and a combination of both steep and gently dipping structures can now be clearly seen, and their extents better resolved.

Figure 5.9 and 5.10 show and compare the results obtained from running the ant-tracking algorithm in aggressive mode for the smoothed data and graphic equalizer filtered data respectively. The results from running the ant-tracking algorithm in aggressive mode yielded much more structural detail in both the smoothed and graphic equalizer filtered data.

Both images show enhanced structural detail in the seismic data, still resembling results from the passive mode which is good from a data quality-check perspective. Aggressive mode allows the algorithm to illuminate far more linear structures in the data, but caution should be taken as to not overdo the process and run the risk of enhancing noise and artifacts.

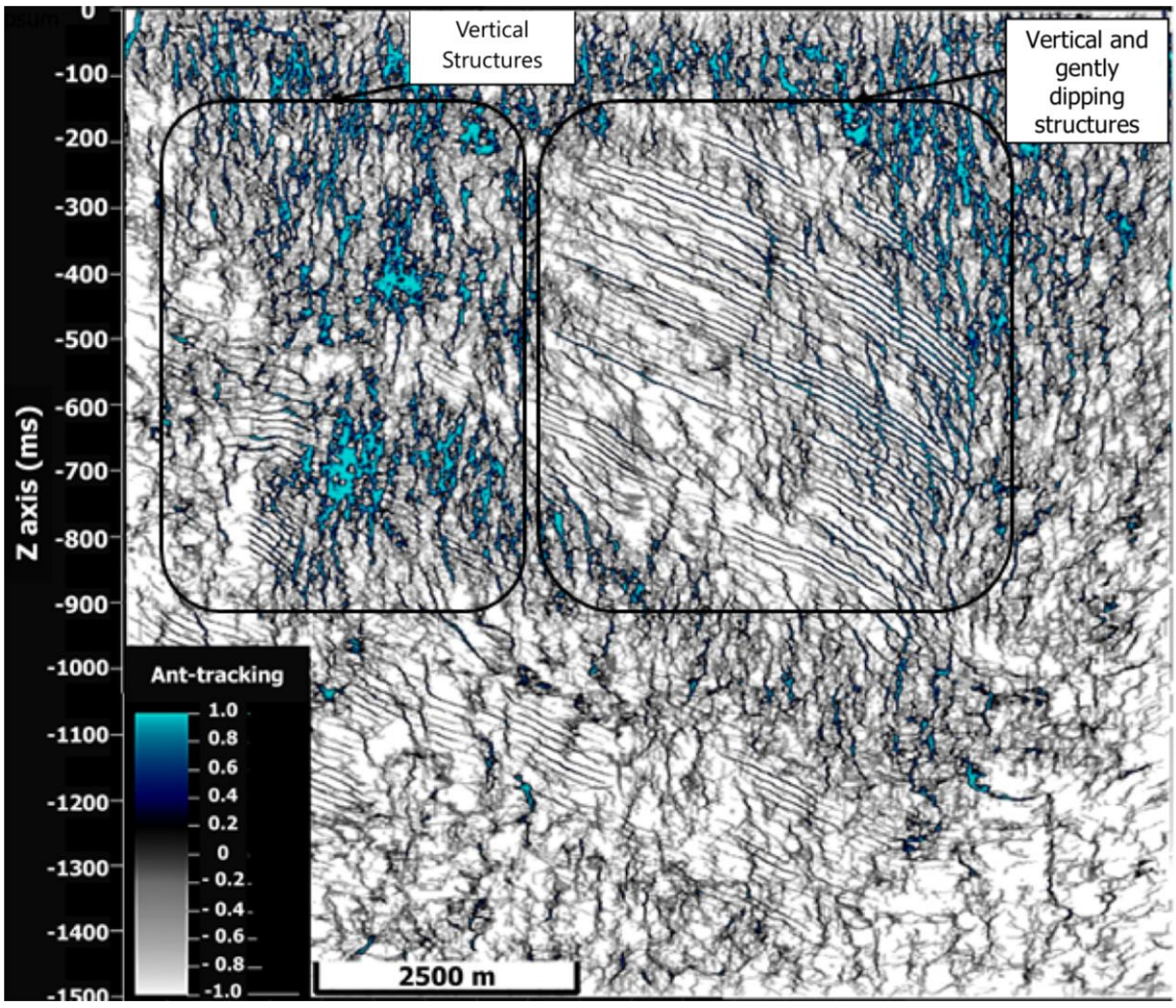

Figure 5.9: Crossline view of the ant-tracking results, run in aggressive mode, from the structurally – smoothed data with variance attribute applied. The visibility and continuity of structures are considerably enhanced compared to the conventional amplitude display. Areas of steep and gently dipping structures can now be seen such as Figure 5.7, but more enhanced.

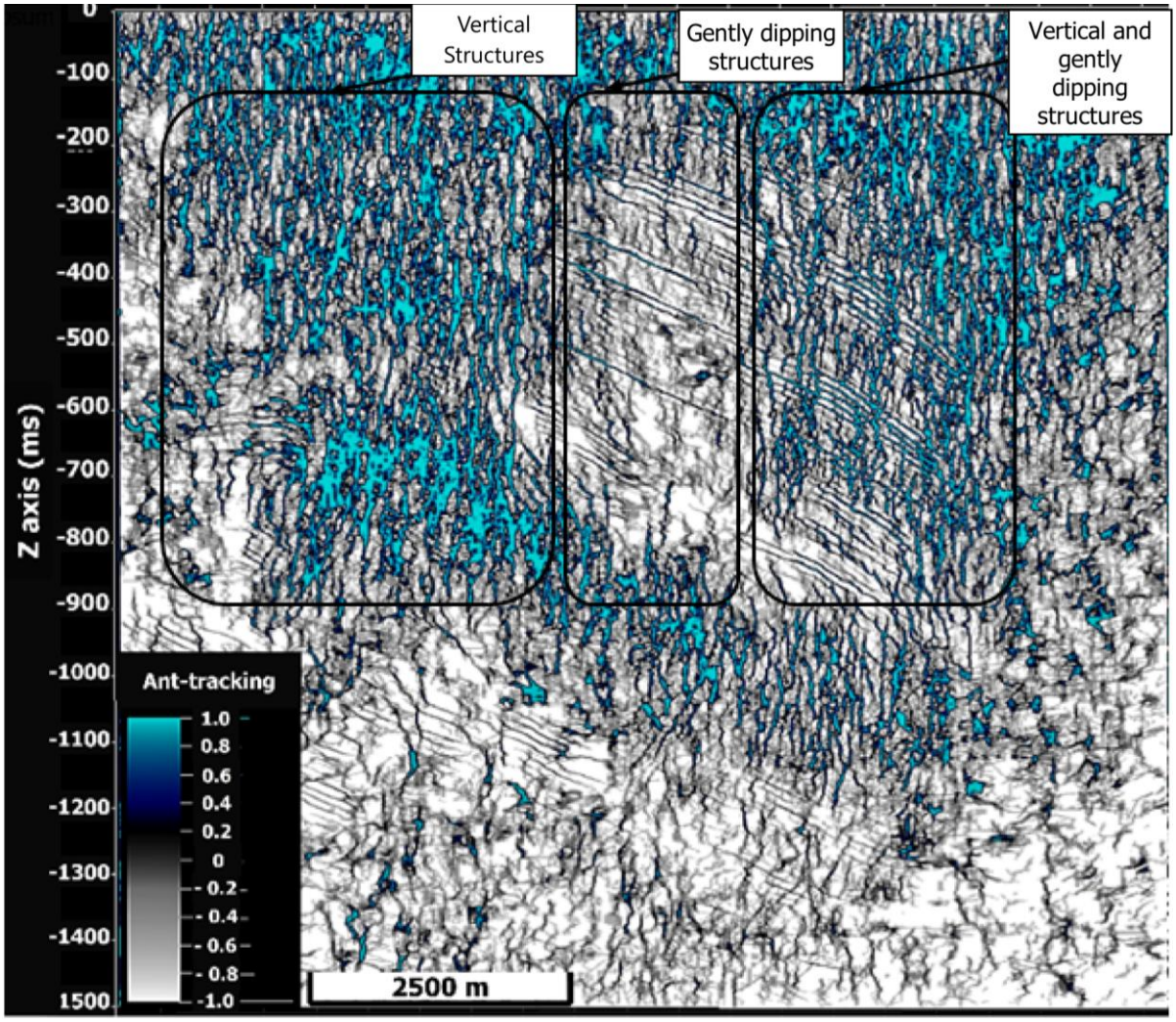

Figure 5.10: Crossline view of the ant-tracking results, in aggressive mode, from the graphic equalizer data with variance attribute applied. The visibility and continuity of structures are considerably enhanced compared to the conventional amplitude display. Areas of steep, gently and a combination of both steep and gently dipping structures can now be seen such as in Figure 5.8, but more enhanced.

Figure 5.11 and 5.12 are results from the ant-tracking algorithm run twice on the smoothed and graphic equalizer filtered variance data respectively. The results are still in agreement with those in Figure 5.7 and 5.8, but slightly enhanced, which reaffirms the confidence in the results with respect to noise and artifacts.

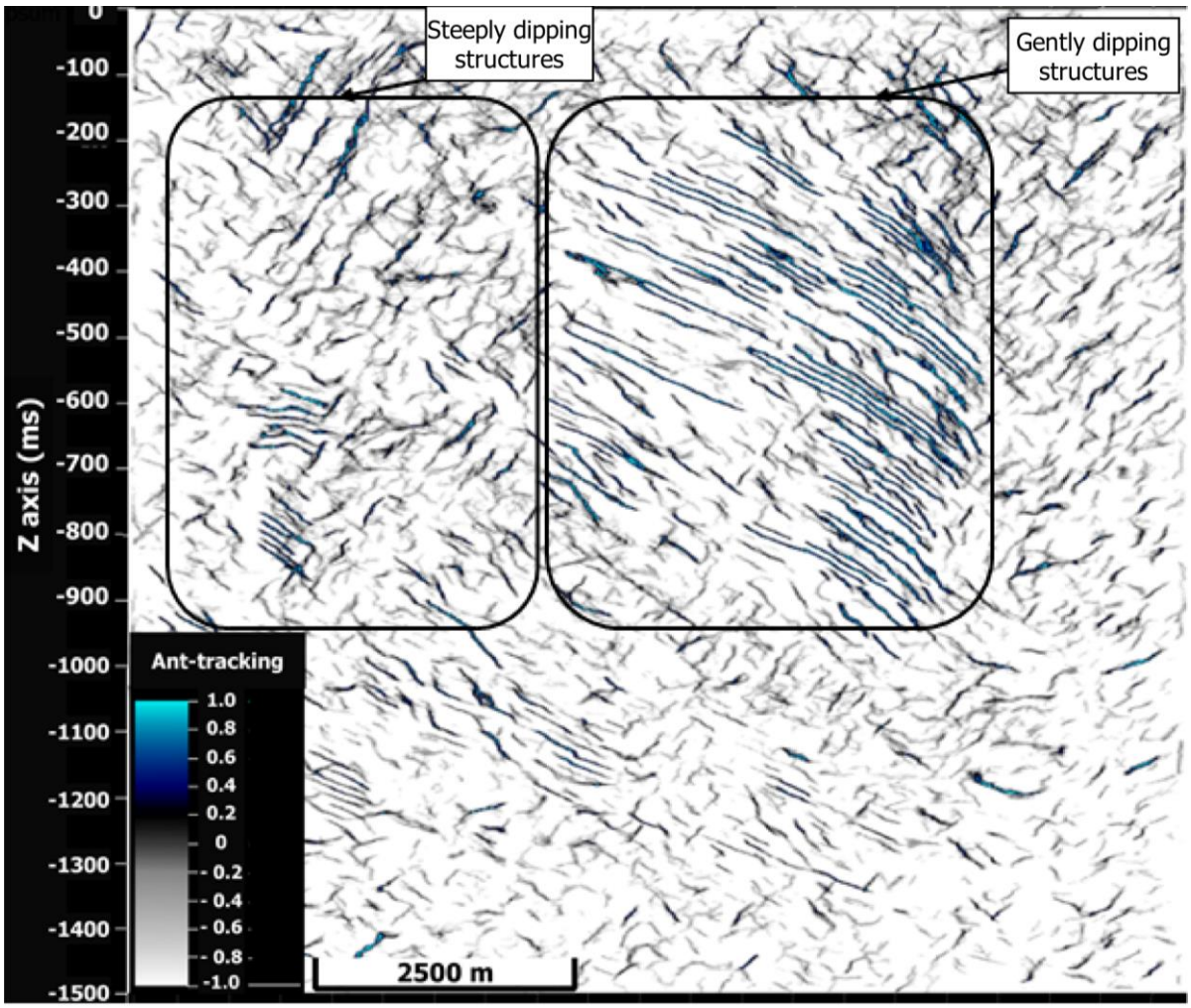

Figure 5.11: Crossline view of the ant-tracking results, run twice in passive mode, from the structurally – smoothed data with variance attribute applied. The visibility and continuity of structures are considerably enhanced compared to the conventional amplitude display. Steep and gently dipping structures can be clearly seen, and their extents better resolved. Care should always be taken as such detail can also bear artifacts.

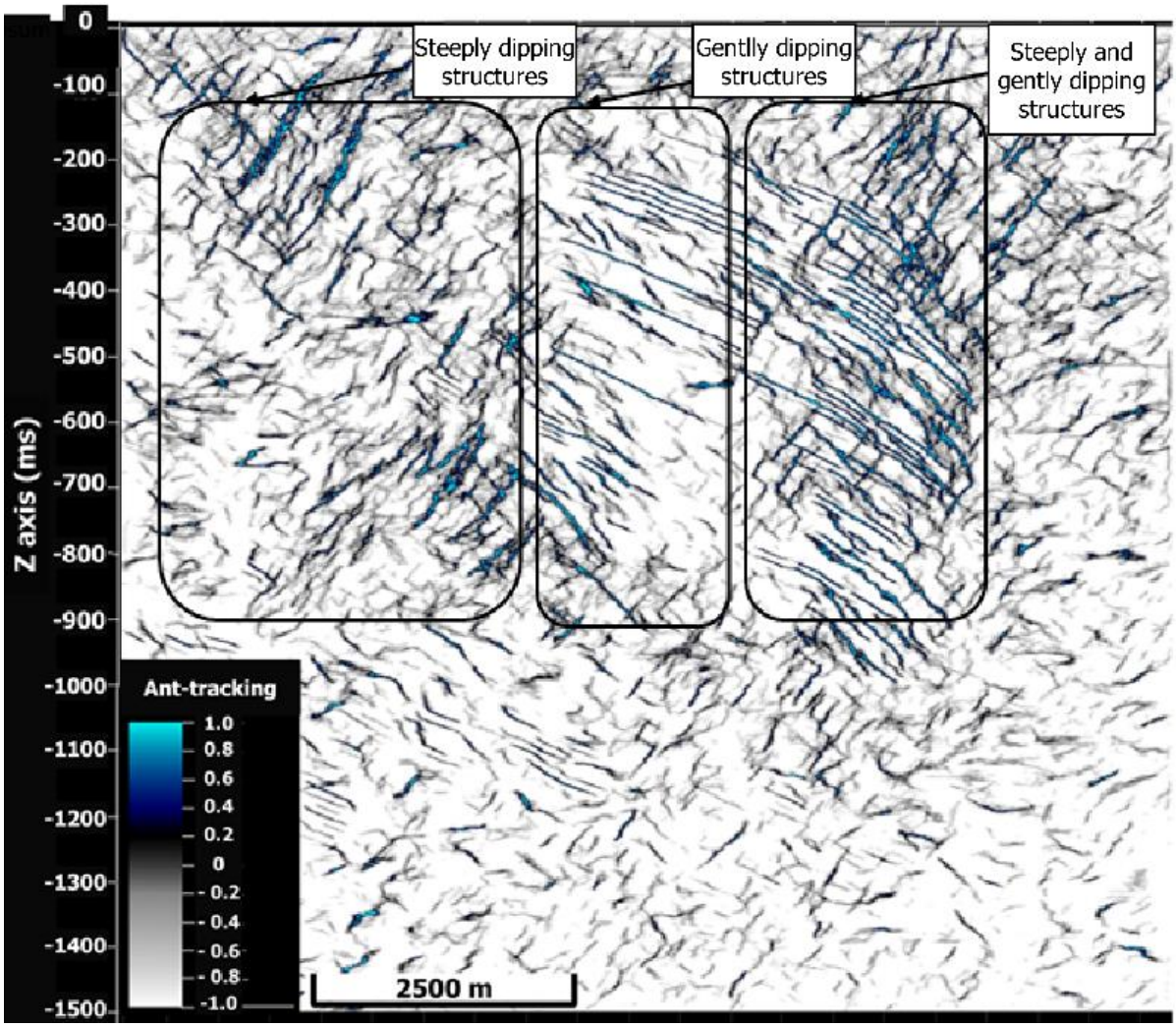

Figure 5.12: Crossline view of the ant-tracking results, run twice in passive mode, from the graphic equalizer data with variance attribute applied. The visibility and continuity of structures are considerably enhanced compared to the conventional amplitude display. Areas of steep, gently and a combination of both steep and gently dipping structures can now be clearly seen, and their extents better resolved. Care should always be taken as such detail can also bear artifacts.

6. Discussion

The aim of this study was to interpret 3D reflection seismic data collected at a platinum mine in the Bushveld Complex, in an area earmarked for future mining operations, to understand the local geology of the economic UG2 marker horizon better. The interpretation was carried out in this study by comparing the conventional seismic interpretation method with seismic attribute analysis. Taking it further, comparison between two interpretation approaches was carried out; namely structural smoothing of data vs graphic equalizer filter of data, comparing their outputs down the ant-tracking workflow, namely; data smoothing, edge detection and edge enhancement.

6.1. Conventional seismic interpretation

Conventional interpretation was initially done to get a quick first pass look at the data and get a sense of the major scale features that would be readily apparent. The overall structure on the western Bushveld Complex is consistent with previous studies; it dips towards the NE in an angle between 9º - 12º (Kinnard, 2015). The UG2 was clearly visible and mapped in the data's inline, crossline and time scale. Picking was aided by borehole data, which was clustered in one part of the mine lease area. In other areas, the UG2 horizon was picked out by extrapolating from the areas where it was confidently mapped.

Picking of faults was not easy to do at this stage as the displacement due to faulting was not clear. On the picked UG2 surface, some depressions were seen in the inline and crossline view, although their resolution was poor. All structures, minor and major, need to be interpreted and understood as they could be possible zones of weakness during mining operations and can cause rock falls, and in worst cases, lead to fatalities. No minor scale features were seismically visible; hence the next step was to apply seismic attributes to illuminate them. The data were first conditioned to reduce noise and increase signal-to-noise ratio prior to seismic attribute application, as these are sensitive to noise.

6.2. Seismic attribute analysis

6.2.1. Horizon-based attributes

The UG2 picked surface was gridded and smoothed to remove the noise introduced by picking, but care was also taken to use an algorithm that will not remove features of interest;

thus, the convergent interpolation was chosen as it fit this criterion. After data smoothing, the surface attributes were then applied.

The dip angle attribute highlighted subtle features on the surface, with relative dip ranging between 0º and 15º. These features could be possible faults, slumps and potholes that need to be investigated further using borehole data and be catered for in future mining planning. The dip - azimuth attribute provides more detail on the surface by providing better definition of faults than the dip angle attribute, and with the change of the colourbar, draws focus on more structures that were invisible to conventional interpretation. These structures are possible zones of reef terracing, as seen in other literature and they clearly need to be well studied and understood. The edge detection attribute was able to highlight far more structures than the dip angle and dip-azimuth by increasing structure definition in more orientations.

The application of the above horizon attributes (local dip and azimuth attributes) has proven to enhance detail invisible in the conventional interpretation method. It was also noted that they rely mostly on the quality of the data, which in this case was of high resolution. The importance of applying multiple seismic attributes was also realized when each of their outputs correlated reasonably well with others. This improved interpretation confidence despite the inability to resolve data at the edges of the survey area due to poor fold coverage. In some areas, the data was too noisy to confidently interpret.

6.2.2. Volumetric attributes

The application of the ant-tracking attribute has been known to provide better definition and continuity of subtle lineaments. This was seen in this study as well, where comparison was also made with results from different ant-tracking workflows. It was noted that the results of the structural smoothing workflow showed that even though the window size was selected out of many options for filtering and the noise was relatively reduced, there was smearing, and some data details were lost, compared to the results from the graphic equalizer. The graphic equalizer attribute showed improved reflector resolution throughout the entire workflow to the ant-tracking results. However, because it muted certain data frequencies and boosted the desired one, it also boosted some noise as seen in the comparison of time slices from both outputs

7. Conclusions

Mining operations in the Bushveld Complex have greatly benefited from the 3D reflection seismic surveys that have been conducted since the 1990s to delineate and effectively map the Merensky and UG2. From conventional interpretation, first order structures that are well above the resolution limit are clearly visible, but finer details are not seen.

Horizon-based seismic attributes were applied to highlight features that were previously invisible. The dip angle attribute highlights dip information, while the dip azimuth highlights structural detail along strike; together they give a full detailed view of a horizon, showing the presence of lineaments and zones of reef depressions. The dip angle attribute detected subtle features dipping between 5º and >10º; while the dip-azimuth attribute revealed large-scale lineaments throughout the surface that trend in the NW – SE direction, as well as some lineaments in the direction of dip. The edge detection attribute, however, adds more resolution than the dip angle and azimuth attributes, highlighting zones associated with regions too noisy to pick that are possible zones of depression. The variance attribute measures the local variance of the data, while the chaos attribute measures the uniformity in the dip angle and dip-azimuth orientations. Variance and chaos attribute volumes were then used as inputs to the ant-tracking algorithm. The ant-tracked volume highlighted lineaments, possibly small faults and joints, that were not visible in the variance and chaos attribute volumes. The ant-tracked volume yielded an enhanced visibility of gently dipping structures, initially seen in the data but not well resolved, as well as steeply dipping structures that were not previously visible to the interpreter.

Results showed that definitive decisions cannot be made from conventional seismic interpretation nor from a single seismic attribute, but better insights and confidence is gained through the careful investigation and use of a combination of seismic attributes. High resolution mapping of the mineralized reef and the definition of zones of reef depression (‘slumps’ and ‘potholes’), fault zones, and reef terracing are all important in the viability of a mining lease area.

References

Admasu, F., 2008. A stochastic method for automated matching of horizons across a fault in 3D seismic data (Doctoral dissertation, Otto-von-Guericke-Universität Magdeburg, Universitätsbibliothek).

Azevedo, L. and Pereira, G.R., 2009. Seismic Attributes in Hydrocarbon Reservoirs Characterization. Universidade de Aveiro, Departamento de Geociências.

Ballhaus, C. G., 1988. Potholes of the Merensky reef at Brakspruit Shaft, Rustenburg platinum mines; primary disturbances in the magmatic stratigraphy: Economic Geology, v. 83, no. 6, pp. 1140-1158.

Barbato, U., 2012. Fault Detection Using the Phase Spectra from Spectral Decomposition (Doctoral dissertation).

Barnes, A. E., 2007. Redundant and useless seismic attributes: Geophysics, v. 72, no. 3, pp. 33-38.

Brouwer, J., and Helbig, K., 1998. Shallow high-resolution reflection seismics, Elsevier.

Campbell, G., 2011, Exploration geophysics of the Bushveld Complex in South Africa: The Leading Edge, v. 30, no. 6, pp. 622-638.

Cawthorn, R. G., 2010. The platinum group element deposits of the Bushveld Complex in South Africa: Platinum Metals Review, v. 54, no. 4, pp. 205-215.

Cawthorn, R. G., and Walraven, F., 1998. Emplacement and crystallization time for the Bushveld Complex: Journal of Petrology, v. 39, no. 9, pp. 1669-1687.

Cawthorn, R., and Webb, S., 2001. Connectivity between the western and eastern limbs of the Bushveld Complex: Tectonophysics, v. 330, no. 3, pp. 195-209.

Chambovet, G., 2006. Keynote Address: Seismic method applied to platinum exploration, a success story!, in Proceedings International Platinum Conference 2006, pp. 17-18.

Chaouch, A., and Mari, J., 2006. 3D Land Seismic Surveys: Definition of Geophysical Parameter: Oil & Gas Science and Technology-Revue de l'IFP, v. 61, no. 5, pp. 611-630.

Chen, Q. and Sidney, S., 1997. Seismic attribute technology for reservoir forecasting and monitoring. The Leading Edge, 16(5), pp.445-448.

Clarke, B., Uken, R. and Reinhardt, J., 2009. Structural and compositional constraints on the emplacement of the Bushveld Complex, South Africa. Lithos, v. 111, no 1-2, pp. 21-36.

Coetzee, A. and Kisters, A.F., 2018. The elusive feeders of the Karoo Large Igneous Province and their structural controls. Tectonophysics, v. 747, pp. 146-162.

Colorni, A., Dorigo, M. and Maniezzo, V., 1991. December. Distributed optimization by ant colonies. In Proceedings of the first European conference on artificial life, v. 142, pp. 134-142.

De Wit, M. J., de Ronde, C. E., Tredoux, M., Roering, C., Hart, R. J., Armstrong, R. A., Green, R. W., Peberdy, E., and Hart, R. A., 1992. Formation of an Archaean continent: Nature, v. 357, no. 6379, pp. 553-562.

Dentith, M., and Mudge, S. T., 2014. Geophysics for the mineral exploration geoscientist, Cambridge University Press.

Dorn, G. A., 1998. Modern 3D seismic interpretation: The Leading Edge, v. 17, no. 9, pp. 1262-1262.

Du Plessis, C., and Walraven, F., 1990. The tectonic setting of the Bushveld Complex in Southern Africa, Part 1. Structural deformation and distribution: Tectonophysics, v. 179, no. 3, pp. 305-319.

Durrheim, R. J., Spottiswoode, S. M., Roberts, M. K. C., and Brink, A. v. Z., 2005. Comparative seismology of the Witwatersrand Basin and Bushveld Complex and emerging technologies to manage the risk of rockbursting: Journal of the Southern African Institute of Mining and Metallurgy, v. 105, no. 6, pp. 409-416.

Durrheim, R.J., 1986. Recent reflection seismic developments in the Witwatersrand basin. Reflection seismology: A global perspective, 13, pp.77-83.

Duweke, W., Trickett, J.C., Tootal, K. and Slabbert, M., 2002. May. Three-dimensional reflection seismics as a tool to optimise mine design, planning and development in the Bushveld Igneous Complex. In 64th EAGE Conference & Exhibition.

Dyrendahl, M.M., 2018. A better Horizon Auto Tracker-Powered by Machine Learning (Master's thesis, NTNU).

Eales, H., and Cawthorn, R., 1996. The bushveld complex: Developments in Petrology, v. 15, pp. 181-229.

Eriksson, P., Hattingh, P., and Altermann, W., 1995. An overview of the geology of the Transvaal Sequence and Bushveld Complex, South Africa: Mineralium Deposita, v. 30, no. 2, pp. 98-111.

Eriksson, P., Reczko, B., Corner, B., and Jenkins, S., 1996. The Kanye axis, Kaapvaal Craton, southern Africa: a postulated Archaean crustal architectural element inferred

from three-dimensional basin modelling of the lower Transvaal Supergroup: Journal of African Earth Sciences, v. 22, no. 3, pp. 223-233.

Gillot, E., Gibson, M., Verneau, D., and Laroche, S., 2005. Application of high-resolution 3D seismic to mine planning in shallow platinum mines: First Break, v. 23, no. 7.

Godel, B., Barnes, S.J. and Maier, W.D., 2006. 3D distribution of sulphide minerals in the Merensky Reef (Bushveld Complex, South Africa) and the JM reef (Stillwater Complex, USA) and their relationship to microstructures using X-ray computed tomography. Journal of Petrology, v. 47, no 9, pp. 1853-1872.

Good, N., and De Wit, M. J., 1997. The Thabazimbi-Murchison lineament of the Kaapvaal Craton, South Africa: 2700 Ma of episodic deformation: Journal of the Geological Society, v. 154, no. 1, pp. 93-97.

Harmer, R.E. and Armstrong, R.A., 2000. November. Duration of Bushveld Complex (sensu lato) magmatism: constraints from new SHRIMP zircon chronology. In Abstracts and program, Workshop on the Bushveld Complex, Gethane Lodge, Burgersfort, South Africa.

Hatton, C., and Schweitzer, J., 1995. Evidence for synchronous extrusive and intrusive Bushveld magmatism: Journal of African Earth Sciences, v. 21, no. 4, pp. 579-594.

Hunt, J.P., 2006. Geological Characteristics of Iron Oxide-Copper-Gold (IOCG) Type Mineralisation in the Western Bushveld Complex (Doctoral dissertation).

Implats, 2015. Mineral resource and mineral reserve statement 2015 - supplement to the integrated annual report 30 June 2015, p. 1-88.

Iske, A. and Randen, T. eds., 2005. Mathematical Methods and Modelling in Hydrocarbon Exploration and Production. Mathematics in Industry. Springer.

Jager, A., and Ryder, J., 1999. A handbook on rock engineering practice for tabular hard rock mines: Safety in Mines Research Advisory Committee, Johannesburg.

Karsten, M. and Mackay, L., 2012. May. Underground environmental challenges in deep platinum mining and some suggested solutions. In Platinum 2012, 5th International Platinum Conference-'A Catalyst for Change.

Kee, S.P., Ghosh, D. and Kadir, A.A., 2017. Innovated PETREL Workflow for Multi-Attribute Analysis: Case Study in Malay Basin.

Kinnaird, J. A., 2005. The Bushveld large igneous province: Review Paper, The University of the Witwatersrand, Johannesburg, South Africa, pp. 39.

Kleemann, G. J., and Twist, D., 1989. The compositionally-zoned sheet-like granite pluton of the Bushveld Complex: Evidence bearing on the nature of A-type magmatism: Journal of Petrology, v. 30, no. 6, pp. 1383-1414.

Ledwaba, L. S., 2012. Seismic damage mechanism at Impala Platinum mine: School of Geosciences, Faculty of Science, University of the Witwatersrand, Johannesburg.

Leeb-Du Toit, A., 1986. The Impala platinum mines: Mineral deposits of southern Africa, v. 2, pp. 1091-1106.

Lougher, D. R. and Mellowship, P., 1991. Strata control problems associated with geological structures on Impala platinum Mines. Impala Internal Report. Unpublished.

Lougher, D., 1994, An in-situ investigation into the behaviour of the surrounding rock mass in a hard rock pillar mining environment.

Manzi, M.S.D., 2014. Application of 3D Seismic Analysis Techniques to Evaluate Ore Resources on Kloof, South Deeps and Driefontein Gold Mines, Witwatersrand Basin, South Africa (Doctoral dissertation, University of the Witwatersrand, Faculty of Science, School of Geosciences)..

Mellman, G., and Kunzinger, P. A., 1992. Forward Modeling of Seismic Data: Part 7. Geophysical Methods.

Ngeri, A.P., Tamunobereton-ari, I. and Amakiri, A.R.C., 2015. Ant-tracker attributes: an effective approach to enhancing fault identification and interpretation. Journal of VLSI and Signal Processing, v. 5, pp. 67-73.

Nguuri, T.K., Gore, J., James, D.E., Webb, S.J., Wright, C., Zengeni, T.G., Gwavava, O. and Snoke, J.A., 2001. Crustal structure beneath southern Africa and its implications for the formation and evolution of the Kaapvaal and Zimbabwe cratons. Geophysical Research Letters, v. 28, no. 13, pp. 2501-2504.

Nwaila, G., Frimmel, H.E. and Minter, W.E., 2017. Provenance and geochemical variations in shales of the Mesoarchean Witwatersrand Supergroup. The Journal of Geology, vol 125, no. 4, pp .399-422.

Othman, A., Mohamed, M. and Mohamed, M., 2016. Improving fault tracing detection applying 3D ant tracking seismic attribute. International Organization of Scientific Research - Journal of Applied Geology and Geophysics, v. 4, no. 3, ver. 1, pp. 18 - 25

Parkseismic.com, (n.d), What is a seismic survey?, [Online] Available at: http://www.parkseismic.com/Whatisseismicsurvey.html [Accessed 16th January, 2019]

Qamata, X., and Steenkamp, J., (n.d), Negotiating Complex Geological Structures by Applying New Mining Strategies. In Association of Mine Managers South Africa Technical papers. [ONLINE] Available at: http://www.ammsa.org.za/downloads/send/2-technical-papers/614-negotiating-complex-geological-structures-by-applying-new-mining-strategies. [Accessed 22 January 2019].

Randen, T., and Sønneland, L., 2005. Atlas of 3D seismic attributes, Mathematical Methods and Modelling in Hydrocarbon Exploration and Production, Springer, pp. 23-46.

Randen, T., Monsen, E., Signer, C., Abrahamsen, A., Hansen, J.O., Sæter, T. and Schlaf, J., 2000. Three-dimensional texture attributes for seismic data analysis. In SEG Technical Program Expanded Abstracts 2000. Society of Exploration Geophysicists, pp. 668-671.

Randen, T., Pedersen, S.I. and Sønneland, L., 2001. Automatic extraction of fault surfaces from three-dimensional seismic data. In SEG Technical Program Expanded Abstracts 2001, pp. 551-554.

Rekoske, K., and Hicks, D., 1992. Synthetic Seismograms: Part 7. Geophysical Methods.

Riemer, K. L., and Durrheim, R. J., 2012. Mining seismicity in the Witwatersrand Basin: monitoring, mechanisms and mitigation strategies in perspective: Journal of Rock Mechanics and Geotechnical Engineering, v. 4, no. 3, pp. 228-249.

Robb, L. J., and Meyer, F. M., 1995. The Witwatersrand Basin, South Africa: geological framework and mineralization processes: Ore Geology Reviews, v. 10, no. 2, pp. 67-94.

Scheiber-Enslin, S.E. and Manzi, M., 2018. Integration of 3D reflection seismics and magnetic data for deep platinum mine planning and risk mitigation: a case study from Bushveld Complex, South Africa. Exploration Geophysics, vol. 49, no. 6, pp. 928-939.

Schweitzer, J., Hatton, C., and Waal, S. d., 1995. Economic potential of the Rooiberg Group: volcanic rocks in the floor and roof of the Bushveld Complex: Mineralium Deposita, v. 30, no. 2, pp. 168-177.

Scoates, J. S., and Friedman, R. M., 2008. Precise age of the platiniferous Merensky Reef, Bushveld Complex, South Africa, by the U-Pb zircon chemical abrasion ID-TIMS technique: Economic Geology, v. 103, no. 3, pp. 465-471.

Scoon, R. N., and Mitchell, A. A., 1994. Discordant iron-rich ultramafic pegmatites in the Bushveld Complex and their relationship to iron-rich intercumulus and residual liquids: Journal of Petrology, v. 35, no. 4, pp. 881-917.

Sheriff, R. E., and Geldart, L. P., 1995. Exploration seismology, Cambridge university press.

Stevenson, F. and Durrheim, R.J., 1997. Reflection seismic for gold, platinum and base metal exploration and mining in Southern Africa. In Proc. of Exploration, v. 97, pp. 391-398).

Subrahmanyam, D. and Rao, P.H., 2008. Seismic attributes–A review. In 7th International Conference & Exposition on Petroleum Geophysics, Hyderabad, pp. 398-404.

Taner, M. T., Schuelke, J. S., O'Doherty, R., and Baysal, E., 1994. Seismic attributes revisited, SEG Technical Program Expanded Abstracts 1994, Society of Exploration Geophysicists, pp. 1104-1106.

Telford, W. M., Geldart, L. P., and Sheriff, R. E., 1990. Applied geophysics, Cambridge university press.

Trickett, J., Duweke, W., and Kock, S., 2004. Three-dimensional reflection seismic: Worth its weight in platinum: SAIMM Journal of the South African Institute of Mining and Metallurgy, v. 105, pp. 252-263.

Twist, D., and French, B., 1983. Voluminous acid volcanism in the Busheveld Complex: A review of the Rooiberg Felsite: Bulletin volcanologique, v. 46, no. 3, pp. 225-242.

Van Bemmel, P.P. and Pepper, R.E., Schlumberger Technology Corp, 2000. Seismic signal processing method and apparatus for generating a cube of variance values. U.S. Patent 6,151,555.

Walraven, F., 1987. Textural, geochemical and genetic aspects of the granophyric rocks of the Bushveld Complex.

Walraven, F., and Hattingh, E., 1993. Geochronology of the Nebo Granite, Bushveld Complex: South African Journal of Geology, v. 96, no. 1-2, pp. 31-41.

Walraven, F., Armstrong, R., and Kruger, F., 1990. A chronostratigraphic framework for the north-central Kaapvaal Craton, the Bushveld Complex and the Vredefort structure: Tectonophysics, v. 171, no. 1-4, pp. 23-48.

Wilson, M., and Anhaeusser, C., 1998. The mineral resources of South Africa (Handbook 16).

Yilmaz, Ö., 2001. Seismic data analysis: Processing, inversion, and interpretation of seismic data, Society of exploration geophysicists.

Yordkayhun, S., 2008. 2D and 3D Seismic Surveying at the CO2SINK Project Site, Ketzin, Germany: The Potential for Imaging the Shallow Subsurface (Doctoral dissertation, Acta Universitatis Upsaliensis).

Zhang, T., Lin, Y., Liu, K.H., Alhakeem, A. and Gao, S., 2017. Fault visualization enhancement using ant tracking technique and its application in the Taranaki basin, New Zealand. In SEG Technical Program Expanded Abstracts 2017. Society of Exploration Geophysicists, pp. 2350-235.

Zindi, L., 2008. No. 17 Shaft project—overcoming 'fourth generation 'technical challenges. In Proceedings of the Third International Platinum Conference: 'Platinum in Transformation.

Zoeppritz, K., 1919. On the reflection and propagation of seismic waves at discontinuities. Erdbebenwellen, v. VII, no. B, pp. 66-84.